Interacting multiterminal Josephson junctions
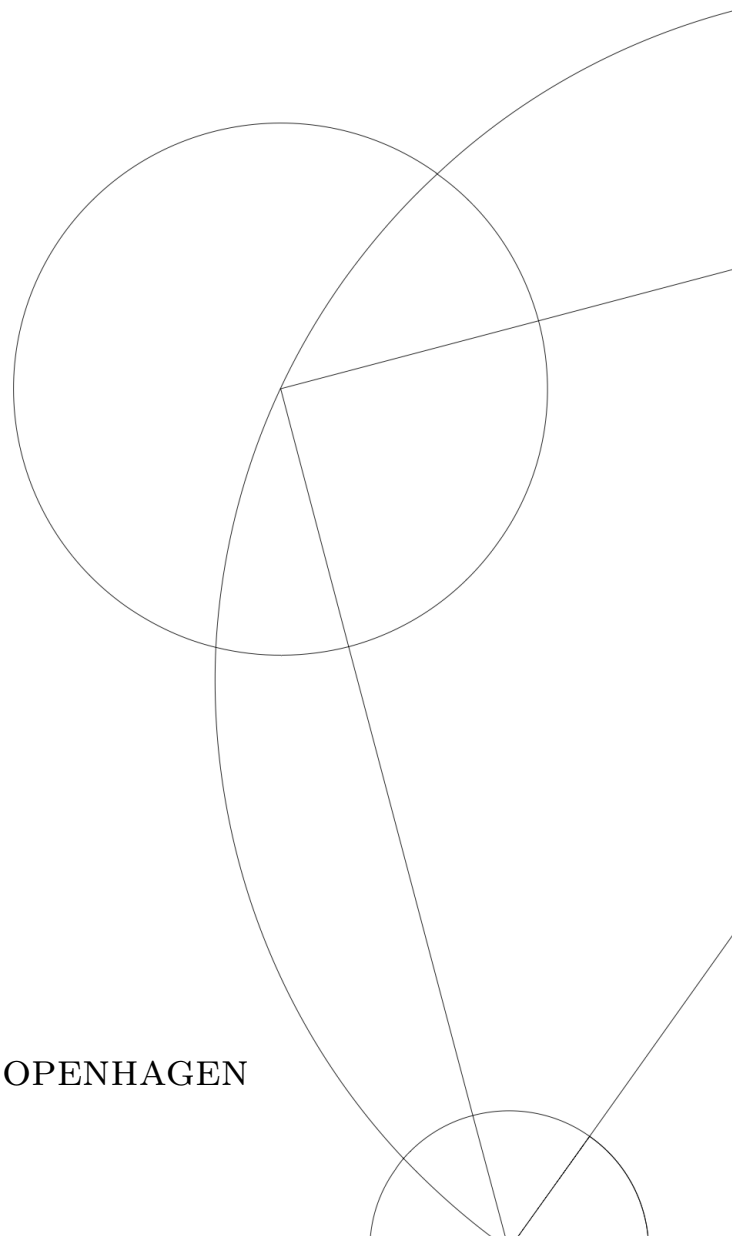
A study of the superconducting impurity Anderson model

Master's thesis
Written by *Emil Jermiin Pedersen Frost*
May 22, 2023

Supervised by
Jens Paaske

University of Copenhagen

FACULTY:	Faculty of Science
DEPARTMENT:	Niels Bohr Institute
AUTHOR:	Emil Jermiin Pedersen Frost
EMAIL:	emiljpfrost@gmail.com
TITLE AND SUBTITLE:	Interacting multiterminal Josephson junctions - A study of the superconducting impurity Anderson model
SUPERVISOR:	Jens Paaske
HANDED IN:	22.05.2023
DEFENDED:	07.06.2023

NAME _____

SIGNATURE _____

DATE _____

Abstract

This thesis studies interacting multiterminal Josephson junctions in the context of a single-level quantum dot (QD) coupled to multiple s-wave superconductors using the superconducting impurity Anderson model. We derive the effective action for electrons on the QD and show – in the limit of large superconducting gap (proximitized limit) – that this leads to an effective low-energy Hamiltonian which describes proximity-induced superconductivity of the QD. In this limit, we obtain the eigenenergies, eigenstates, and the QD phase diagram, showing the transition from a BCS-like singlet to a magnetic doublet. Next, we consider the leading order corrections to describe finite-gap systems and find the energy level shifts through a self-consistent renormalization. We compare the phase diagram with NRG and find good agreement for single-lead systems in the proximitized limit and even for moderate interactions $U \sim \Delta$. For two-lead systems with cancelled proximity effect ($\varphi = \pi$), the model fails to describe the persistent doublet region around particle-hole symmetry. We also develop a zero-bandwidth (ZBW) model which is shown to capture some qualitative features of the full Anderson model, namely the transition from a BCS-like singlet to a YSR-screened singlet as Δ/U is decreased as well as similar bound state energy spectra, supercurrents, and phase diagrams. In the proximitized limit, we state the appropriate conversion from the effective ZBW tunneling rate t to the hybrdization Γ of the Anderson model; the conversion is shown to be independent of U. We find solid agreement with NRG results – showing that the ZBW model is able to describe proximitized QDs on a quantitative level. In the Kondo limit $U \gg \Gamma \gg \Delta$, we utilize the phase transition relation $T_K = 0.3\Delta$ from NRG to scale t. By interpolating between the proximitized limit and the Kondo limit, we extend the validity of the ZBW model, but find it inadequate in describing the strongly interacting limit due to the lack of a continuum of states in the leads.

Acknowledgments

First of all, I would like to thank my patient, inspiring, and encouraging supervisor, Jens. Through the process he has taught me a lot of fascinating physics and always been ready for helpful discussions concerning new ideas and unavoidable complications. The open-door policy was frequently used and many late afternoons were well-spent in your company.

Second of all, I express my gratitude towards my good friend Thomas as well as my office mates Qiyu and Oliver – partly for their interest in my project and partly for taking my mind off the project when I needed it.

Third of all, I thank Gorm Steffensen and Virgil Baran for fruitful discussions and planting new seeds of ideas in my mind.

Lastly, I want to tell my parents their continued support and enthusiasm means the world to me.

Contents

1 Introduction

Quantum dots embedded in Josephson junctions is an interesting platform to study as it lends itself to examination of the intriguing competition between superconductivity and magnetism. Experimentally, the manufactured devices are engineered to have a high degree of tunability of the relevant model parameters. The simple nature of the systems makes it an ideal platform for theory and experiment to come together. In such systems, small quantum dot (QD) regions can be made to resemble a single, localized magnetic moment which in turn will affect the properties of the Josephson junction in which the QD is embedded. In this way, measurements such as the conductance of the junction can give insight into the energy spectrum of the QD and, hence, the underlying physics. The energy scales also make such systems highly relevant for the study of the Kondo effect in relation to superconductivity. In a sense, they are competing phenomena as superconductivity seeks to bond electrons into Cooper pairs that carry no net spin while the Kondo effect tries try screen a local moment (on a QD) by breaking apart the Cooper pairs into screening quasiparticles with opposite spin to the local moment. In some parameter regimes, superconductivity prevails and in others, the Kondo effect.

In this thesis, we study interacting multiterminal Josephson junctions through the superconducting Anderson impurity model via different approximation schemes. In the rest of Section 1, we review BCS theory, Josephson junctions, quantum dots, and the Anderson model to lay the foundation of some of the key concepts relevant for this thesis. In Section 2, we define the physical system we will be studying along with the Hamiltonian before we integrate out the leads to find an effective action for electrons on the QD. In Section 3 we find a low-energy effective Hamiltonian in the infinite gap limit which describes the proximity effect and discuss the eigenstates, eigenenergies, and the phase diagram before we move on to finite superconducting gaps in Section 4. In the last part of the thesis we go into detail with a zero-bandwidth model (Section 5) and evaluate its effectiveness as both a qualitative and quantitative tool.

1.1 BCS theory

Bardeen, Cooper, and Schrieffer (BCS) introduced their theory of superconductivity in their seminal paper from 1957 [1]. The idea is that, in an electron gas, the Fermi sea ground state is unstable towards the formation of Cooper pairs near the Fermi surface for an arbitrary

small electron-electron attraction. These Cooper pairs, that consist of two electrons of opposite momentum and spin, are responsible for the superconducting properties such as zero resistivity and the Meissner effect. BCS explained this for a phonon-mediated (conventional) superconductor whose effective electronic interactions are modelled by a simplified Bardeen-Pines interaction.

For an electrically neutral material with a lattice of positively charged ions immersed in a sea of itinerant electrons, the effective electron-electron interactions are described by the Bardeen-Pines interaction [2, 3].

$$V_{\text{eff}}(\boldsymbol{q}, \nu) = \frac{e^2}{\epsilon_0(q^2 + \kappa^2)} \left(1 + \frac{\omega_q^2}{\nu^2 - \omega_q^2} \right). \tag{1.1}$$

The first term describes the direct electron-electron Coulomb interactions which are screened by the positively charged ions over the Thomas-Fermi screening length $\kappa^{-1} = \sqrt{\epsilon_0/(2e^2\nu_F)}$ with vacuum permittivity ϵ_0, electron charge e, and electronic density of states at the Fermi level ν_F. The second term describes the phonon-mediated interactions. Here, $\omega_q^2 = \Omega_p^2 q^2/(q^2 + \kappa^2)$ is a renormalized ionic plasma frequency, where $\Omega_p^2 = (Ze)^2 n_{\text{ion}}/(\epsilon_0 M)$ with proton number Z, ionic mass M, and density n_{ion}. Due to the heavy mass of the ions compared to the light electrons, only the phonon-mediated interactions are frequency-dependent and, hence, retarded in this approximation. The direct Coulomb interactions are considered instantaneous in time. The cartoon picture of the phonon-mediated interaction is a negatively charged electron traversing the lattice, attracting the positively charged ions, and leaving behind a slight positive charge compared to the unperturbed lattice. This attracts another electron, meaning the pair of electrons are effectively attracted to each other without being close to each other at the *same* time.

From Eq. (1.1), it is clear that electrons in states with energy difference $|\nu| < |\omega_q|$ are attracted ($V_{\text{eff}} < 0$); phonon-mediated attraction overcomes the Coulomb repulsion. BCS simplified this interaction further and replaced it with a constant attraction for energies $-\omega_D < \nu < \omega_D$ within a thin shell around the Fermi surface and $V_{\text{eff}} = 0$ outside. The thickness of the shell is the typical phonon energy, here given by the Debye frequency ω_D.

Superconductivity is inherently a many-particle phenomena, leading to a macroscopic, coherent wave function. Therefore, it serves to describe superconductors in the second quantization formalism by introducing creation (annihilation) operators for the electrons $c_{k\sigma}^\dagger(c_{k\sigma})$, which creates (annihilates) an electron with momentum k and spin $\sigma \in \{\uparrow, \downarrow\}$. The operators satisfy the usual fermionic anti-commutation relations $\{c_{k\sigma}^\dagger, c_{k'\sigma'}\} =$

$\delta_{k,k'}\delta_{\sigma,\sigma'}$, $\{c_{k\sigma}, c_{k'\sigma'}\} = \{c_{k\sigma}^\dagger, c_{k'\sigma'}^\dagger\} = 0$. The BCS Hamiltonian only considers interactions between zero-momentum Cooper pair states and takes the form

$$H_{\text{BCS}} = \sum_{k\sigma} \xi_k c_{k\sigma}^\dagger c_{k\sigma} + \sum_{kk'} V_{kk'} c_{k\uparrow}^\dagger c_{-k\downarrow}^\dagger c_{-k'\downarrow} c_{k'\uparrow}, \qquad (1.2)$$

with electronic dispersion $\xi_k = \epsilon_k - \mu$ (measured from the chemical potential) and scattering matrix elements $V_{kk'}$ between Cooper pair states. We will only be concerned with zero temperature physics, meaning the chemical potential coincides with the Fermi energy: $\mu = \epsilon_F$. In simple s-wave superconductors as BCS considered, $V_{kk'}$ is taken to be an attractive, constant, and isotropic interaction close to the Fermi surface

$$V_{kk'} = \begin{cases} -g_0, & |\xi_k|, |\xi_k'| < \omega_D \\ 0, & \text{otherwise,} \end{cases} \qquad (1.3)$$

where $g_0 > 0$ is the average interaction strength.

In the thermodynamic limit (infinite system size), fluctuations are negligible and a mean field approximation is justified, yielding the effective Hamiltonian

$$H_{\text{BCS}}^{\text{MF}} = \sum_{k\sigma} \xi_k c_{k\sigma}^\dagger c_{k\sigma} - \sum_k \left(\Delta c_{k\uparrow}^\dagger c_{-k\downarrow}^\dagger + \Delta^* c_{-k\downarrow} c_{k\uparrow} \right), \qquad (1.4)$$

where the pairing potential $\Delta = g_0 \sum_{|\xi_k| < \omega_D} \langle c_{-k\downarrow} c_{k\uparrow} \rangle$ is determined self-consistently such that the free energy is minimized. This Hamiltonian is only bilinear and may be diagonalized, yielding quasi-particle excitations with energies $E_k = \pm\sqrt{\xi_k^2 + |\Delta|^2}$, a gapped spectrum around the Fermi level. In the language of the phenomenological Ginzburg-Landau theory, the pairing potential $\Delta = |\Delta|e^{i\varphi}$ is the complex order parameter which becomes finite and breaks U(1) gauge symmetry when the material becomes superconducting and coherently chooses a *macroscopic* complex phase φ. One might ask what happens when two superconductors with different complex phases are placed in close contact; this is the exciting topic of Josephson junctions.

1.2   Josephson junctions

A Josephson junction (JJ) consists of two superconducting electrodes in weak contact through a region of a different material, e.g. an insulator or a normal metal; these are abbreviated as S-I-S and S-N-S junctions, respectively. Quantum mechanics allows for tunneling between the superconducting regions if the tunneling barrier is surmountable. When the voltage bias between the superconducting electrodes is less than the critical

value $eV_c = 2\Delta$, normal current can't flow. However, electrons bound in Cooper pairs may tunnel through the barrier giving rise to a (super-)current across the junction. This is referred to as the *Josephson effect* after B. D. Josephson who received the Nobel prize in 1973 for his work on this topic [4]. Opposed to normal metals with a finite resistance, no voltage bias is required between the superconducting electrodes for a current to flow. The effect is observable if there is a phase difference between the superconducting order parameters across the junction.

For a perfect JJ with a narrow intersection region compared to the coherence lengths of the superconductors, the Josephson equations relate the supercurrent I_J and voltage drop V across the junction to the phase difference $\Delta\phi$ of the two superconductors [5].

$$I_J = I_c \sin(\Delta\phi), \tag{1.5}$$

$$\frac{\mathrm{d}}{\mathrm{d}t}(\Delta\phi) = \frac{2eV}{\hbar}. \tag{1.6}$$

The maximum supercurrent I_c that can be driven through the junction with $V = 0$ is determined by the normal state resistance of the junction and the superconducting gap [6]. In a physical experiment, the *current* bias may be fixed to a constant value $I_J < I_c$ which fixes the phase difference $\Delta\phi = \arcsin(I_J/I_c)$ and $V = 0$ (since the phase difference is time-independent). This is known as the *direct* current Josephson effect. Conversely, if the *voltage* bias is constant in time and nonzero $V \neq 0$, the phase difference advances linearly in time $\Delta\phi = \Delta\phi_0 + 2eVt/\hbar$. This produces an alternating current $I_J = I_c \sin(\Delta\phi_0 + 2eVt/\hbar)$ with frequency $\nu = K_J V$ and Josephson constant $K_J = 2e/h \approx 483.6\,\mathrm{GHz/mV}$. This is known as the *alternating* current Josephson effect.

As mentioned, the weak contact region may be made of different materials. For a S-N-S junction with a normal metal (not superconducting by itself) in the middle, the adjacent superconductors will, in fact, induce superconductivity in the material. This is known as the *proximity* effect. Subgap bound states form within the normal region and Cooper pairs are transported across the junction through Andreev scattering off the normal-superconducting interfaces. Here, an electron in the normal metal is reflected as a hole at the superconductor interface if it has less energy than the superconducting gap $E < \Delta$; there are no states in the superconductor with that energy. Simultaneously, a Cooper pair is formed in the superconductor, yielding a charge transport of $2e$ at the interface.

1.3 Quantum dots

Interesting physics arise when one can control the electronic occupation on the level of single electrons in the junction region. Experimentally, it is possible to confine electrons to a small region in space. Like a quantum particle in a box, the spacing between energy levels grows as the region shrinks, making it possible to isolate and conduct experiments with a single orbital. This is the basic idea behind (single-level) quantum dots (QDs). The small confinement also results in a large Coulomb repulsion between electrons on the QD, typically on the order of meV. The electronic occupation of the QD may be controlled through a capacitively coupled electrode which varies the electrostatic potential close to the QD. There is a profound difference between an even and an odd number of electrons on the QD. An odd number of electrons means a half-filled orbital with an unpaired electron and, hence, a local magnetic moment. Among other things, this affects the bound states and transport properties, making S-QD-S junctions behave quite differently from S-N-S junctions. The local electron-electron repulsion gives rise to Coulomb-blockaded transport and a local magnetic moment may be screened by quasiparticles in the leads.

To probe such an S-QD-S junction, one might construct a device such as the one depicted in Fig. 1.1 from Ref. [7] in which a QD is placed into a transmon circuit. The central part of the device is the 10 μm long superconductor-semiconductor nanowire with a core of InAs and Al shell seen in Figs. 1.1(c) and 1.1(d). The actual QD is simply the 200 nm long region seen in Fig. 1.1(d) where the Al has been etched away. Underneath, there are three gates to tune the electrostatic potential and confine electrons. These control the QD energy level and coupling strengths to the SC leads. The S-QD-S junction is placed in parallel with another JJ to form a SQUID loop. Then, the phase difference across the S-QD-S junction can be measured when an external flux is threaded through the SQUID. The SQUID is capacitively coupled to an LC circuit to measure resonant frequencies of the transmon circuit – excitations of the QD. Theoretical models of such systems are often based on the Anderson model which we will briefly review.

1.4 The Anderson model

Consider an impurity embedded in a metallic host with a localized state at the impurity site. Let us denote the wave function $\psi_d(r) = \langle r|d \rangle$ and charge density $\rho_d(r) = e|\psi_d(r)|^2$. If the state is doubly occupied by both a spin up and down electron, the Coulomb repulsion
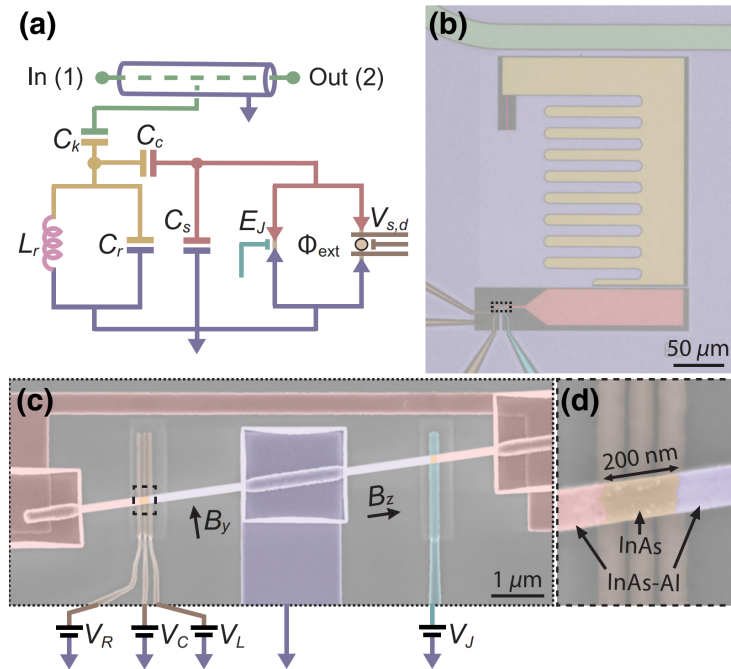
Figure 1.1: Transmon circuit with quantum dot from Ref. [7]. (a) shows the ciruit diagram with the transmission line (green) capacitively coupled to an LC resonator and to a SQUID loop with penetrating flux Φ_{ext} and two JJs – one for reference and one to be measured. (b)-(d) are images of the actual device, colored to match (a) (zoom region indicated by inset rectangles).

between the electrons

$$U = \frac{1}{4\pi\epsilon_0} \int \mathrm{d}^3\boldsymbol{r}\, \mathrm{d}^3\boldsymbol{r}' \frac{1}{|\boldsymbol{r} - \boldsymbol{r}'|} \rho_d(\boldsymbol{r})\rho_d(\boldsymbol{r}'), \tag{1.7}$$

may be a large energy expense. If this is the case, the system may favor to occupy the impurity state with only a single electron, leading to the formation of a local moment. This is the idea behind local moments in the Anderson model.

For simplicity, we consider only a single localized impurity orbital with energy level ϵ_d and Coulomb repulsion U. The Anderson Hamiltonian then takes the form [8]

$$H_A = \epsilon_d n_d + U n_{d\uparrow} n_{d\downarrow} + \sum_{k\sigma} \xi_k c^\dagger_{k\sigma} c_{k\sigma} + \sum_{k\sigma} t_k c^\dagger_{k\sigma} d_\sigma + t^*_k d^\dagger_\sigma c_{k\sigma}, \tag{1.8}$$

where $n_d = n_{d\uparrow} + n_{d\downarrow}$ and $n_{d\sigma} = d^\dagger_\sigma d_\sigma$ counts the number of d-electrons with spin σ in the impurity state. The third term in the Hamiltonian is the kinetic term for the conduction electrons and the last term describes the tunneling or hybridization between conduction electrons and the localized impurity state.

In the (atomic) limit $t_k = 0$ with no hybridization, the Hamiltonian is trivially diagonalized. The metal has a filled Fermi sea with three possible ground state energies for the d-electrons: $0, \epsilon_d, 2\epsilon_d + U$, corresponding to states with zero, one, or two electrons and denoted by $|0\rangle, |\sigma\rangle, |\uparrow\downarrow\rangle$, respectively. The state with single occupancy is doubly spin-degenerate. For $\epsilon_d > 0$ (energy is measured from the Fermi energy of the metal), the impurity state is empty. For $\epsilon_d < 0$, one electron is added from the metal and if $\epsilon_d + U < 0$, it pays off to add a second electron. This is illustrated in Fig. 1.2. For $-U < \epsilon_d < 0$, $|\sigma\rangle$ is the ground state which defines the local moment regime in the atomic limit. At the points $\epsilon_d = -U, 0$, the ground state becomes charge-degenerate. With finite hybridization, these points evolve into regimes of mixed-valence.

1.4.1   Local moment regime

If the level spacings between the ground state and excited states are large compared to the hybridization $\Gamma = \pi\nu_F t^2$, the picture with a well-defined particle number does not change too much and we can consider the hybridization a perturbation to the atomic limit. In the local moment regime ($-U < \epsilon_d < 0$ and $|\epsilon_d + U|, |\epsilon_d| \gg \Gamma$), one can show, through a Schrieffer-Wolf transformation, that virtual excitations to the empty and doubly occupied d-states lead to an effective anti-ferromagnetic exchange interaction between the
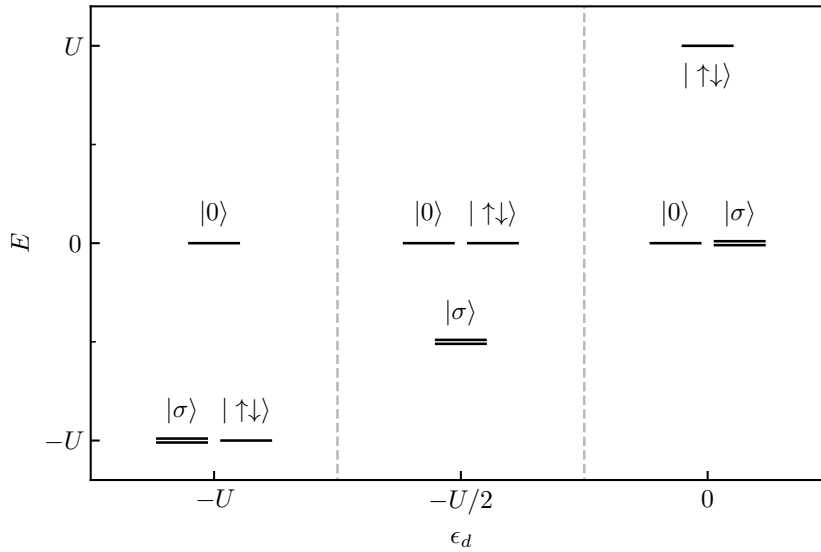
Figure 1.2: Impurity energy levels relative to the Fermi energy of the host metal in the atomic limit of the Anderson model. The energy levels are drawn in the local moment regime at $\epsilon_d = -U, -U/2, 0$.

local impurity moment and the conduction electrons [9].

$$J\nu_F = -\frac{2}{\pi}\frac{\Gamma U}{\epsilon_d(\epsilon_d + U)} > 0. \tag{1.9}$$

This effect leads to screening of the impurity spin and the formation of a Kondo singlet ground state when $T \ll T_K$. The Kondo temperature T_K is determined by the size of the exchange interaction J. At the particle-hole symmetric point $\epsilon_d = -U/2$, $J\nu_F = 8\Gamma/\pi U$, such that $J\nu_F \ll 1$ when $U \gg \Gamma$ in the local moment regime. Using a scaling argument of the Anderson model, Haldane [10] derived an expression for the Kondo temperature

$$T_K = 0.182\sqrt{\frac{8\Gamma U}{\pi}}\exp\left[\frac{\pi}{2}\frac{\epsilon_d(\epsilon_d + U)}{\Gamma U}\right]. \tag{1.10}$$

At particle-hole symmetry in the local moment regime, this energy scale is small compared to the large Coulomb interaction: $T_K/U \propto \sqrt{8\Gamma/\pi U}\exp(-\pi U/8\Gamma) \ll 1$. We will return to the Kondo temperature later. For now, we move on to how we use the Anderson model to model interacting multiterminal Josephson junctions.

2 Modelling multiterminal Josephson junctions

In this thesis, we will study so-called multiterminal Josephson junctions (MJJs) with a QD in the interface region. Instead of only two leads – as in Fig. 1.1(d) – we consider a single QD tunnel-coupled to $N \in \mathbb{N}$ superconducting leads indexed by $\alpha = 1, 2, ..., N$. We describe this system using a single-orbital superconducting Anderson model $H = H_S + H_D + H_{S-D}$. We assume the leads are described by simple s-wave BCS Hamiltonians (see Eq. (1.4)) with different electronic dispersions $\xi_{\alpha k}$ in general.

$$H_S = \sum_{\alpha k \sigma} \xi_{\alpha k} c^\dagger_{\alpha k \sigma} c_{\alpha k \sigma} - \sum_{\alpha k} \left(\Delta_\alpha c^\dagger_{\alpha k \uparrow} c^\dagger_{\alpha - k \downarrow} + \Delta^*_\alpha c_{\alpha - k \downarrow} c_{\alpha k \uparrow} \right). \tag{2.1}$$

The pairing potential $\Delta_\alpha = |\Delta_\alpha| e^{i\varphi_\alpha}$ can vary between leads in both magnitude and phase. Absolute phases are, however, gauge-dependent and only phase *differences* are physically meaningful (e.g. relating to current flows as in Eq. (1.5)). Hence, without loss of generality, we set $\varphi_N = 0$ and measure all other phases relative to lead N. The bandwidth of lead α is assumed to be $2D_\alpha$ such that $\xi_{\alpha k} \in [-D_\alpha, D_\alpha]$. We can think of the QD as a single electronic level with Coulomb repulsion $U > 0$.

$$H_D = \sum_\sigma \epsilon_d n_{d\sigma} + U n_{d\uparrow} n_{d\downarrow}, \tag{2.2}$$

where $n_{d\sigma} = d^\dagger_\sigma d_\sigma$ counts the number of electrons with spin σ on the QD. The filling may be controlled through a gate voltage that adjusts the energy level ϵ_d; the electrodes below the QD in Fig. 1.1(d). The QD is in contact with the leads, giving rise to electron-tunneling which we assume, for simplicity, to be momentum-independent.

$$H_{S-D} = \sum_{\alpha k \sigma} t_\alpha c^\dagger_{\alpha k \sigma} d_\sigma + t^*_\alpha d^\dagger_\sigma c_{\alpha k \sigma}. \tag{2.3}$$

Furthermore, we assume the direct tunneling between individual leads to be negligible, i.e. all tunneling happens through the QD. If the QD orbital is occupied by a single electron, a local moment develops. As with a magnetic impurity in a superconductor, this gives rise to the formation of Yu-Shiba-Rusinov (YSR) bound states inside the superconducting gap [11–13]. In terms of gauge choice, we have $N + 1$ degrees of freedom to work with from N leads and one QD. This means that, without loss of generality, we may choose the phase of $N + 1$ parameters from the $2N$ parameters Δ_α and t_α. We already set $\varphi_N = 0$ and in the following, we choose a gauge in which the tunneling amplitudes are real ($t_\alpha = |t_\alpha|$).

2.1 Effective action for electrons on the QD

In this section, we will formulate the problem in terms of path integrals and integrate out the leads to arrive at an effective action for the electrons on the QD. To this end, we replace the fermionic operators with Grassman fields that are anti-periodic in imaginary time τ over a period of the inverse temperature $\beta = 1/k_B T$

$$
\begin{aligned}
c_{\alpha k \sigma} &\to c_{\alpha k \sigma}(\tau), \\
c_{\alpha k \sigma}^\dagger &\to \bar{c}_{\alpha k \sigma}(\tau), \\
d_\sigma &\to d_\sigma(\tau), \\
d_\sigma^\dagger &\to \bar{d}_\sigma(\tau),
\end{aligned}
\tag{2.4}
$$

and write the total action as $S = S_S + S_D + S_{S-D}$ in complete analogy with how we separated the Hamiltonian. The terms are given by (suppressing the time dependence of the fields for the sake of readability)

$$
S_S = \int_0^\beta d\tau \left\{ \sum_{\alpha k \sigma} \bar{c}_{\alpha k \sigma}(\partial_\tau + \xi_{\alpha k}) c_{\alpha k \sigma} - \sum_{\alpha k} (\Delta_\alpha \bar{c}_{\alpha k \uparrow} \bar{c}_{\alpha - k \downarrow} + \Delta_\alpha^* c_{\alpha - k \downarrow} c_{\alpha k \uparrow}) \right\}, \tag{2.5a}
$$

$$
S_D = \int_0^\beta d\tau \left\{ \sum_\sigma \bar{d}_\sigma(\partial_\tau + \epsilon_d) d_\sigma + U \bar{d}_\uparrow \bar{d}_\downarrow d_\downarrow d_\uparrow \right\}, \tag{2.5b}
$$

$$
S_{S-D} = \int_0^\beta d\tau \sum_{\alpha k \sigma} \left[t_\alpha \bar{c}_{\alpha k \sigma} d_\sigma + t_\alpha \bar{d}_\sigma c_{\alpha k \sigma} \right], \tag{2.5c}
$$

where the partial time derivative ∂_τ is the Berry phase term. Due to the anomalous terms in the BCS part, it is convenient to rewrite the quadratic terms using Nambu spinors.

$$
\begin{aligned}
\psi_{c \alpha k}(\tau) &= \begin{pmatrix} c_{\alpha k \uparrow}(\tau) \\ \bar{c}_{\alpha - k \downarrow}(\tau) \end{pmatrix}, \quad \bar{\psi}_{c \alpha k}(\tau) = \begin{pmatrix} \bar{c}_{\alpha k \uparrow}(\tau), & c_{\alpha - k \downarrow}(\tau) \end{pmatrix}, \\
\psi_d(\tau) &= \begin{pmatrix} d_\uparrow(\tau) \\ \bar{d}_\downarrow(\tau) \end{pmatrix}, \qquad \bar{\psi}_d(\tau) = \begin{pmatrix} \bar{d}_\uparrow(\tau), & d_\downarrow(\tau) \end{pmatrix}.
\end{aligned}
\tag{2.6}
$$

Using partial integration and anti-periodicity of the Grassman fields, we write the Berry phase term as $\int d\tau \sum_{k\sigma} \bar{c}_{\alpha k \sigma} \partial_\tau c_{\alpha k \sigma} = \int d\tau \sum_k \bar{\psi}_{c\alpha k} \partial_\tau \psi_{c\alpha k}$. We will also transform to Matsubara frequencies $\omega_n = (2n+1)\pi/\beta$.

$$
\begin{aligned}
\psi_{c\alpha k}(\tau) &= \frac{1}{\sqrt{\beta}} \sum_n \psi_{c\alpha k}(i\omega_n) e^{-i\omega_n \tau}, \quad \bar{\psi}_{c\alpha k}(\tau) = \frac{1}{\sqrt{\beta}} \sum_n \bar{\psi}_{c\alpha k}(i\omega_n) e^{i\omega_n \tau}, \\
\psi_d(\tau) &= \frac{1}{\sqrt{\beta}} \sum_n \psi_d(i\omega_n) e^{-i\omega_n \tau}, \qquad \bar{\psi}_d(\tau) = \frac{1}{\sqrt{\beta}} \sum_n \bar{\psi}_d(i\omega_n) e^{i\omega_n \tau}.
\end{aligned}
\tag{2.7}
$$

Using the orthogonality relation $\frac{1}{\beta} \int d\tau \exp[i(\omega_n - \omega_{n'})\tau] = \delta_{n,n'}$, the terms of the action involving the leads become (suppressing the frequency dependence of the fields)

$$S_{\text{S}} = \sum_{\alpha kn} \bar{\psi}_{c\alpha k} \underbrace{\left(-i\omega_n + \xi_{\alpha k}\tau_z - \Delta'_\alpha \tau_x + \Delta''_\alpha \tau_y\right)}_{-\mathcal{G}^{-1}_{0,\alpha k}} \psi_{c\alpha k}, \tag{2.8a}$$

$$S_{\text{S-D}} = \sum_{\alpha kn} \left[\bar{\psi}_{c\alpha k} t_\alpha \tau_z \psi_d + \bar{\psi}_d t_\alpha \tau_z \psi_{c\alpha k}\right], \tag{2.8b}$$

where $\tau_{x,y,z}$ are a set of Pauli matrices acting in electron-hole (Nambu) space and the pairing potential has been decomposed into real and imaginary parts: $\Delta_\alpha = \Delta'_\alpha + i\Delta''_\alpha$. From Eq. (2.8a), we may directly read off the inverse Matsubara Nambu Green function for the electrons in lead α. After inverting it, we find

$$\mathcal{G}_{0,\alpha k}(i\omega_n) = \frac{i\omega_n + \xi_{\alpha k}\tau_z - \Delta'_\alpha \tau_x + \Delta''_\alpha \tau_y}{(i\omega_n)^2 - (\xi^2_{\alpha k} + |\Delta_\alpha|^2)}. \tag{2.9}$$

It will be useful to also calculate the momentum-summed version, i.e.

$$\mathcal{G}_{0,\alpha}(i\omega_n) = \sum_k \mathcal{G}_{0,\alpha k}(i\omega_n) = \nu_{F,\alpha} \int_{-D_\alpha}^{D_\alpha} d\xi_\alpha \, \mathcal{G}_{0,\alpha k}(i\omega_n)$$

$$= 2\nu_{F,\alpha} \arctan\left(\frac{D_\alpha}{\sqrt{|\Delta_\alpha|^2 + \omega_n^2}}\right) \frac{1}{\sqrt{|\Delta_\alpha|^2 + \omega_n^2}} \begin{pmatrix} -i\omega_n & \Delta_\alpha \\ \Delta^*_\alpha & -i\omega_n \end{pmatrix}, \tag{2.10}$$

assuming a constant density of states $\nu_{F,\alpha}$ near the Fermi surface in lead α.

To arrive at an effective action for the electrons on the dot, we consider the partition function and perform the Gaussian integrals over the leads (tildes are used to reserve the effective action for Eq. (2.15)).

$$\tilde{Z} = \int \mathcal{D}[\bar{\psi}_c, \psi_c, \bar{\psi}_d, \psi_d] e^{-S} = \int \mathcal{D}\left[\bar{\psi}_d, \psi_d\right] e^{-\tilde{S}_{\text{eff}}},$$

$$e^{-\tilde{S}_{\text{eff}}[\psi_d, \bar{\psi}_d]} = \int \mathcal{D}[\bar{\psi}_c, \psi_c] e^{-S[\psi_c, \bar{\psi}_c, \psi_d, \bar{\psi}_d]}. \tag{2.11}$$

Completing the square among lead electrons, we find

$$S_{\text{S}} + S_{\text{S-D}} = \sum_{\alpha kn} \left[(\bar{\psi}_{c\alpha k} - \bar{\psi}_d t_\alpha \tau_z \mathcal{G}_{0,\alpha k})(-\mathcal{G}^{-1}_{0,\alpha k})(\psi_{c\alpha k} - \mathcal{G}_{0,\alpha k} t_\alpha \tau_z \psi_d) + t^2_\alpha \bar{\psi}_d \tau_z \mathcal{G}_{0,\alpha k} \tau_z \psi_d\right]. \tag{2.12}$$

Changing variables to $\psi'_{c\alpha k} = \psi_{c\alpha k} - \mathcal{G}_{0,\alpha k} t_\alpha \tau_z \psi_d$, $\bar{\psi}'_{c\alpha k} = \bar{\psi}_{c\alpha k} - \bar{\psi}_d t_\alpha \tau_z \mathcal{G}_{0,\alpha k}$, the measure is unchanged $\mathcal{D}[\psi'_c, \bar{\psi}'_c] = \mathcal{D}[\psi_c, \bar{\psi}_c]$, and we may perform the Gaussian integral. Comparing

with Eq. (2.11), we find

$$\tilde{S}_{\text{eff}} = S_{\text{D}} + \sum_n \bar{\psi}_d(i\omega_n)\Sigma_d(i\omega_n)\psi_d(i\omega_n) - \ln\left(\det\left(-\mathcal{G}_0^{-1}\right)\right), \tag{2.13}$$

with self-energy

$$\begin{aligned}
\Sigma_d(i\omega_n) &= \sum_{\alpha k} t_\alpha^2 \tau_z \mathcal{G}_{0,\alpha k}(i\omega_n)\tau_z \\
&= -\sum_\alpha \frac{2}{\pi}\arctan\left(\frac{D_\alpha}{\sqrt{|\Delta_\alpha|^2 + \omega_n^2}}\right)\frac{\Gamma_\alpha}{\sqrt{|\Delta_\alpha|^2 + \omega_n^2}}\begin{pmatrix} i\omega_n & \Delta_\alpha \\ \Delta_\alpha^* & i\omega_n \end{pmatrix},
\end{aligned} \tag{2.14}$$

where $\Gamma_\alpha = \pi\nu_{F,\alpha}t_\alpha^2$ is the tunneling rate between lead α and the QD. We define the total hybridization as the sum of the individual contributions: $\Gamma = \sum_\alpha \Gamma_\alpha$. The second equality follows from Eq. (2.10).

The last term in Eq. (2.13) is unimportant for the physics of the QD since it depends on the leads only. Therefore, let us define the effective action as

$$S_{\text{eff}} = S_{\text{D}} + \sum_n \bar{\psi}_d(i\omega_n)\Sigma_d(i\omega_n)\psi_d(i\omega_n). \tag{2.15}$$

Due to the interacting term in S_{D} (see Eq. (2.5b)), the problem is not analytically solvable in general and we have to study the problem in certain limits. The infinite gap/low energy limit is (analytically) the easiest way to proceed and will, therefore, be our first order of business.

3   The proximitized QD in the infinite gap limit

Let us consider the limit $\omega \ll |\Delta_\alpha|$, i.e. the low-energy or infinite gap limit. This means we may neglect the diagonal entries in the self-energy (Eq. (2.14)) and approximate $\sqrt{|\Delta_\alpha|^2 + \omega_n^2} \simeq |\Delta_\alpha|$. Then the self-energy becomes static and takes the form

$$\Sigma_d = -\begin{pmatrix} 0 & \gamma \\ \gamma^* & 0 \end{pmatrix}, \tag{3.1}$$

where the effect of coupling to the leads is contained in a single complex parameter

$$\gamma = \sum_\alpha \frac{2}{\pi}\arctan\left(\frac{D_\alpha}{|\Delta_\alpha|}\right)\Gamma_\alpha e^{i\varphi_\alpha}. \tag{3.2}$$

Interestingly, in this limit where the continuum states in the leads are inaccessible, the effect of the leads boils down to an 'interference' problem governed by the tunneling amplitudes Γ_α and lead phases φ_α. No matter the number of leads, the QD is only concerned with two degrees of freedom, e.g. the magnitude and phase of γ. Clearly, then, all results from single or two-lead systems in the infinite gap limit, expressed in terms of γ, also apply to multiterminal systems.

The effective action for the electrons on the QD (Eq. (2.15)) takes the form

$$S_{\text{eff}}^{(\infty)} = \int_0^\beta \mathrm{d}\tau \left\{ \sum_\sigma \bar{d}_\sigma \partial_\tau d_\sigma + \underbrace{\sum_\sigma \epsilon_d \bar{d}_\sigma d_\sigma - \gamma \bar{d}_\uparrow \bar{d}_\downarrow - \gamma^* d_\downarrow d_\uparrow + U \bar{d}_\uparrow \bar{d}_\downarrow d_\downarrow d_\uparrow}_{\tilde{H}_\infty[\bar{d},d]} \right\}. \qquad (3.3)$$

Since the self-energy is static, we may directly read off the (normal-ordered) Hamiltonian $\tilde{H}_\infty[d^\dagger, d]$ leading to this action.

$$\tilde{H}_\infty[d^\dagger, d] = \sum_\sigma \epsilon_d d_\sigma^\dagger d_\sigma - \gamma d_\uparrow^\dagger d_\downarrow^\dagger - \gamma^* d_\downarrow d_\uparrow + U d_\uparrow^\dagger d_\downarrow^\dagger d_\downarrow d_\uparrow. \qquad (3.4)$$

In this form, the proximity effect of the superconducting leads is directly apparent through the anomalous terms. Hence, the infinite gap limit is also referred to as the "proximitized limit" or sometimes the "atomic limit" (we take this to mean no hybridization – see Section 1.4).

To write it in a particle-hole symmetric form, we consider the fermionic identity $(n_d - 1)^2 = 2n_{d\uparrow}n_{d\downarrow} - n_d + 1$; it follows from Pauli's exclusion principle that $n_{d\sigma}^2 = n_{d\sigma}$. Then we may write the effective low-energy Hamiltonian as

$$H_\infty = \xi_d n_d - \gamma d_\uparrow^\dagger d_\downarrow^\dagger - \gamma^* d_\downarrow d_\uparrow + \frac{U}{2}(n_d - 1)^2, \qquad (3.5)$$

where $\xi_d = \epsilon_d + U/2$. Note that the zero point energy has been raised by $U/2$ compared to Eq. (3.4), hence the tilde. The particle-hole symmetric point is $\xi_d = 0$ or equivalently $\epsilon_d = -U/2$. At this point, the Hamiltonian is unchanged under the transformation $d_\sigma \leftrightarrow d_\sigma^\dagger$, $c_{\alpha k\sigma} \leftrightarrow c_{\alpha k\sigma}^\dagger$; this entails $n_{d\sigma} \to 1 - n_{d\sigma}$ and $\gamma \leftrightarrow -\gamma^*$.

The Hamiltonian only lives in a 4-dimensional Hilbert space spanned by the states $|0\rangle, |\sigma\rangle = d_\sigma^\dagger |0\rangle, |\uparrow\downarrow\rangle = d_\uparrow^\dagger d_\downarrow^\dagger |0\rangle$. The Hamiltonian is easily diagonalized since it may be decoupled into an odd and an even parity sector, yielding two uncoupled 2×2 matrices. The odd parity, singly occupied eigenstates $|\sigma\rangle$ form a doublet with energy $E_\sigma^0 = \xi_d$. The superscript is placed in anticipation of the perturbation corrections to be discussed

in Section 4. The even parity base kets given by the empty and doubly occupied states $|0\rangle, |\uparrow\downarrow\rangle$, mix and form BCS-like eigenstates with energies $E_\pm^0 = \xi_d + U/2 \pm E_A$ where $E_A = \sqrt{\xi_d^2 + |\gamma|^2}$. We will label the states $|\pm\rangle$ and they may explicitly be written as

$$|+\rangle = -ve^{-i\zeta}|0\rangle + u|\uparrow\downarrow\rangle, \qquad |-\rangle = u|0\rangle + ve^{i\zeta}|\uparrow\downarrow\rangle, \tag{3.6}$$

where the real coefficients u, v are given by

$$u = \frac{1}{\sqrt{2}}\sqrt{1 + \frac{\xi_d}{E_A}}, \quad v = \frac{1}{\sqrt{2}}\sqrt{1 - \frac{\xi_d}{E_A}}, \tag{3.7}$$

and ζ is the phase of the tunneling parameter $\gamma = |\gamma|e^{i\zeta}$.

It is clear that the energies of the even parity states depend on the tunneling couplings to the leads Γ_α and on the phases of the leads φ_α through the parameter γ (see Eq. (3.2)); the doublet energy is independent of γ. In analogy with crystal momentum on a lattice with translational symmetry, the superconductor phases $\varphi_\alpha \in [0, 2\pi)$ define a periodic first Brillouin zone. In Fig. 3.1, the 'band structure' is shown for different three-terminal junctions in the limit of infinite electronic bandwidth $D_\alpha/|\Delta_\alpha| \to \infty$. Depending on the position in phase-space (φ_1, φ_2), the ground state of the QD is either the singlet $|-\rangle$ or the doublet $|\sigma\rangle$. At the so-called Weyl nodes, the even parity eigenstates are degenerate which occurs when $\xi_d = 0$ and $\gamma = 0$. These nodes are seen in Fig. 3.1(a) and Fig. 3.1(c) and may be associated with topological charges which always come in pairs with opposite sign in this model. At very strong coupling asymmetry, $\max(\Gamma_\alpha) > \Gamma/2$, there are no solutions to the equation $\gamma = 0$ and, hence, no Weyl nodes in Fig. 3.1(e). In appendix A we show that the topology is indeed trivial (zero Chern number) in the model considered here. Klees $et\ al.$ [14] showed, however, that an additional tunneling term between neighboring leads gives rise to non-trivial topological phases (nonzero Chern number). Then, the Weyl points are also protected against deviations away from particle-hole symmetry.

The phase diagram for the QD is very simple in the infinite gap limit. The phase transition between doublet and singlet ground states occurs when $E_-^0 = E_\sigma^0$ which is equivalent to $\xi_d^2 + |\gamma|^2 = U^2/4$. The levels are allowed to cross since they come from sectors of H_∞ with different parity. The phase diagram is shown in Fig. 3.2 and illustrates the competition between local Coulomb repulsion and the proximity effect. Around the particle-hole symmetric point $\xi_d = 0$, the doublet phase $|\sigma\rangle$ is stabilized for small tunneling rates. However, as the tunneling is increased, the phase transition eventually occurs and the QD favors the BCS-like singlet state $|-\rangle$. Note also that, at the Weyl nodes from Fig. 3.1, the doublet phase is favoured when $-U/2 < \xi_d < U/2$ since $\gamma = 0$.
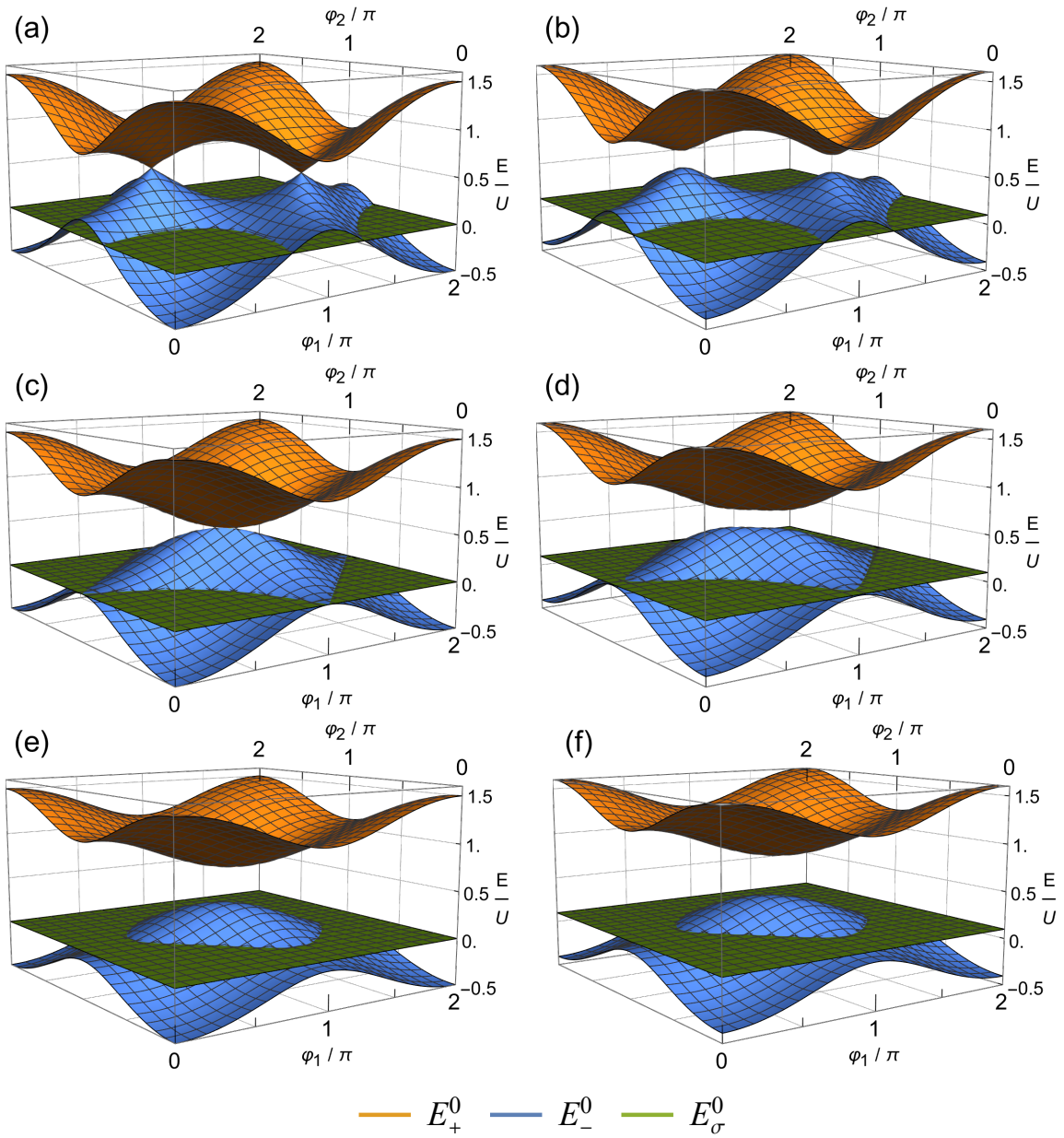
Figure 3.1: Infinite gap multi-particle eigenenergies for three-terminal junctions as function of two independent lead phases; the last phase is fixed by our gauge $\varphi_3 = 0$. For simplicity, we consider infinite electronic bandwidth $D_\alpha/|\Delta_\alpha| \to \infty$. The top row (a), (b) uses a symmetric coupling $\Gamma_1 = \Gamma_2 = \Gamma_3 = U/3$, while the second row (c), (d) introduces an asymmetry $\Gamma_1 = \Gamma_2 = U/4, \Gamma_3 = U/2$, and the bottom row (e), (f) uses stronger asymmetry $\Gamma_1 = \Gamma_2 = U/5, \Gamma_3 = 3U/5$. The left column (a), (c), (e) is at particle-hole symmetry ($\xi_d = 0$), while the right column (b), (d), (f) has $\xi_d = 0.1\,U$. At particle-hole symmetry ($\xi_d = 0$), Weyl nodes are found where $\gamma = 0$; solutions are possible when $\max(\Gamma_\alpha) \leq \Gamma/2$.
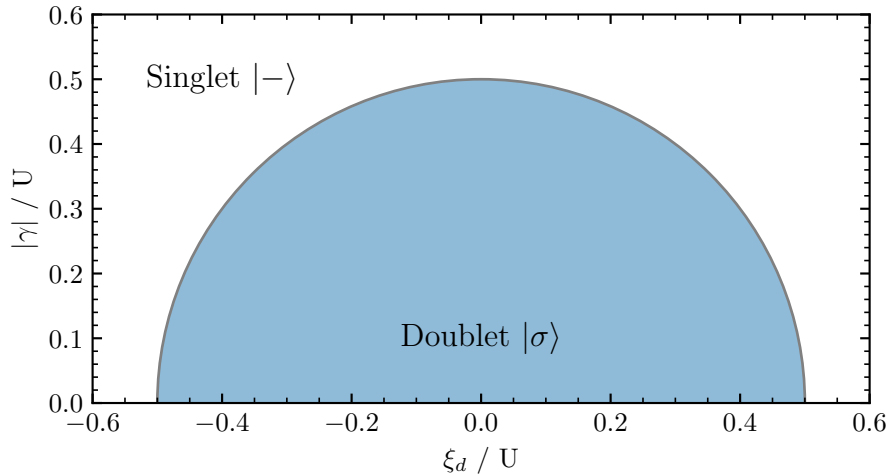
Figure 3.2: Infinite gap phase diagram for the QD showing the transition between the singlet $|-\rangle$ and doublet $|\sigma\rangle$ ground states at $\xi_d^2 + |\gamma|^2 = U^2/4$.

4   First order energy corrections to the infinite gap limit

To extend our discussion to finite superconducting gaps, we apply perturbation theory to the infinite gap limit as done by Meng & Florens & Simon [15] in the case of $N = 2$ leads. We follow their methods and generalize the results to an arbitrary number of leads. In the end, we will find the energy shifts from the infinite gap energy levels and new phase diagrams. Later, we will refer to this as the "MFS" model.

We start from Eq. (2.15) and split the effective action on the QD into an unperturbed infinite gap action and collect the rest as a perturbation. Transforming to imaginary time, the self energy is

$$\Sigma_d(\tau) = \frac{1}{\beta} \sum_n \Sigma_d(i\omega_n) e^{-i\omega_n \tau}, \tag{4.1}$$

such that Eq. (2.15) expands to

$$
S_{\text{eff}} = \int_0^\beta \mathrm{d}\tau \sum_\sigma \bar{d}_\sigma(\tau)(\partial_\tau + \epsilon_d) d_\sigma(\tau) + U \bar{d}_\uparrow(\tau) \bar{d}_\downarrow(\tau) d_\downarrow(\tau) d_\uparrow(\tau)
$$
$$
+ \int_0^\beta \mathrm{d}\tau \int_0^\beta \mathrm{d}\tau' \, \bar{\psi}_d(\tau) \Sigma_d(\tau - \tau') \psi_d(\tau'). \tag{4.2}
$$

We write this as $S_{\text{eff}} = S_{\text{eff}}^{(\infty)} + S_{\text{pert}}$. The infinite gap action $S_{\text{eff}}^{(\infty)}$ is given by Eq. (3.3)

and by comparison with Eq. (4.2), the perturbation is seen to be

$$S_{\text{pert}} = \int_0^\beta d\tau \int_0^\beta d\tau' \, \bar{\psi}_d(\tau) \Sigma_d(\tau - \tau') \psi_d(\tau') + \int_0^\beta d\tau \left[\gamma \bar{d}_\uparrow(\tau) \bar{d}_\downarrow(\tau) + \gamma^* d_\downarrow(\tau) d_\uparrow(\tau) \right]. \quad (4.3)$$

Perturbation theory amounts to expanding the partition function in powers of S_{pert}. Expanding to linear order, we find

$$Z = \int \mathcal{D}[\bar{d}, d] e^{-S_{\text{eff}}} \approx \int \mathcal{D}[\bar{d}, d](1 - S_{\text{pert}}) e^{-S_{\text{eff}}^{(\infty)}} = Z_0 - Z_0 \langle S_{\text{pert}} \rangle_0. \quad (4.4)$$

The subscript zero indicates that the unperturbed infinite gap distribution function is used to evaluate the path integral, i.e. $Z_0 \langle \cdots \rangle_0 = \int \mathcal{D}[\bar{d}, d](\cdots) e^{-S_{\text{eff}}^{(\infty)}}$ and $Z_0 = \int \mathcal{D}[\bar{d}, d] e^{-S_{\text{eff}}^{(\infty)}}$. Sufficiently close (we will see what this means later) to the infinite gap limit, this linear expansion describes the system well. If we introduce the infinite gap single-particle Nambu Green function for electrons on the QD

$$\mathcal{G}_{0,d}^{\alpha\beta}(\tau - \tau') = - \left\langle T \psi_{d\alpha}(\tau) \psi_{d\beta}^\dagger(\tau') \right\rangle_0 = - \frac{\int \mathcal{D}[\bar{d}, d] \psi_{d\alpha}(\tau) \bar{\psi}_{d\beta}(\tau') e^{-S_{\text{eff}}^{(\infty)}}}{\int \mathcal{D}[\bar{d}, d] e^{-S_{\text{eff}}^{(\infty)}}}, \quad (4.5)$$

that only depends on the time difference due to time translation symmetry, we may write

$$\begin{aligned} \langle S_{\text{pert}} \rangle_0 &= \int_0^\beta d\tau \int_0^\beta d\tau' \, \Sigma_d^{\alpha\beta}(\tau - \tau') \mathcal{G}_{0,d}^{\beta\alpha}(\tau' - \tau) + \int_0^\beta d\tau \, \gamma \mathcal{G}_{0,d}^{21}(0) + \gamma^* \mathcal{G}_{0,d}^{12}(0), \\ &= \beta \int_0^\beta d\tau \, \Sigma_d^{\alpha\beta}(\tau) \mathcal{G}_{0,d}^{\beta\alpha}(-\tau) + \beta\gamma \mathcal{G}_{0,d}^{21}(0) + \beta\gamma^* \mathcal{G}_{0,d}^{12}(0), \end{aligned} \quad (4.6)$$

with an implicit sum over Nambu matrix indices $\alpha, \beta \in \{1, 2\}$. The last equality reduces the double integral to a single integral – this follows from Fourier transformation. To proceed further, we need the imaginary time self-energy and QD Green functions.

The self-energy may be written as (Eq. (2.14))

$$\Sigma_d(\tau) = \sum_{\alpha k} t_\alpha^2 \tau_z \mathcal{G}_{0,\alpha k}(\tau) \tau_z = \sum_{\alpha k} t_\alpha^2 \begin{pmatrix} \mathcal{G}_{0,\alpha k}^{11}(\tau) & -\mathcal{G}_{0,\alpha k}^{12}(\tau) \\ -\mathcal{G}_{0,\alpha k}^{21}(\tau) & \mathcal{G}_{0,\alpha k}^{22}(\tau) \end{pmatrix}. \quad (4.7)$$

The imaginary time Nambu Green functions for electrons in lead α are derived in Appendix B through Fourier transformation of Eq. (2.9) and restated here:

$$\sum_k \mathcal{G}_{0,\alpha k}^{11}(\tau) = -\sum_k \frac{1}{2} f(E_{\alpha k}) \left(e^{E_{\alpha k}(\beta - \tau)} + e^{E_{\alpha k}\tau} \right), \quad 0 < \tau < \beta, \quad (4.8a)$$

$$\mathcal{G}_{0,\alpha k}^{12}(\tau) = \frac{\Delta_\alpha}{2E_{\alpha k}} f(E_{\alpha k}) \left(e^{E_{\alpha k}(\beta - \tau)} - e^{E_{\alpha k}\tau} \right), \quad 0 < \tau < \beta. \quad (4.8b)$$

We use the shorthand notation $E_{\alpha k} = \sqrt{\xi_{\alpha k}^2 + |\Delta_\alpha|^2}$ for quasiparticle energies in lead α and $f(z) = [\exp(\beta z) + 1]^{-1}$ for the Fermi function. The two other components are found from $\sum_k \mathcal{G}_{0,\alpha k}^{22}(\tau) = \sum_k \mathcal{G}_{0,\alpha k}^{11}(\tau)$, $\mathcal{G}_{0,\alpha k}^{21}(\tau) = \mathcal{G}_{0,\alpha k}^{12}(\tau)^*$.

The QD Green functions are a little more cumbersome to derive. In the infinite gap limit, we consider the interactions as they are – it is exact in U. Therefore, if we attempted to use the equations of motion to derive the single-particle Green function $\mathcal{G}_{0,d}$, we would soon run into problems due to these interactions. We would find that $\mathcal{G}_{0,d}$ couples to a two-particle Green function. The two-particle Green function couples to a three-particle one and so on. We would not be able to find a closed system of equations for $\mathcal{G}_{0,d}$. Furthermore, due to interactions, it is not possible to apply Wick's theorem that reduces many-particle Green functions to a sum of products of single-particle Green functions.

However, since we actually do know the many-particle eigenstates in the infinite gap limit, we may instead use the Lehmann representation and calculate the QD Green functions in this way. Then, we simply take statistical averages where each state is weighted by a Boltzmann factor: $Z_0 \langle \cdots \rangle_0 = \sum_{n_0} e^{-\beta E_n^0} \langle n_0 | \cdots | n_0 \rangle$ using the eigenstates (Eq. (3.6)) $|n_0\rangle \in \{|\uparrow\rangle, |\downarrow\rangle, |+\rangle, |-\rangle\}$ and with normalization $Z_0 = \sum_{n_0} e^{-\beta E_n^0}$.

Terms of the form $\langle A_H(\tau) B_H(0) \rangle_0$ need to be evaluated when calculating single-particle Green functions. Here, $A_H(\tau), B_H(\tau)$ are operators in the Heisenberg representation. The time evolution is governed by the unperturbed infinite gap Hamiltonian (Eq. (3.5)), e.g. $A_H(\tau) = e^{H_\infty \tau} A_S e^{-H_\infty \tau}$ with A_S given in the Schrödinger representation.

We may write the QD Nambu Green function (Eq. (4.5)) explicitly as

$$\mathcal{G}_{0,d}(-\tau) = \begin{pmatrix} \left\langle d_\uparrow^\dagger(\tau) d_\uparrow(0) \right\rangle_0 & \left\langle d_\downarrow(\tau) d_\uparrow(0) \right\rangle_0 \\ \left\langle d_\uparrow^\dagger(\tau) d_\downarrow^\dagger(0) \right\rangle_0 & \left\langle d_\downarrow(\tau) d_\downarrow^\dagger(0) \right\rangle_0 \end{pmatrix}, \quad 0 < \tau < \beta. \tag{4.9}$$

The statistical averages are evaluated in Appendix C. They end up being

$$Z_0 \left\langle d_\uparrow^\dagger(\tau) d_\uparrow(0) \right\rangle_0 = u^2 \left(e^{-E_-^0 \tau} e^{-E_\sigma^0 (\beta - \tau)} + e^{-E_\sigma^0 \tau} e^{-E_+^0 (\beta - \tau)} \right)$$
$$+ v^2 \left(e^{-E_+^0 \tau} e^{-E_\sigma^0 (\beta - \tau)} + e^{-E_\sigma^0 \tau} e^{-E_-^0 (\beta - \tau)} \right), \tag{4.10a}$$

$$Z_0 \left\langle d_\downarrow(\tau) d_\downarrow^\dagger(0) \right\rangle_0 = u^2 \left(e^{-E_+^0 \tau} e^{-E_\sigma^0 (\beta - \tau)} + e^{-E_\sigma^0 \tau} e^{-E_-^0 (\beta - \tau)} \right)$$
$$+ v^2 \left(e^{-E_-^0 \tau} e^{-E_\sigma^0 (\beta - \tau)} + e^{-E_\sigma^0 \tau} e^{-E_+^0 (\beta - \tau)} \right), \tag{4.10b}$$

$$Z_0 \left\langle d_\uparrow^\dagger(\tau) d_\downarrow^\dagger(0) \right\rangle_0 = uv e^{-i\zeta} \left(e^{-E_+^0 \tau} e^{-E_\sigma^0 (\beta - \tau)} + e^{-E_\sigma^0 \tau} e^{-E_-^0 (\beta - \tau)} \right.$$
$$\left. - e^{-E_-^0 \tau} e^{-E_\sigma^0 (\beta - \tau)} - e^{-E_\sigma^0 \tau} e^{-E_+^0 (\beta - \tau)} \right) \tag{4.10c}$$
$$= Z_0 \left\langle d_\downarrow(\tau) d_\uparrow(0) \right\rangle_0^* .$$

Note that if we exchange E_+^0 and E_-^0 on the RHS of Eq. (4.10a), we get the RHS of Eq. (4.10b) and vice versa; i.e. $\left\langle d_\uparrow^\dagger(\tau) d_\uparrow(0) \right\rangle_0 \overset{+\leftrightarrow-}{\longleftrightarrow} \left\langle d_\downarrow(\tau) d_\downarrow^\dagger(0) \right\rangle_0$.

Let us now return to Eq. (4.6) and evaluate the first order correction to the partition function $Z_0 \left\langle S_{\text{pert}} \right\rangle_0$. Inserting the expressions for the Green functions and performing the time integral, the diagonal terms give

$$Z_0 \beta \int_0^\beta \mathrm{d}\tau \, \Sigma_d^{11}(\tau) \mathcal{G}_{0,d}^{11}(-\tau) + \Sigma_d^{22}(\tau) \mathcal{G}_{0,d}^{22}(-\tau)$$
$$= -\beta \sum_{\substack{\alpha k \\ s=+,-}} t_\alpha^2 f(E_{\alpha k}) \left[\frac{e^{\beta(E_{\alpha k} - E_s^0)} - e^{-\beta E_\sigma^0}}{E_{\alpha k} - (E_s^0 - E_\sigma^0)} + \frac{e^{\beta(E_{\alpha k} - E_\sigma^0)} - e^{-\beta E_s^0}}{E_{\alpha k} + (E_s^0 - E_\sigma^0)} \right], \quad (4.11)$$

while the off-diagonal terms give

$$Z_0 \beta \int_0^\beta \mathrm{d}\tau \, \Sigma_d^{12}(\tau) \mathcal{G}_{0,d}^{21}(-\tau) + \Sigma_d^{21}(\tau) \mathcal{G}_{0,d}^{12}(-\tau)$$
$$= 2uv\beta \sum_{\alpha k} t_\alpha^2 \frac{\mathrm{Re}(\Delta_\alpha e^{-i\zeta})}{E_{\alpha k}} f(E_{\alpha k}) \left(\left[\frac{e^{\beta(E_{\alpha k} - E_+^0)} - e^{-\beta E_\sigma^0}}{E_{\alpha k} - (E_+^0 - E_\sigma^0)} \right. \right.$$
$$\left. \left. - \frac{e^{\beta(E_{\alpha k} - E_\sigma^0)} - e^{-\beta E_+^0}}{E_{\alpha k} + (E_+^0 - E_\sigma^0)} \right] - [+ \to -] \right). \tag{4.12}$$

Here, $\mathrm{Re}(z)$ denotes the real part of z. The final two terms evaluate to

$$Z_0 \beta \left[\gamma \mathcal{G}_{0,d}^{21}(0) + \gamma^* \mathcal{G}_{0,d}^{12}(0) \right] = 2\beta |\gamma| uv \left(e^{-\beta E_-^0} - e^{-\beta E_+^0} \right). \tag{4.13}$$

Due to the perturbation, the energy levels are shifted compared to the infinite gap limit. To first order in S_{pert}, the four energy levels are $E_\pm = E_\pm^0 + \delta E_\pm$ and $E_\sigma = E_\sigma^0 + \delta E_\sigma$. Since there is symmetry between spin up and down electrons in the system, we will still find a doublet state, i.e. $E_\uparrow = E_\downarrow$. To determine the energy shifts, we consider the low temperature limit, specifically $\delta E_{\sigma(\pm)} \ll T \ll E_{\alpha k}$. To maintain lead superconductivity, we require $T \ll |\Delta_\alpha| < E_{\alpha k}$, and the condition $\delta E_{\sigma(\pm)} \ll T$ allows us to expand the partition function (again).

In the limit $T \ll E_{\alpha k}$, $f(E_{\alpha k}) = e^{-\beta E_{\alpha k}}$ and terms that scale as $\sim e^{-\beta E_{\alpha k}}$ are exponentially suppressed and negligible at low temperatures since $E_{\alpha k} > 0$. Then, combining Eqs. (4.11)–(4.13), the partition function is given by

$$
\begin{aligned}
Z \approx Z_0 \\
+ \beta \sum_{\alpha k} t_\alpha^2 \Bigg\{ \sum_{s=+,-} \left[\frac{e^{-\beta E_s^0}}{E_{\alpha k} - (E_s^0 - E_\sigma^0)} + \frac{e^{-\beta E_\sigma^0}}{E_{\alpha k} + (E_s^0 - E_\sigma^0)} \right] \\
- 2uv \frac{\operatorname{Re}(\Delta_\alpha e^{-i\zeta})}{E_{\alpha k}} \left(\left[\frac{e^{-\beta E_+^0}}{E_{\alpha k} - (E_+^0 - E_\sigma^0)} - \frac{e^{-\beta E_\sigma^0}}{E_{\alpha k} + (E_+^0 - E_\sigma^0)} \right] - [+ \to -] \right) \Bigg\} \\
- 2\beta uv |\gamma| \left(e^{-\beta E_-^0} - e^{-\beta E_+^0} \right) .
\end{aligned}
$$

$$(4.14)$$

On the other hand, given the energy levels $E_\sigma, E_\pm$, we can also expand the partition function according to

$$
Z = \sum_\sigma e^{-\beta E_\sigma} + e^{-\beta E_+} + e^{-\beta E_-} = \sum_\sigma e^{-\beta(E_\sigma^0 + \delta E_\sigma)} + e^{-\beta(E_+^0 + \delta E_+)} + e^{-\beta(E_-^0 + \delta E_-)}
$$

$$
\approx Z_0 - \beta \left(\sum_\sigma \delta E_\sigma e^{-\beta E_\sigma^0} + \delta E_+ e^{-\beta E_+^0} + \delta E_- e^{-\beta E_-^0} \right) .
$$

$$(4.15)$$

This is valid for energy shifts much smaller than the temperature $\delta E_{\sigma(\pm)} \ll T$. Comparing

coefficients in front of the Boltzmann factors, we find

$$\delta E_\sigma = -\sum_{\alpha k} \frac{t_\alpha^2}{2} \left\{ \frac{1}{E_{\alpha k} + (E_+^0 - E_\sigma^0)} + \frac{1}{E_{\alpha k} + (E_-^0 - E_\sigma^0)} \right.$$
$$\left. + 2uv \frac{\text{Re}(\Delta_\alpha e^{-i\zeta})}{E_{\alpha k}} \left[\frac{1}{E_{\alpha k} + (E_+^0 - E_\sigma^0)} - \frac{1}{E_{\alpha k} + (E_-^0 - E_\sigma^0)} \right] \right\}, \tag{4.16a}$$

$$\delta E_+ = -\sum_{\alpha k} t_\alpha^2 \left\{ \left[1 - 2uv \frac{\text{Re}(\Delta_\alpha e^{-i\zeta})}{E_{\alpha k}} \right] \frac{1}{E_{\alpha k} - (E_+^0 - E_\sigma^0)} \right\} - 2uv|\gamma|, \tag{4.16b}$$

$$\delta E_- = -\sum_{\alpha k} t_\alpha^2 \left\{ \left[1 + 2uv \frac{\text{Re}(\Delta_\alpha e^{-i\zeta})}{E_{\alpha k}} \right] \frac{1}{E_{\alpha k} - (E_-^0 - E_\sigma^0)} \right\} + 2uv|\gamma|. \tag{4.16c}$$

We note that for $N = 2$ identical leads with symmetric coupling, this reduces to the energy corrections found by Meng & Florens & Simon [15]. Already now, we may expect to run into some divergence problems when $E_\pm^0 - E_\sigma^0 \simeq \pm|\Delta_\alpha|$ and the denominators approach zero. This is indeed a problem we need to deal with shortly.

For now, let us evaluate the momentum summations. We do this inside the lead summations so the lead index α will be suppressed in the following. In the thermodynamic limit, we may replace the discrete summations with continuous integrals: $\sum_k (\cdots) \to \nu_F \int_{-D}^D d\xi \, (\cdots)$. This will leave us with two types of integrals: I_1 and I_2 – both with analytic solutions. Using the trigonometric substitutions $\xi = |\Delta| \tan\theta$ and $x = \tan(\theta/2)$, one may show I_1 and I_2 are related to the same, dimensionless integral I. Introducing the notation $E(\xi) = \sqrt{\xi^2 + |\Delta|^2}$, we have

$$I_1(E') = \int_0^D d\xi \, \frac{1}{E(\xi) - E'} = 2 \frac{E'}{|\Delta|} I\left(\frac{E'}{|\Delta|}\right) + L\left(\frac{|\Delta|}{D}\right), \tag{4.17}$$

$$I_2(E') = \int_0^D d\xi \, \frac{1}{E(\xi)} \frac{1}{E(\xi) - E'} = \frac{2}{|\Delta|} I\left(\frac{E'}{|\Delta|}\right). \tag{4.18}$$

The term $L\left(\frac{|\Delta|}{D}\right) = \ln\left(\frac{1+x_{\max}}{1-x_{\max}}\right)$ with $x_{\max} = -\frac{|\Delta|}{D} + \sqrt{1 + \frac{|\Delta|^2}{D^2}}$ comes from partial fraction decomposition and describes the logarithmic divergence with increasing bandwidth. The principal value of I is given by

$$I(c) = \mathcal{P} \int_0^{x_{\max}} dx \, \frac{1}{1 - c + (1 + c)x^2} = \begin{cases} \infty, & c = 1 \\ x_{\max}/2, & c = -1 \\ \frac{-\text{sgn}(c)}{2\sqrt{c^2-1}} \ln\left(\frac{x_{\max}+x_*}{|x_{\max}-x_*|}\right), & |c| > 1 \\ \frac{1}{\sqrt{1-c^2}} \arctan(x_{\max}/x_*), & |c| < 1 \end{cases}. \tag{4.19}$$
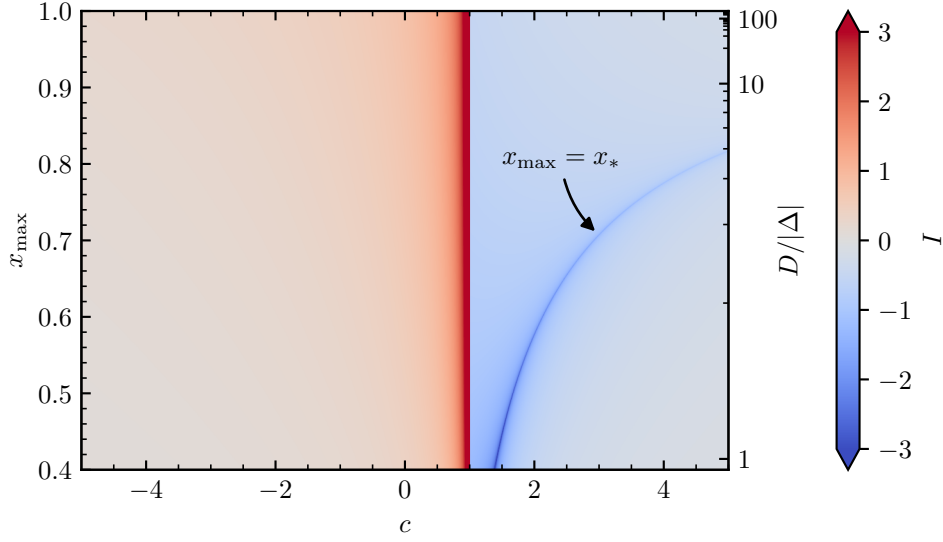
Figure 4.1: The integral I (see Eq. (4.19)) for different values of $x_{\max}$ and c. The vertical axis on the RHS relates $D/|\Delta|$ to $x_{\max}$ through $x_{\max} = -\frac{|\Delta|}{D} + \sqrt{1 + \frac{|\Delta|^2}{D^2}}$. The integral I diverges on the lines $c = 1$ and $x_{\max} = x_*$.

The integrand diverges at $x_* = \sqrt{\left|\frac{c-1}{c+1}\right|}$ when $|c| > 1$, giving rise to a divergence of the whole integral when the upper limit of integration is set to this value: $x_{\max} = x_*$. I also diverges when $c = 1$ and the integrand is $1/(2x^2)$. Apart from these two lines, the integral is well behaved. The value of I is plotted in Fig. 4.1 for different arguments c and upper limits $x_{\max}$ in the region $D > |\Delta|$, corresponding to $\sqrt{2} - 1 < x_{\max} < 1$. The integral is positive for $c < 1$ and negative for $c > 1$.

In terms of I, the energy corrections (Eq. (4.16)) are given by

$$\delta E_\sigma = -\frac{2}{\pi} \sum_\alpha \Gamma_\alpha \left\{ \frac{E_\sigma^0 - E_+^0}{|\Delta_\alpha|} I\left(\frac{E_\sigma^0 - E_+^0}{|\Delta_\alpha|}\right) + \frac{E_\sigma^0 - E_-^0}{|\Delta_\alpha|} I\left(\frac{E_\sigma^0 - E_-^0}{|\Delta_\alpha|}\right) + L\left(\frac{|\Delta_\alpha|}{D_\alpha}\right) \right.$$
$$\left. + 2uv\cos(\varphi_\alpha - \zeta)\left[I\left(\frac{E_\sigma^0 - E_+^0}{|\Delta_\alpha|}\right) - I\left(\frac{E_\sigma^0 - E_-^0}{|\Delta_\alpha|}\right)\right] \right\},$$

$$(4.20a)$$

$$\delta E_\pm = -\frac{2}{\pi} \sum_\alpha \Gamma_\alpha \left\{ \left[\frac{E_\pm^0 - E_\sigma^0}{|\Delta_\alpha|} \mp 2uv\cos(\varphi_\alpha - \zeta)\right] 2I\left(\frac{E_\pm^0 - E_\sigma^0}{|\Delta_\alpha|}\right) + L\left(\frac{|\Delta_\alpha|}{D_\alpha}\right) \right\} \mp 2uv|\gamma|.$$

$$(4.20b)$$

Note that all energy levels are shifted by the same logarithmic term L, meaning energy

differences will not depend on this. Just as we anticipated, our perturbation corrections break down when the infinite gap energy differences approach the gap $E_\pm^0 - E_\sigma^0 \simeq |\Delta_\alpha|$ or $E_\sigma^0 - E_-^0 \simeq |\Delta_\alpha|$, and I diverges.

To extend the validity of Eq. (4.20), Meng & Florens & Simon [15] proposed to renormalize the energy levels through a "self-consistency condition inspired by Brillouin-Wigner perturbation theory" that re-sums the divergences. Their method corresponds to self-consistently renormalizing the even parity energy levels $E_\pm$ and leaving the odd parity energy level E_σ as stated in Eq. (4.20a). It may seem odd to only have self-consistent equations for some energy levels and not all, but it takes care of the divergences and fits well with NRG data as we shall see.

Consider the energy differences $a = E_- - E_\sigma$ and $b = E_+ - E_\sigma$ between the two singlets and the doublet. Let us denote the unperturbed infinite gap energy differences by $a_0 = E_-^0 - E_\sigma^0$ and $b_0 = E_+^0 - E_\sigma^0$, and the first order corrections by $\delta a = \delta E_- - \delta E_\sigma$ and $\delta b = \delta E_+ - \delta E_\sigma$ such that $a = a_0 + \delta a$ and $b = b_0 + \delta b$. The self-consistency conditions then yield

$$
\delta a = -\frac{2}{\pi} \sum_\alpha \Gamma_\alpha \left\{ \frac{2a}{|\Delta_\alpha|} I\left(\frac{a}{|\Delta_\alpha|}\right) + \frac{b_0}{|\Delta_\alpha|} I\left(\frac{-b_0}{|\Delta_\alpha|}\right) + \frac{a_0}{|\Delta_\alpha|} I\left(\frac{-a_0}{|\Delta_\alpha|}\right) \right.
$$
$$
\left. + 2uv\cos(\varphi_\alpha - \zeta)\left[2I\left(\frac{a}{|\Delta_\alpha|}\right) - I\left(\frac{-b_0}{|\Delta_\alpha|}\right) + I\left(\frac{-a_0}{|\Delta_\alpha|}\right)\right] \right\} + 2uv|\gamma|,
$$
$$(4.21a)$$

$$
\delta b = -\frac{2}{\pi} \sum_\alpha \Gamma_\alpha \left\{ \frac{2b}{|\Delta_\alpha|} I\left(\frac{b}{|\Delta_\alpha|}\right) + \frac{b_0}{|\Delta_\alpha|} I\left(\frac{-b_0}{|\Delta_\alpha|}\right) + \frac{a_0}{|\Delta_\alpha|} I\left(\frac{-a_0}{|\Delta_\alpha|}\right) \right.
$$
$$
\left. - 2uv\cos(\varphi_\alpha - \zeta)\left[2I\left(\frac{b}{|\Delta_\alpha|}\right) + I\left(\frac{-b_0}{|\Delta_\alpha|}\right) - I\left(\frac{-a_0}{|\Delta_\alpha|}\right)\right] \right\} - 2uv|\gamma|.
$$
$$(4.21b)$$

These two equations are decoupled since no self-consistency is imposed on E_σ. Since $b_0 = E_+^0 - E_\sigma^0 > 0$, terms with $I(-b_0/|\Delta_\alpha|)$ do not diverge. But $a_0 = E_-^0 - E_\sigma^0$ is negative in the singlet region of the infinite gap limit, and, therefore, terms with $I(-a_0/|\Delta_\alpha|)$ may diverge (when $a_0 = -|\Delta_\alpha|$). Close to the level crossing of E_- and E_σ, however, the integral turns out to be well behaved for the cases considered here. Equation (4.21) may therefore be used to determine the phase diagram.

4.1   Phase diagrams and comparison with NRG

Using these perturbative energy corrections, we may update the infinite gap phase diagram shown in Fig. 3.2. To first order in S_{pert}, the phase transition between the doublet and singlet state occurs when $E_- = E_\sigma$, equivalent to $a = 0$. The easiest approach to find the phase transition is simply to set $a = 0$ on the RHS of Eq. (4.21a) and $\delta a = -a_0$ on the LHS. This leaves us with the self-consistency equation

$$
\begin{aligned}
a_0 = \frac{2}{\pi} \sum_\alpha \Gamma_\alpha \Bigg\{ & \frac{b_0}{|\Delta_\alpha|} I\left(\frac{-b_0}{|\Delta_\alpha|}\right) + \frac{a_0}{|\Delta_\alpha|} I\left(\frac{-a_0}{|\Delta_\alpha|}\right) \\
& + 2uv\cos(\varphi_\alpha - \zeta)\left[2I(0) - I\left(\frac{-b_0}{|\Delta_\alpha|}\right) + I\left(\frac{-a_0}{|\Delta_\alpha|}\right)\right]\Bigg\} - 2uv|\gamma|,
\end{aligned}
\tag{4.22}
$$

which indirectly determines the phase transition.

For identical leads ($D_\alpha = D$, $|\Delta_\alpha| = |\Delta|$) with no phase differences, $\varphi_\alpha = 0$, we find the same phase diagram as Meng & Florens & Simon [15] computed for $N = 2$ leads. This is shown in Fig. 4.2. As the superconducting gap is decreased from the infinite gap limit, the doublet phase is suppressed. Close to the particle-hole symmetric point $\xi_d = 0$, however, the QD will still be found in the doublet phase for strong enough Coulomb repulsion. Note that the ratios $|\Delta|/\Gamma$ and D/Γ are 'extensive' quantities that depend on the number of leads N since $\Gamma = \sum_\alpha \Gamma_\alpha$ is the *total* hybridization. Hence, adding more leads favors the singlet phase. This was also true in the infinite gap limit (Fig. 3.2). Note, also, that we did not have to specify the individual couplings, only the total tunneling rate $\Gamma = \sum_\alpha \Gamma_\alpha$ since the leads act in unison when $\varphi_\alpha = 0$.

As previously mentioned, $I(-a_0/|\Delta|)$ diverges when $a_0 = -|\Delta|$. Except at the charge degeneracy points, the line on which $a_0 = -|\Delta|$ is far from the phase transition for all three values of $|\Delta|/\Gamma$ considered here (see Fig. 4.2). Since the curve $a_0 = -|\Delta|$ is in the singlet region in the infinite gap limit and the phase transition moves downwards in Fig. 4.2 with decreasing gap, the curve $a_0 = -|\Delta|$ will remain in the singlet region. Thus, the divergence will never be an issue for the determination of the phase transition and an imposed self-consistency on the renormalization of E_σ will only change the results slightly. In the limit $|\Delta| \to 0$, the curve $a_0 = -|\Delta|$ collapses onto the infinite gap phase transition curve.

For $|\Delta| \gtrsim \Gamma$, Meng & Florens & Simon found good agreement with numerical renormalization group (NRG) results by Bauer *et al.* [16] (also shown in Fig. 4.2 but graphically read off from Fig. 12 in Ref. [16]). For $|\Delta| < \Gamma$ and close to the particle-hole symmetric point,
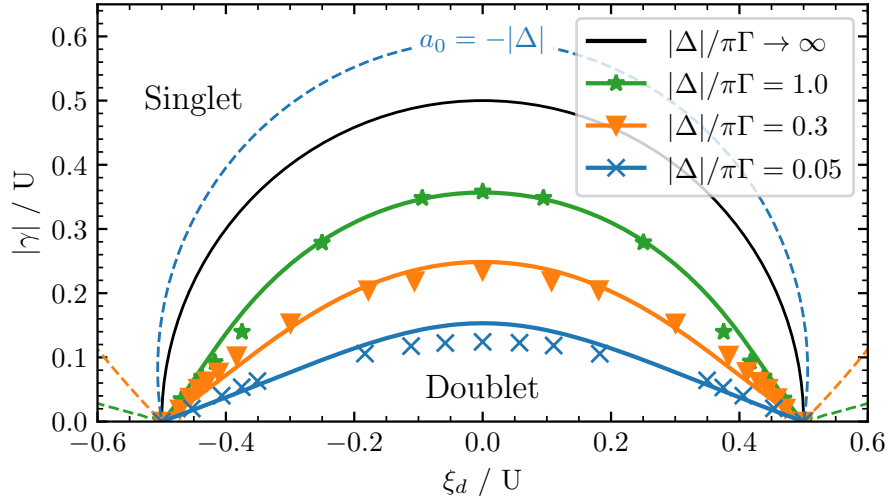
Figure 4.2: QD phase diagram to first order in S_{pert} for N identical leads with no phase differences $\varphi_\alpha = 0$, electronic bandwidth $D_\alpha = 5\pi\Gamma$, and superconducting gap $|\Delta_\alpha| = |\Delta|$ given by the legend. Solid curves are the analytical expressions ($\xi_d^2 + |\gamma|^2 = U^2/4$ for infinite gap and Eq. (4.22) for finite gap); symbols are NRG data (graphically read off) from Bauer *et al.* [16]; dashed curves (color matches solid curves) are where $a_0 = -|\Delta|$, giving diverging integrals. The doublet phase is stabilized with increasing gap around the particle-hole symmetric point $\xi_d = 0$. To read this diagram, it is easiest to think of fixing Γ, and thereby $|\gamma|$, for each line and varying U along the vertical axis and ξ_d along the horizontal axis.

the Kondo effect becomes increasingly important since U/Γ becomes large (local moment regime) at the phase transition. Then, the YSR singlet changes character from a BCS-like singlet ($T_K \ll \Delta$) – the $|-\rangle$ state we saw in Eq. (3.6) – to a Kondo singlet ($T_K \gg \Delta$) with a screened impurity moment. Meng & Florens & Simon argue that this first order perturbation theory underestimates the Kondo temperature at particle-hole symmetry. In this sense, perturbation theory breaks down since the system is very different from the infinite gap limit; the continuum states which were 'frozen' out and irrelevant in the infinite gap limit become important in Kondo physics. Non-negligible corrections lie in higher order perturbative terms. One could return to Eq. (4.4) and include these terms but it becomes a tedious process. Instead, a Schrieffer-Wolff [9, 17] transformation to an effective Kondo model in the local moment regime is likely a better approach. This eliminates (real) charge fluctuations on the QD and considers – as lowest order – co-tunneling processes.

Superconductivity and the Kondo effect are competing phenomena in the sense that Cooper pairs, that carry no net spin, must be broken apart to screen an impurity moment. In some parameter regimes, superconductivity prevails and in others, the Kondo effect. Consider, for instance, the particle-hole symmetric point $\xi_d = 0$, deep in the local moment regime of the Anderson model, $U \gg \Gamma$. For a single lead with very small superconducting gap $\Delta \ll T_K$ (the Kondo temperature is stated in Eq. (1.10)), there are lead electrons close to the Fermi level and it is energetically favorable for the electrons to screen the local moment instead of forming Cooper pairs. Therefore, we expect to find a screened Kondo singlet as the ground state of the system (see Section 1.4.1). As Δ is increased, we expect to find a crossover between the energy of the singlet and doublet states when it is favorable for the lead electrons to condense into Cooper pairs instead of participating in screening ($\Delta \sim T_K$). NRG calculations [16, 18, 19] have shown that the doublet-singlet transition is given by $T_K \simeq 0.3\Delta$ in the local moment regime when the QD is coupled to a single BCS superconductor.

To study the effect of a phase difference between leads, we consider a two-lead S-QD-S system with identical leads $D_\alpha = D, |\Delta_\alpha| = |\Delta|$, symmetric coupling $\Gamma_\alpha = \Gamma/2$ and phase bias φ. Using the same gap sizes as in Fig. 4.2, we find the phase diagrams shown in Fig. 4.3. The phase diagrams have a 'chimney'-like look with a growing doublet region around the particle-hole symmetric point as $\varphi \to \pi$; this is suppression of the proximity effect. As we saw in Fig. 4.2, the superconducting gap protects the doublet phase, causing the doublet region to shrink with decreasing gap. The sides of the chimney move from
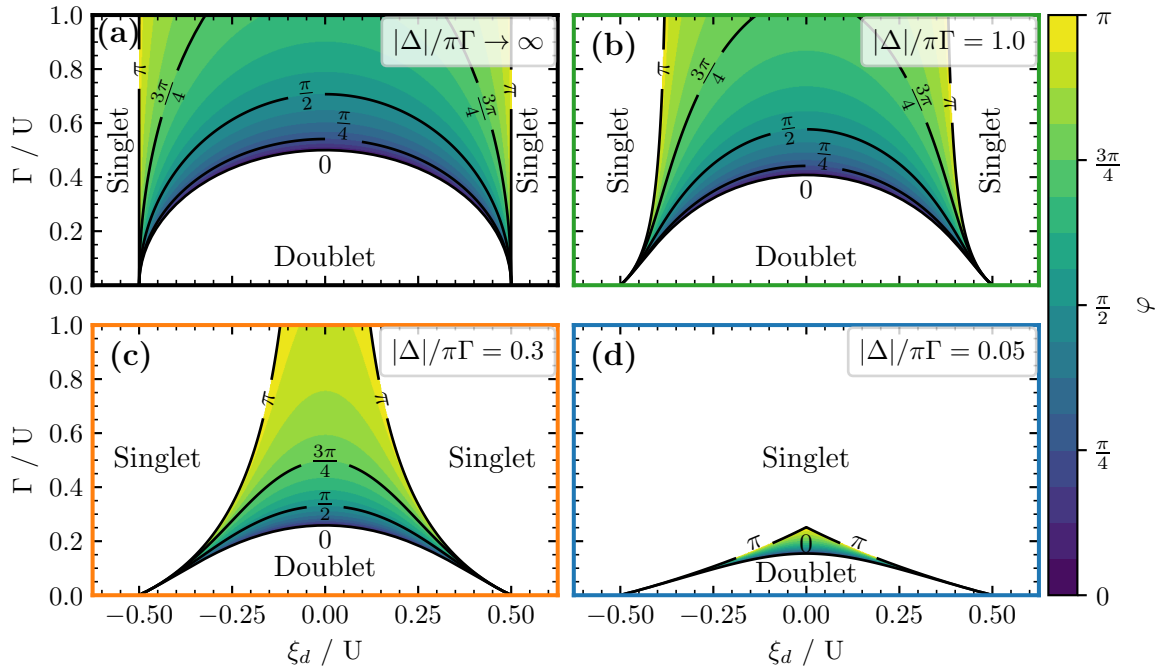
Figure 4.3: QD phase diagrams to first order in S_{pert} when coupled to $N = 2$ identical leads with electronic bandwidth $D_\alpha = 5\pi\Gamma$, phase difference φ, and superconducting gap $|\Delta_\alpha| = |\Delta|$ given by the figure text in the upper right corner. The frame color matches the line color used in Fig. 4.2. The color indicates where the phase transition lies for different phase differences; some lines have been labeled.

completely vertical in Fig. 4.3(a) to almost collapsed in Fig. 4.3(d) where the $\varphi = 0$ and $\varphi = \pi$ phase transitions lie almost atop each other. In the infinite gap limit (Fig. 4.3(a)) at $\varphi = \pi$, $\gamma = 0$ and the even parity base kets $|0\rangle$ and $|\uparrow\downarrow\rangle$ decouple. The system is then equivalent to the atomic limit of the Anderson model with no QD-lead hybridization (see Section 1.4). Thus, the ground state is seen to be the singlet $|\uparrow\downarrow\rangle$ when $\xi_d < -U/2$, the doublet $|\sigma\rangle$ when $-U/2 < \xi_d < U/2$ and the singlet $|0\rangle$ when $\xi_d > U/2$.

When $\varphi = \pi$, the off-diagonal anomalous terms in the self-energy (Eq. (2.14)) are zero and the proximity effect is completely cancelled. This is true in general for identical leads with symmetric coupling – even before we apply any perturbative methods. We can interpret this as destructive interference between the two leads. An instructive picture might be a field that changes sign across the QD, giving rise to a node in the superconducting gap at the QD. Since the unperturbed infinite gap limit only considers these off-diagonal terms, we expect the perturbative results to become gradually worse as we change φ from

zero to π where the diagonal terms become important. To quantify this claim, we compare our phase diagrams with NRG results by Tanaka *et al.* [20] who studied both the effect of asymmetric coupling and phase bias in two-terminal junctions ($L =$ Left lead, $R =$ Right lead) coupled to a QD. They considered identical leads with superconducting gap $|\Delta_L| = |\Delta_R| = \Delta$ and electronic bandwidth $D_L = D_R = 1.0 \times 10^5 \Delta$. Fig. 4.4 shows how our first-order results compare with data from their Figs. 5, 6, and 7; the NRG data has been extracted graphically. Note that all energies are in units of Δ instead of U as in the previous figures. The phase transition agreement is excellent in the proximitized limit $\varphi = 0$, $\Delta \gg \Gamma_R$ for both the symmetric ($\Gamma_L = \Gamma_R$) and asymmetric ($\Gamma_L = 1.44\Gamma_R$) coupling.

The NRG data in Fig. 4.4 show an enlarged doublet region when the phase difference is nonzero. This effect is captured by the perturbation theory, but it is too conservative. In the proximity-cancelled limit $\varphi = \pi$, $\Gamma_L \sim \Gamma_R$, the computed phase transitions are far off, as expected. The discrepancies are largest at particle-hole symmetry which is shown in Fig. 4.4(a). Here, the NRG calculations show a doublet ground state for all $\Gamma_R > 0, U > 0$ in the case of symmetric coupling at $\varphi = \pi$. Our perturbative results, however, predict a phase transition (dashed red line) in the middle of Fig. 4.4(a) for finite U. For asymmetric coupling at $\varphi = \pi$ (solid red lines), we actually have two phase transitions in the plotted region in Fig. 4.4(a) – in disagreement with NRG. Returning to Fig. 4.3(d), we see that the 'chimney'-collapse is a flaw of our perturbative results; the doublet phase should remain protected at particle-hole symmetry when the proximity-induced gap vanishes at $\varphi = \pi$ for symmetric coupling as is clearly evident from the NRG data in Fig. 4.4(c).

Recently, exactly this sort of 'chimney'-like phase diagram was observed experimentally by Bargerbos *et al.* [7] in the phase-biased junction seen in Fig. 1.1. They also used a two-lead superconducting Anderson model as the theoretical model but used NRG to fit to the experimental data which yielded good agreement.

We have seen that the MFS model accurate replicates the NRG phase diagram for single and two-lead systems with $\Delta \gtrsim \Gamma$. For smaller gaps ($\Delta < \Gamma$) or with a large phase bias $\varphi \simeq \pi$, however, care must be taken since the MFS model becomes gradually worse. This suggests that the important parameter for the validity of MFS is the induced gap on the QD γ (Eq. (3.2)).
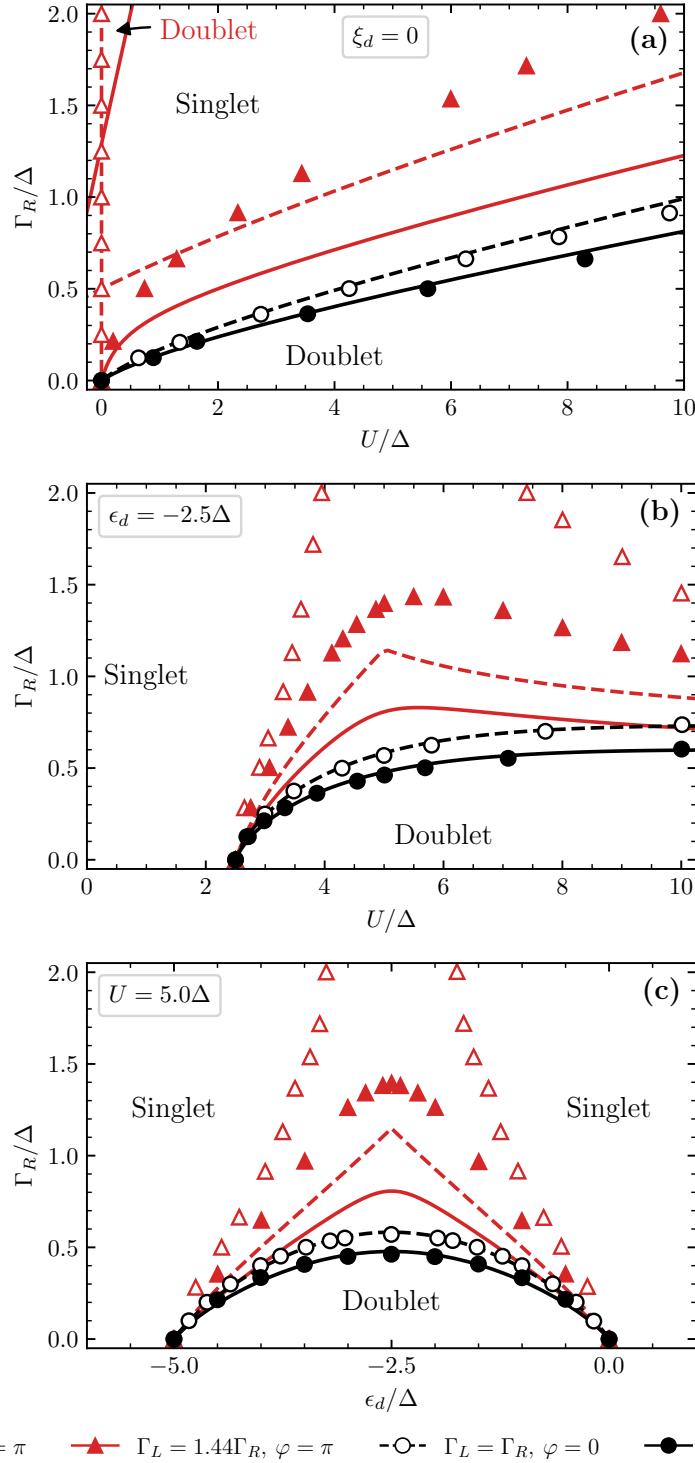
Figure 4.4: QD phase diagrams to first order in S_{pert} when coupled to $N = 2$ identical leads (L = Left lead, R = Right lead) with superconducting gap $|\Delta_L| = |\Delta_R| = \Delta$ and electronic bandwidth $D_L = D_R = 1.0 \times 10^5 \Delta$. The phase difference and couplings for the different lines is given by the legend below pane (c). Symbols are NRG data from Tanaka *et al.* [20] (the data has been graphically read off from their Figs. 5, 6, and 7).

5   Zero-bandwidth approximation

So far we have studied the infinite gap limit and the first order corrections to the energy levels and the accompanied phase diagram. In this section, we strengthen our intuition for Josephson junctions coupled to interacting quantum dots by considering a very simple numerical model, namely the zero-bandwidth (ZBW) approximation. In the ZBW model, BCS leads are replaced by single quasiparticles with energy Δ, disregarding the continuum of states outside the gap. This makes the model exactly solvable, numerically. Opposed to NRG, the ZBW model is also easily extendible to more complex systems with more dots, leads, and other couplings. Despite the crude continuum simplification, it has been shown to be a useful tool to describe experimental data, in good agreement with NRG [21, 22].

One caveat of the model is the determination of the effective tunneling between the QD and the single level in the lead. Given the hybridization Γ which describes total coupling to all states in the lead, the conversion to the ZBW tunneling parameter is non-trivial. In some sense, one can treat it as a fitting parameter when comparing with experimental data. It turns out, however, that the conversion is straightforward in the infinite gap limit as we will present in Section 5.6.1.

The ZBW model is also able to interpolate between two distinct regimes: the proximity-induced superconducting QD ($U \ll \Delta$) and YSR screening of a local moment ($U \gtrsim \Delta$) [17, 23]. Nonetheless, the model fails to describe the Kondo effect in the strongly interacting limit $U \gg \Delta$ due to the lack of a continuum of bulk states. In Section 5.6.2 we try to mend this flaw in the S-QD ($N = 1$) system by a suitable rescaling of the tunneling parameter.

First, we introduce the ZBW Hamiltonian and write it in a basis of Fock states before we transform it into a basis that conserves total spin angular momentum. Afterwards, we study screening of a local moment in the ZBW model and YSR bound states before we move on to energy dispersions and current-phase relations. In the end, we try to relate it directly to the superconducting Anderson model and compare with both NRG and the MFS model from Section 4.

5.1   The ZBW Hamiltonian

The ZBW approximation amounts to keeping only terms involving Fermi surface states in the Hamiltonian which substantially simplifies the problem. The Hamiltonian $H =$

$H_S + H_D + H_{S-D}$ (Eqs. (2.1) to (2.3)) is then approximated by

$$H_S \approx -\sum_\alpha \left(\Delta_\alpha c_{\alpha\uparrow}^\dagger c_{\alpha\downarrow}^\dagger + \Delta_\alpha^* c_{\alpha\downarrow} c_{\alpha\uparrow} \right), \tag{5.1a}$$

$$H_D = \sum_\sigma \epsilon_d n_{d\sigma} + U n_{d\uparrow} n_{d\downarrow}, \tag{5.1b}$$

$$H_{S-D} \approx \sum_{\alpha\sigma} \left(t_\alpha c_{\alpha\sigma}^\dagger d_\sigma + t_\alpha d_\sigma^\dagger c_{\alpha\sigma} \right), \tag{5.1c}$$

where we have dropped the k-index on the c-operators $c_{\alpha\sigma}^{(\dagger)} = c_{\alpha k_F\sigma}^{(\dagger)}$ and chosen a gauge with real tunneling matrix elements $t_\alpha \in \mathbb{R}$. The QD part of the Hamiltonian remains unchanged.

In the ZBW approximation we are left with a Hilbert space of size 4^{N+1} (4 states in each lead and 4 on the QD), meaning we can diagonalize the Hamiltonian numerically if N is reasonably small. Let us denote the Fock states by

$$|D, S_1, S_2, ..., S_N\rangle = D^\dagger S_1^\dagger S_2^\dagger \cdots S_N^\dagger |0\rangle, \tag{5.2}$$

where the creation operators $D^\dagger$ and $S_\alpha^\dagger$ mean

$$D^\dagger = \begin{cases} \mathbb{1} & (n_D = 0) \\ d_\sigma^\dagger, \quad \sigma = \uparrow, \downarrow & (n_D = 1) \\ d_\uparrow^\dagger d_\downarrow^\dagger & (n_D = 2) \end{cases}, \qquad S_\alpha^\dagger = \begin{cases} \mathbb{1} & (n_\alpha = 0) \\ c_{\alpha\sigma}^\dagger, \quad \sigma = \uparrow, \downarrow & (n_\alpha = 1) \\ c_{\alpha\uparrow}^\dagger c_{\alpha\downarrow}^\dagger & (n_\alpha = 2) \end{cases}. \tag{5.3}$$

The number n simply counts the number of creation operators (electrons) and will become useful to keep track of minus signs when commuting operators. Single electron operators anti-commute between a lead and the QD and between different leads: $c_{\alpha\sigma}^{(\dagger)} d_\sigma^{(\dagger)} = -d_\sigma^{(\dagger)} c_{\alpha\sigma}^{(\dagger)}$, $c_{\alpha\sigma}^{(\dagger)} c_{\alpha'\sigma}^{(\dagger)} = -c_{\alpha'\sigma}^{(\dagger)} c_{\alpha\sigma}^{(\dagger)}$ ($\alpha \neq \alpha'$). Thus,

$$S_\alpha^{(\dagger)} S_{\alpha'}^{(\dagger)} = (-1)^{n_\alpha n_{\alpha'}} S_{\alpha'}^{(\dagger)} S_\alpha^{(\dagger)}, \quad \alpha \neq \alpha', \tag{5.4a}$$

$$S_\alpha^{(\dagger)} D^{(\dagger)} = (-1)^{n_\alpha n_D} D^{(\dagger)} S_\alpha^{(\dagger)}. \tag{5.4b}$$

The states are orthonormal, meaning

$$\langle \tilde{D}, \tilde{S}_1, ..., \tilde{S}_N | D, S_1, ..., S_N \rangle = \langle 0 | \tilde{S}_N \cdots \tilde{S}_1 \tilde{D} D^\dagger S_1^\dagger \cdots S_N^\dagger | 0 \rangle = \delta_{\tilde{D}D} \prod_\alpha \delta_{\tilde{\alpha}\alpha}. \tag{5.5}$$

Before we can diagonalize the Hamiltonian, we need to determine the matrix elements in this Fock basis. The QD part is diagonal.

$$\langle \tilde{D}, \tilde{S}_1, ..., \tilde{S}_N | H_D | D, S_1, ..., S_N \rangle = E_D \delta_{\tilde{D}D} \prod_\alpha \delta_{\tilde{\alpha}\alpha}, \tag{5.6}$$

where $E_D = 0, \epsilon_d, 2\epsilon_d + U$ for the states $|0, S_1, ..., S_N\rangle, |\sigma, S_1, ..., S_N\rangle, |\uparrow\downarrow, S_1, ..., S_N\rangle$, respectively. The lead part H_S also simplifies nicely since it only concerns electrons in the *same* lead. Let us write $H_S = \sum_\alpha H_S^\alpha$, where $H_S^\alpha = -\Delta_\alpha c_{\alpha\uparrow}^\dagger c_{\alpha\downarrow}^\dagger - \Delta_\alpha^* c_{\alpha\downarrow} c_{\alpha\uparrow}$ from Eq. (5.1a). Note that operators pertaining to different leads or the QD commute with H_S^α since it is bilinear. Using Eqs. (5.4) and (5.5), we find

$$
\begin{aligned}
\langle \tilde{D}, \tilde{S}_1, ..., \tilde{S}_N | H_S | D, S_1, ..., S_N \rangle &= \sum_\alpha \langle 0 | \tilde{S}_N \cdots \tilde{S}_1 \tilde{D} H_S^\alpha D^\dagger S_1^\dagger \cdots S_N^\dagger | 0 \rangle \\
&= \delta_{\tilde{D}D} \sum_\alpha \langle 0 | \tilde{S}_N \cdots \tilde{S}_\alpha H_S^\alpha S_\alpha^\dagger \cdots S_N^\dagger | 0 \rangle \prod_{\alpha' < \alpha} \delta_{\tilde{\alpha}'\alpha'} \\
&= \delta_{\tilde{D}D} \sum_\alpha \langle 0 | \tilde{S}_\alpha H_S^\alpha S_\alpha^\dagger | 0 \rangle \prod_{\alpha'' > \alpha} (-1)^{(\tilde{n}_\alpha + n_\alpha)n_{\alpha''}} \prod_{\alpha' \neq \alpha} \delta_{\tilde{\alpha}'\alpha'} \\
&= \delta_{\tilde{D}D} \sum_\alpha \langle 0 | \tilde{S}_\alpha H_S^\alpha S_\alpha^\dagger | 0 \rangle \prod_{\alpha' \neq \alpha} \delta_{\tilde{\alpha}'\alpha'},
\end{aligned}
$$

$$(5.7)$$

where we have used that $\tilde{n}_\alpha + n_\alpha = 2$ when $\langle 0 | \tilde{S}_\alpha H_S^\alpha S_\alpha^\dagger | 0 \rangle \neq 0$; the BCS terms create or destroy a Cooper pair of two electrons. We represent H_S^α in the single lead subspace as a 4×4 matrix. In the basis $\{|0_\alpha\rangle, |\uparrow_\alpha\rangle, |\downarrow_\alpha\rangle, |\uparrow\downarrow_\alpha\rangle\}$, the matrix representation is

$$
H_S^\alpha \doteq \begin{pmatrix} 0 & 0 & 0 & -\Delta_\alpha^* \\ 0 & 0 & 0 & 0 \\ 0 & 0 & 0 & 0 \\ -\Delta_\alpha & 0 & 0 & 0 \end{pmatrix}.
$$

$$(5.8)$$

The tunneling part H_{S-D} couples each lead to the QD and, hence, takes a more complicated form. Similar to before, we write Eq. (5.1c) as $H_{S-D} = \sum_\alpha H_{S-D}^\alpha$, where

$H_{S-D}^{\alpha} = \sum_{\sigma}(t_{\alpha}c_{\alpha\sigma}^{\dagger}d_{\sigma} + t_{\alpha}^{*}d_{\sigma}^{\dagger}c_{\alpha\sigma})$, such that

$$\begin{aligned}
\langle\tilde{D},\tilde{S}_1,...,\tilde{S}_N|H_{S-D}|D,S_1,...,S_N\rangle &= \sum_{\alpha}\langle 0|\tilde{S}_N\cdots\tilde{S}_1\tilde{D}H_{S-D}^{\alpha}D^{\dagger}S_1^{\dagger}\cdots S_N^{\dagger}|0\rangle \\
&= \sum_{\alpha}\langle 0|\tilde{S}_N\cdots\tilde{S}_{\alpha}\tilde{D}H_{S-D}^{\alpha}D^{\dagger}S_{\alpha}^{\dagger}\cdots S_N^{\dagger}|0\rangle \\
&\qquad\qquad\qquad\times\prod_{\alpha'<\alpha}(-1)^{(\tilde{n}_D+n_D)n_{\alpha'}}\delta_{\tilde{\alpha}'\alpha'} \\
&= \sum_{\alpha}\langle 0|\tilde{S}_{\alpha}\tilde{D}H_{S-D}^{\alpha}D^{\dagger}S_{\alpha}^{\dagger}|0\rangle\prod_{\alpha'<\alpha}(-1)^{n_{\alpha'}}\delta_{\tilde{\alpha}'\alpha'} \\
&\qquad\qquad\times\prod_{\alpha''>\alpha}(-1)^{(\tilde{n}_{\alpha}+\tilde{n}_D+n_D+n_{\alpha})n_{\alpha}''}\delta_{\tilde{\alpha}''\alpha''} \\
&= \sum_{\alpha}\langle 0|\tilde{S}_{\alpha}\tilde{D}H_{S-D}^{\alpha}D^{\dagger}S_{\alpha}^{\dagger}|0\rangle\,(-1)^{\sum_{\alpha'<\alpha}n_{\alpha'}}\prod_{\alpha'\neq\alpha}\delta_{\tilde{\alpha}'\alpha'}.
\end{aligned}$$
(5.9)

In the third and final equalities we used that $\tilde{n}_D = n_D \pm 1$ (one electron is either added to or removed from the QD) and $\tilde{n}_D + \tilde{n}_{\alpha} = n_D + n_{\alpha}$ (the number of electrons is conserved) when $\langle 0|\tilde{S}_{\alpha}\tilde{D}H_T^{\alpha\sigma}D^{\dagger}S_{\alpha}^{\dagger}|0\rangle \neq 0$. As in Eq. (5.8), we can write the matrix representation of H_{S-D}^{α} in a subspace of the full 4^{N+1}-dimensional Hilbert space. Since H_{S-D}^{α} couples a single lead and the QD, we need a 16×16 matrix to represent this term. Due to the size, we omit the explicit form and simply note that it is a sparse matrix with only 16 nonzero entries.

5.2   Conservation of total spin angular momentum

The ZBW Hamiltonian has spin rotational symmetry which we will exploit. In this section we will show that the total spin is conserved, simplifying the job of diagonalizing the Hamiltonian.

The spin of the QD and of lead α are measured with the operators $\boldsymbol{S}_{\text{QD}}$ and $\boldsymbol{S}_{\alpha}$, respectively. The usual commutation relations between different directions apply and the square of spin operator commutes with any of its three components.

$$[S_i, S_j] = i\epsilon_{ijk}S_k, \quad i,j,k \in \{x,y,z\}, \tag{5.10a}$$

$$[S^2, S_i] = 0, \quad i \in \{x,y,z\}. \tag{5.10b}$$

Here, ϵ_{ijk} is the Levi-Civita symbol and we set $\hbar = 1$. Thus, only one component of the spin and S^2 may be measured simultaneously. Note that operators pertaining to different

'channels' (QD or leads) commute, e.g. $\left[S_{\mathrm{QD}}^x, S_2^y\right] = 0$. The z-component of $\boldsymbol{S}_{\mathrm{QD}}$ and $\boldsymbol{S}_\alpha$ have the explicit forms

$$
\begin{aligned}
S_{\mathrm{QD}}^z &= \frac{1}{2}(n_{d\uparrow} - n_{d\downarrow}), \\
S_\alpha^z &= \frac{1}{2}(n_{\alpha\uparrow} - n_{\alpha\downarrow}).
\end{aligned}
\tag{5.11}
$$

Instead of working with S_x and S_y directly, we introduce the non-hermitian ladder operators: $S_\pm = S_x \pm iS_y$. They are easier to find explicit forms of than S_x and S_y and will be more useful to us.

$$
\begin{aligned}
S_{\mathrm{QD}}^+ &= d_\uparrow^\dagger d_\downarrow, \qquad S_{\mathrm{QD}}^- = d_\downarrow^\dagger d_\uparrow, \\
S_\alpha^+ &= c_{\alpha\uparrow}^\dagger c_{\alpha\downarrow}, \qquad S_\alpha^- = c_{\alpha\downarrow}^\dagger c_{\alpha\uparrow}.
\end{aligned}
\tag{5.12}
$$

From these expressions, it is straightforward to verify the commutation relations $[S_+, S_-] = 2S_z$ and $[S_z, S_\pm] = \pm S_\pm$. These are equivalent to Eq. (5.10a). Using the ladder operators, one may write $S^2 = S_x^2 + S_y^2 + S_z^2$ as

$$
\begin{aligned}
S_{\mathrm{QD}}^2 &= \frac{1}{2}\left(S_{\mathrm{QD}}^+ S_{\mathrm{QD}}^- + S_{\mathrm{QD}}^- S_{\mathrm{QD}}^+\right) + \left(S_{\mathrm{QD}}^z\right)^2 = \frac{3}{4}n_d - \frac{3}{2}n_{d\uparrow}n_{d\downarrow}, \\
S_\alpha^2 &= \frac{1}{2}\left(S_\alpha^+ S_\alpha^- + S_\alpha^- S_\alpha^+\right) + (S_\alpha^z)^2 = \frac{3}{4}n_\alpha - \frac{3}{2}n_{\alpha\uparrow}n_{\alpha\downarrow}.
\end{aligned}
\tag{5.13}
$$

The (single-channel) operators have the following properties:

$$
\begin{aligned}
S_z \left|0\right\rangle &= S_z \left|\uparrow\downarrow\right\rangle = 0, \\
S_z \left|\uparrow\right\rangle &= \frac{1}{2}\left|\uparrow\right\rangle, \quad S_z \left|\downarrow\right\rangle = -\frac{1}{2}\left|\downarrow\right\rangle,
\end{aligned}
\tag{5.14}
$$

$$
\begin{aligned}
S_\pm \left|0\right\rangle &= S_\pm \left|\uparrow\downarrow\right\rangle = 0, \\
S_+ \left|\downarrow\right\rangle &= \left|\uparrow\right\rangle, \quad S_+ \left|\uparrow\right\rangle = 0, \\
S_- \left|\uparrow\right\rangle &= \left|\downarrow\right\rangle, \quad S_- \left|\downarrow\right\rangle = 0,
\end{aligned}
\tag{5.15}
$$

$$
\begin{aligned}
S^2 \left|0\right\rangle &= S^2 \left|\uparrow\downarrow\right\rangle = 0, \\
S^2 \left|\sigma\right\rangle &= \frac{3}{4}\left|\sigma\right\rangle.
\end{aligned}
\tag{5.16}
$$

Due to the tunneling part of the Hamiltonian H_{S-D}, only the *total* spin across the QD and the leads will be conserved. Let us construct the operator that measures the total spin

of a Fock state.

$$
\begin{aligned}
\boldsymbol{S} &= \boldsymbol{S}_{\mathrm{QD}} + \boldsymbol{S}_1 + ... + \boldsymbol{S}_N \\
&= \boldsymbol{S}_{\mathrm{QD}} \otimes \mathbb{1}_1 \otimes \cdots \otimes \mathbb{1}_N + \mathbb{1}_{\mathrm{QD}} \otimes \boldsymbol{S}_1 \otimes \mathbb{1}_2 \otimes \cdots \otimes \mathbb{1}_N + ... + \mathbb{1}_{\mathrm{QD}} \otimes \cdots \otimes \mathbb{1}_{N-1} \otimes \boldsymbol{S}_N.
\end{aligned}
\tag{5.17}
$$

The operators on the RHS only act in their respective 'channel', i.e. the QD or lead α. Since all single-channel operators on the RHS satisfy Eq. (5.10) and commute across channels, the total spin $\boldsymbol{S}$ also satisfies Eq. (5.10). The z-component of $\boldsymbol{S}$ has the explicit form

$$
S_z = S_{\mathrm{QD}}^z + S_1^z + ... + S_N^z = \frac{1}{2}(n_{d\uparrow} - n_{d\downarrow}) + \frac{1}{2}(n_{1\uparrow} - n_{1\downarrow}) + ... + \frac{1}{2}(n_{N\uparrow} - n_{N\downarrow}), \tag{5.18}
$$

and the ladder operators extend to

$$
\begin{aligned}
S_+ &= S_{\mathrm{QD}}^+ + S_1^+ + ... + S_N^+ = d_\uparrow^\dagger d_\downarrow + c_{1\uparrow}^\dagger c_{1\downarrow} + ... + c_{N\uparrow}^\dagger c_{N\downarrow}, \\
S_- &= S_{\mathrm{QD}}^- + S_1^- + ... + S_N^- = d_\downarrow^\dagger d_\uparrow + c_{1\downarrow}^\dagger c_{1\uparrow} + ... + c_{N\downarrow}^\dagger c_{N\uparrow}.
\end{aligned}
\tag{5.19}
$$

Expanding S^2, we have

$$
S^2 = S_{\mathrm{QD}}^2 + \sum_\alpha S_\alpha^2 + 2\sum_\alpha \boldsymbol{S}_{\mathrm{QD}} \cdot \boldsymbol{S}_\alpha + 2\sum_\alpha \sum_{\alpha' > \alpha} \boldsymbol{S}_\alpha \cdot \boldsymbol{S}_{\alpha'} \tag{5.20}
$$

The combined spin operators S_z, S^2 and $S_\pm$ satisfy the same commutation relations as the single channel ones: $\left[S_z, S^2\right] = \left[S_\pm, S^2\right] = 0$, $[S_+, S_-] = 2S_z$, $[S_z, S_\pm] = \pm S_\pm$. Note, however, that $\left[S^2, S_{\mathrm{QD}}^z\right] \neq 0 \neq \left[S^2, S_\alpha^z\right]$; one can only describe the system using the single-channel operators $(S_{\mathrm{QD}}^z, S_\alpha^z)$ *or* the total spin operators (S^2, S_z).

Now we show that the ZBW Hamiltonian (Eq. (5.1)) commutes with both S_z and S^2, such that they correspond to conserved quantities and 'good' quantum numbers. It is clear that 'cross-channel' commutators are zero.

$$
[H_D, \boldsymbol{S}_\alpha] = \left[H_D, S_\alpha^2\right] = 0, \tag{5.21a}
$$

$$
\begin{aligned}
&[H_S, \boldsymbol{S}_{\mathrm{QD}}] = \left[H_S, S_{\mathrm{QD}}^2\right] = 0, \\
&[H_S^\alpha, \boldsymbol{S}_{\alpha'}] = \left[H_S^\alpha, S_{\alpha'}^2\right] = 0, \quad \alpha' \neq \alpha,
\end{aligned}
\tag{5.21b}
$$

$$
\left[H_{S-D}^\alpha, \boldsymbol{S}_{\alpha'}\right] = \left[H_{S-D}^\alpha, S_{\alpha'}^2\right] = 0, \quad \alpha' \neq \alpha. \tag{5.21c}
$$

Let us first show that $[H, S_z] = 0$. Using Eqs. (5.18) and (5.21), we find

$$[H, S_z] = \left[H_D, S_{\text{QD}}^z\right] + \sum_\alpha [H_S^\alpha, S_\alpha^z] + \sum_\alpha \left[H_{S-D}^\alpha, S_{\text{QD}}^z + S_\alpha^z\right]. \tag{5.22}$$

Since $[n_{d\sigma}, n_{d\sigma'}] = 0$, the first term is zero: $\left[H_D, S_{\text{QD}}^z\right] = 0$. The second term is also zero and the QD and lead contributions cancel in the final term.

$$[H_S^\alpha, S_\alpha^z] = -\frac{1}{2}\left(-\Delta_\alpha c_{\alpha\uparrow}^\dagger c_{\alpha\downarrow}^\dagger + \Delta^* c_{\alpha\downarrow} c_{\alpha\uparrow} - \Delta_\alpha c_{\alpha\downarrow}^\dagger c_{\alpha\uparrow}^\dagger + \Delta^* c_{\alpha\uparrow} c_{\alpha\downarrow}\right) = 0, \tag{5.23}$$

$$\left[H_{S-D}^\alpha, S_{\text{QD}}^z\right] = \frac{t_\alpha}{2}\left(c_{\alpha\uparrow}^\dagger d_\uparrow - d_\uparrow^\dagger c_{\alpha\uparrow} - c_{\alpha\downarrow}^\dagger d_\downarrow + d_\downarrow^\dagger c_{\alpha\downarrow}\right) = -\left[H_{S-D}^\alpha, S_\alpha^z\right]. \tag{5.24}$$

Thus, we conclude $[H, S_z] = 0$.

Next, let us show $\left[H, S^2\right] = 0$. Using Eqs. (5.20) and (5.21), we find

$$\left[H_D, S^2\right] = \left[H_D, S_{\text{QD}}^2\right] + 2[H_D, \boldsymbol{S}_{\text{QD}}] \cdot \sum_\alpha \boldsymbol{S}_\alpha, \tag{5.25}$$

$$\left[H_S, S^2\right] = 2\boldsymbol{S}_{\text{QD}} \cdot \sum_\alpha [H_S^\alpha, \boldsymbol{S}_\alpha] + \sum_{\alpha\alpha'}\left([H_S^\alpha, \boldsymbol{S}_\alpha] \cdot \boldsymbol{S}_{\alpha'} + \boldsymbol{S}_\alpha \cdot \left[H_S^{\alpha'}, \boldsymbol{S}_{\alpha'}\right]\right), \tag{5.26}$$

$$\left[H_{S-D}, S^2\right] = \sum_\alpha \left[H_{S-D}^\alpha, (\boldsymbol{S}_{\text{QD}} + \boldsymbol{S}_\alpha)^2\right] + 2\sum_{\alpha,\alpha'\neq\alpha}\left[H_{S-D}^\alpha, \boldsymbol{S}_{\text{QD}} + \boldsymbol{S}_\alpha\right] \cdot \boldsymbol{S}_{\alpha'}. \tag{5.27}$$

We use the ladder operators (Eq. (5.12)) to write $S_x = (S_+ + S_-)/2$, $S_y = (S_+ - S_-)/2i$. We find $\left[n_{d\sigma}, S_{\text{QD}}^\pm\right] = \pm\sigma S_{\text{QD}}^\pm$ such that $\left[H_D, S_{\text{QD}}^\pm\right] = 0$. Remembering that $\left[H_D, S_{\text{QD}}^z\right] = 0$, we conclude $[H_D, \boldsymbol{S}_{\text{QD}}] = 0$ and, hence, $\left[H_D, S^2\right] = 0$. It is easy to see that $[H_S^\alpha, S_\alpha^\pm] = 0$ such that also $[H_S^\alpha, \boldsymbol{S}_\alpha] = 0$ and, therefore, $\left[H_S, S^2\right] = 0$. This leaves us with the tunneling part for which we find

$$\left[H_{S-D}^\alpha, S_\alpha^+\right] = t_\alpha(d_\uparrow^\dagger c_{\alpha\downarrow} - c_{\alpha\uparrow}^\dagger d_\downarrow) = -\left[H_{S-D}^\alpha, S_{\text{QD}}^+\right], \tag{5.28}$$

$$\left[H_{S-D}^\alpha, S_\alpha^-\right] = -\left[H_{S-D}^\alpha, S_\alpha^+\right]^\dagger = -\left[H_{S-D}^\alpha, S_{\text{QD}}^-\right]. \tag{5.29}$$

The terms in Eq. (5.27) evaluate to zero since the QD and lead commutators cancel, i.e. $\left[H_{S-D}^\alpha, \boldsymbol{S}_{\text{QD}} + \boldsymbol{S}_\alpha\right] = 0$ (the z-component is zero from Eq. (5.24)). In conclusion, our ZBW Hamiltonian commutes with both S_z and S^2 which is a consequence of spin rotational symmetry.

We now have a set of three commuting operators (H, S_z, S^2) which we may use to label the eigenstates $|n, s, m\rangle$.

$$H\left|n, s, m\right\rangle = E_n^s\left|n, s, m\right\rangle, \tag{5.30}$$

$$S_z\left|n, s, m\right\rangle = m\left|n, s, m\right\rangle, \tag{5.31}$$

$$S^2\left|n, s, m\right\rangle = s(s+1)\left|n, s, m\right\rangle. \tag{5.32}$$

We may not add S_{QD}^2 or S_α^2 to the set of commuting operators (H, S_z, S^2) since they do not commute with H_{S-D}. Notice that the energy is independent of m. The degeneracy is due to spin rotational symmetry and may be broken by e.g. an external magnetic field. Combining the intermediate results in proving $\left[H, S^2\right] = 0$, we showed that $[H, S_\pm] = 0$. Thus, the states $|n, s, m\rangle$ and $S_\pm |n, s, m\rangle \propto |n, s, m \pm 1\rangle$ are degenerate.

$$H(S_\pm |n, s, m\rangle) = S_\pm(H |n, s, m\rangle) = E_n^s(S_\pm |n, s, m\rangle). \tag{5.33}$$

All states within the same multiplet are degenerate.

To find the energy spectrum of the ZBW Hamiltonian, then, one may use the eigenstates of S^2 and S_z to block-diagonalize H through a change of basis. Only states with the same quantum numbers s and m are connected via H. We wish to find a unitary operator U which maps the Fock states onto eigenstates of S^2 and S_z.

$$|\chi, s, m\rangle = U |D, S_1, S_2, ..., S_N\rangle. \tag{5.34}$$

The χ indicates that these states are not necessarily eigenstates of H, but some linear combination of eigenstates with the same s and m; it represents our ignorance.

$$|\chi, s, m\rangle = \sum_n \langle n, s, m | \chi, s, m\rangle |n, s, m\rangle. \tag{5.35}$$

Multiplying Eq. (5.34) from the left by the bra $\langle \tilde{D}, \tilde{S}_1, ..., \tilde{S}_N|$, we see that the matrix elements of U in the original basis are the appropriate Clebsch-Gordan coefficients.

$$\langle \tilde{D}, \tilde{S}_1, ..., \tilde{S}_N | U | D, S_1, S_2, ..., S_N\rangle = \langle \tilde{D}, \tilde{S}_1, ..., \tilde{S}_N | \chi, s, m\rangle. \tag{5.36}$$

Except for the largest multiplet $s = s_{\max} = (N + 1)/2$, this mapping is not unique. In other words, the expansion coefficients $\langle n, s, m | \chi, s, m\rangle$ in Eq. (5.35) are not unique. The set of states $\{|\chi, s, m\rangle\}$ is just one particular basis which block-diagonalizes H.

Conveniently, the Fock states are already eigenstates of S_z.

$$S_z |D, S_1, S_2, ..., S_N\rangle = m |D, S_1, S_2, ..., S_N\rangle. \tag{5.37}$$

The z-projection of the total spin is just the sum of individual contributions from all single-particle states: $m = m_{\text{QD}} + m_1 + m_2 + ... + m_N$. This follows from the linearity of S_z (Eq. (5.18)). If we consider

$$\begin{aligned} 0 &= \langle D, S_1, ..., S_N | S_z - S_{\text{QD}}^z - S_1^z - ... - S_N^z | \chi, s, m\rangle \\ &= (m - m_{\text{QD}} - m_1 - ... - m_N) \langle D, S_1, ..., S_N | \chi, s, m\rangle, \end{aligned} \tag{5.38}$$

then it follows that the Clebsch-Gordan coefficients vanish unless $m = m_{\mathrm{QD}} + m_1 + m_2 + \ldots + m_N$ such that the transformation matrix U only connect states with the same m as usual.

$$U = U_m \delta_{m, m_{\mathrm{QD}} + m_1 + \ldots + m_N}. \tag{5.39}$$

The eigenstates of S^2 are a little more cumbersome to obtain but largely follows the usual procedure of applying S_- from the highest weight state and ensuring orthogonality between different multiplets (different s). If we list all 4^{N+1} Fock states, it is easy to divide them into groups with the same quantum number m. We only need the states with $m \geq 0$ to find all energies E_n^s in the end. This results in $N + 2$ blocks – one for each spin z-projection $m = 0, 1/2, \ldots, (N+1)/2$. In each group there will be states from higher multiplets ($s \geq m$), except for the two groups with largest m: $m = s_{\max}, s_{\max} - 1/2$. We know that the highest weight state $|\uparrow, \uparrow, \ldots, \uparrow\rangle$ belongs to the largest multiplet as the only state with $m = s_{\max}$.

$$|s = s_{\max}, m = m_{\max}\rangle = |\uparrow, \uparrow, \ldots, \uparrow\rangle, \quad U_{m=(N+1)/2} = \mathbb{1}. \tag{5.40}$$

In the next group ($m = s_{\max} - 1/2$) which contains Fock states with N spin-up electrons and 1 empty or doubly occupied single-particle state, there are $2(N+1)$ Fock states. They all have the same quantum numbers s and m and, hence, any linear combination of these states are also simultaneous eigenstates of S^2 and S_z.

$$\begin{aligned}
S^2 |\uparrow, \ldots, \uparrow, 0, \uparrow, \ldots, \uparrow\rangle &= \frac{N}{2}\left(\frac{N}{2} + 1\right) |\uparrow, \ldots, \uparrow, 0, \uparrow, \ldots, \uparrow\rangle, \\
S^2 |\uparrow, \ldots, \uparrow, \uparrow\downarrow, \uparrow, \ldots, \uparrow\rangle &= \frac{N}{2}\left(\frac{N}{2} + 1\right) |\uparrow, \ldots, \uparrow, \uparrow\downarrow, \uparrow, \ldots, \uparrow\rangle.
\end{aligned} \tag{5.41}$$

As mentioned, this freedom means the mapping in Eq. (5.34) is not unique. We would need more 'good' quantum numbers / commuting operators / symmetries to choose a better basis. For simplicity, we take the basis of eigenstates of S^2 and S_z in the $s = m = N/2$-subspace to be the Fock states $|D, S_1, \ldots, S_N\rangle$. Then U_m is, again, just the identity.

$$U_{m=N/2} = \mathbb{1}. \tag{5.42}$$

From here, we apply S_- to the basis states to lower m.

$$\begin{aligned}
S_- |s_{\max}, s_{\max}\rangle &\propto |s_{\max}, s_{\max} - 1\rangle, \\
S_- |\chi, s_{\max} - 1/2, s_{\max} - 1/2\rangle &\propto |\chi, s_{\max} - 1/2, s_{\max} - 3/2\rangle.
\end{aligned} \tag{5.43}$$

Then we construct the states $|\chi, s_{\max} - 1, s_{\max} - 1\rangle$, $|\chi, s_{\max} - 3/2, s_{\max} - 3/2\rangle$ by ensuring they are orthogonal to the higher multiplets and within the same multiplet.

$$
\begin{aligned}
\langle s_{\max}, s_{\max} - 1 | \chi, s_{\max} - 1, s_{\max} - 1 \rangle &= 0, \\
\langle \chi, s_{\max} - 1, s_{\max} - 1 | \chi', s_{\max} - 1, s_{\max} - 1 \rangle &= \delta_{\chi,\chi'}, \\
\langle \chi, s_{\max} - 1/2, s_{\max} - 3/2 | \chi', s_{\max} - 3/2, s_{\max} - 3/2 \rangle &= 0, \\
\langle \chi, s_{\max} - 3/2, s_{\max} - 3/2 | \chi', s_{\max} - 3/2, s_{\max} - 3/2 \rangle &= \delta_{\chi,\chi'}.
\end{aligned}
\tag{5.44}
$$

This may be done using the Gram–Schmidt process, for instance. Again, the basis is not unique. We continue using S_- and forming an orthonormal basis for each m until we reach $m = 0$ and $m = 1/2$. The Clebsch-Gordan coefficients for $m < 0$ may be inferred from $U_{m>0}$ if need be.

Having constructed the transformation matrix U, the Hamiltonian becomes block-diagonal upon a change of basis: $H \to U^\dagger H U$. Due to the m-degeneracy, it suffices to study the blocks with $m = 0$ and $m = 1/2$ where we find all s-values. We denote these blocks $H_m = U_m^\dagger H U_m$. Assuming N is odd, $s_{\max} = (N+1)/2$ is an integer and the $s = s_{\max}$ multiplet will be in the $m = 0$-block – otherwise it will be in the $m = 1/2$-block.

$$
\left.
\begin{aligned}
H_{m=0} &\doteq \operatorname{diag}\left(H_0^{s_{\max}}, H_0^{s_{\max}-1}, ..., H_0^0 \right) \\
H_{m=1/2} &\doteq \operatorname{diag}\left(H_{1/2}^{s_{\max}-1/2}, H_{1/2}^{s_{\max}-3/2}, ..., H_{1/2}^{1/2} \right)
\end{aligned}
\right\} \quad N \text{ odd,}
$$

$$
\left.
\begin{aligned}
H_{m=0} &\doteq \operatorname{diag}\left(H_0^{s_{\max}-1/2}, H_0^{s_{\max}-3/2}, ..., H_0^0 \right) \\
H_{m=1/2} &\doteq \operatorname{diag}\left(H_{1/2}^{s_{\max}}, H_{1/2}^{s_{\max}-1}, ..., H_{1/2}^{1/2} \right)
\end{aligned}
\right\} \quad N \text{ even.}
\tag{5.45}
$$

Here, H_m^s is the part which has not yet been diagonalized in each (s, m)-block.

$$
H_m^s = \sum_{\chi,\chi'} |\chi, s, m\rangle \, \langle \chi, s, m | H | \chi', s, m \rangle \, \langle \chi', s, m |.
\tag{5.46}
$$

Diagonalizing $H_{m=0,1/2}^s$ for each $s = 0, 1/2, ..., s_{max}$, we find the full energy spectrum and the eigenstates. The degeneracy follows from the quantum number s; there are $2s + 1$ states with same energy but different $m = -s, -s + 1, ..., s$ in each multiplet. If we require the eigenstates for $m > 0, 1/2$ ($m < 0, 1/2$), we may apply the ladder operator S_+ (S_-) to the eigenstates $|n, s, m = 0\rangle$, $|n, s, m = 1/2\rangle$.

5.2.1   The dimensionality of spin-blocks

The unitary transformation $H \to U^\dagger H U$ outlined in the previous section block-diagonalizes the ZBW Hamiltonian by utilizing the spin-rotational symmetry of the system. In this section, we find the dimensions of the remaining blocks of $U^\dagger H U$, namely those we denoted $H^s_{m=0,1/2}$ with $s = 0, 1/2, ..., s_{\max}$. This is related to how one decomposes a composite system of n spin-1/2 particles into irreducible representations.

The general rule of angular momentum addition for two particles with spin s_1 and s_2 is

$$s_1 \otimes s_2 \sim s_1 + s_2 \oplus s_1 + s_2 - 1 \oplus ... \oplus |s_1 - s_2|. \tag{5.47}$$

The LHS represents eigenstates of S_1^z and S_2^z while the RHS are all the irreducible representations using eigenstates of the total spin: $\boldsymbol{S}_1 + \boldsymbol{S}_2$. A composite system of two spin-1/2 particles gives a triplet and a singlet.

$$\frac{1}{2} \otimes \frac{1}{2} \sim 1 \oplus 0. \tag{5.48}$$

Using this decomposition, three spin-1/2 particles combine in a quartet and two doublets.

$$\left(\frac{1}{2} \otimes \frac{1}{2} \right) \otimes \frac{1}{2} \sim (1 + 0) \otimes \frac{1}{2} \sim \frac{3}{2} \oplus \frac{1}{2} \oplus \frac{1}{2}. \tag{5.49}$$

Four spin-1/2 particles combine in a quintet, three triplets, and two singlets.

$$\left(\frac{1}{2} \otimes \frac{1}{2} \otimes \frac{1}{2} \right) \otimes \frac{1}{2} \sim \left(\frac{3}{2} \oplus \frac{1}{2} \oplus \frac{1}{2} \right) \otimes \frac{1}{2} \sim 2 \oplus 1 \oplus 1 \oplus 1 \oplus 0 \oplus 0. \tag{5.50}$$

One may continue this iterative expansion by adding one particle at a time.

Let $d(n, s)$ denote the number of singlets ($s = 0$), doublets ($s = 1/2$), triplets ($s = 1$), etc. in the decomposition of n spin-1/2 particles into irreducible representations. Then, the decomposition gives the recurrence relation

$$d(n, s) = d\left(n - 1, s - \frac{1}{2} \right) + d\left(n - 1, s + \frac{1}{2} \right), \quad n \geq 2, \quad 0 < s < \frac{n}{2};$$
$$d\left(n, s > \frac{n}{2} \right) = d(n, s < 0) = 0, \quad n \geq 1; \tag{5.51}$$
$$d\left(1, \frac{1}{2} \right) = 1.$$

When we add a spin-1/2 particle, the spin only changes by $s = \pm 1/2$. Therefore, the irreducible representations with spin s for n particles must come from irreducible representations with either spin $s - 1/2$ or $s + 1/2$ at $n - 1$ particles. Of course, $s = 0$ and $s = n/2$

n	s									
	0	$\frac{1}{2}$	1	$\frac{3}{2}$	2	$\frac{5}{2}$	3	$\frac{7}{2}$	4	$\frac{9}{2}$
1		1								
2	1		1							
3		2		1						
4	2		3		1					
5		5		4		1				
6	5		9		5		1			
7		14		14		6		1		
8	14		28		20		7		1	
9		42		48		27		8		1

Table 1: The number of irreducible representations $d(n,s)$ with combined spin s from the product of n spin-1/2 particles: $\bigotimes_{i=1}^{n} \frac{1}{2}$. Each entry is the sum of the two entries above it (Eq. (5.51)). Blank entries are zero as well as entries with $s < 0$.

are special cases, for they are only connected with $s = 1/2$ and $s = (n-1)/2$, respectively. Table 1 shows $d(n,s)$ for combining $1 \leq n \leq 9$ spin-1/2 particles. One finds that these form an asymmetric Pascal's triangle where an entry is the sum of the two entries above.

Given that there are $2s+1$ states in each multiplet, one may check that the dimension of the Hilbert space is still 2^n after the decomposition; e.g. for $n = 5$, $5 \cdot 2 + 4 \cdot 4 + 1 \cdot 6 = 32 = 2^5$.

For the ZBW Hamiltonian, we have to include the vacuum state and the doubly occupied state. In terms of angular momentum addition, these are "spin-0 particles". According to Eq. (5.47), this does not change the decomposition itself, only the number of times it has to be counted. The Fock states $|D, S_1, ..., S_N\rangle$ describe $N + 1$ "particles" in a 4^{N+1}-dimensional Hilbert space. We denote the number of irreducible representations with spin s by $D(N + 1, s)$, where

$$D(N, s) = \sum_{j=0}^{N} 2^j \binom{N}{j} d(N - j, s), \tag{5.52}$$

and $\binom{N}{j} = N!/(N - j)!j!$ is a binomial coefficient which counts the number of ways to place j "spin-0 particles" into a combined Fock state of N particles. The factor 2^j reflects the two choices of "spin-0 particle": vaccum or doubly occupied. Eq. (5.52) states that we

N	s					
	0	$\frac{1}{2}$	1	$\frac{3}{2}$	2	$\frac{5}{2}$
1	2	1				
2	5	4	1			
3	14	14	6	1		
4	42	48	27	8	1	
5	132	165	110	44	10	1

Table 2: The number of irreducible representations $D(N, s)$ with combined spin s from the product of $N - j$ spin-1/2 particles and j spin-0 particles of which there are two types: $\bigotimes_{i=1}^{N} \left(0 \oplus 0 \oplus \frac{1}{2}\right)$. Blank entries are zero as well as entries with $s < 0$.

can compute the number of irreducible representations with spin s by weighing the rows of Tab. 1 by the number of times we need to perform that particular decomposition. The values of $D(N, s)$ are collected in Tab. 2 for $1 \leq N \leq 5$.

Another way to look at it is the expansion of the product $\bigotimes_{i=1}^{N} \left(0 \oplus 0 \oplus \frac{1}{2}\right)$, which is directly related to the Fock states. Each single-particle state is either from a doublet ($s_i = 1/2$) or a singlet ($s_i = 0$), and there are two singlets (vacuum and doubly occupied states). Therefore, each term in the expansion corresponds to a unique Fock state. From the expansion follows a useful recurrence relation analogous to Eq. (5.51).

$$D(N, s) = 2D(N - 1, s) + D\left(N - 1, s - \frac{1}{2}\right) + D\left(N - 1, s + \frac{1}{2}\right), \quad N \geq 2, \quad 0 < s < \frac{N}{2};$$

$$D(1, 0) = 2; \quad D\left(1, \frac{1}{2}\right) = 1; \quad D\left(N, s > \frac{N}{2}\right) = D(N, s < 0) = 0.$$

$$(5.53)$$

This, in fact, implies that all the rows of Tab. 2 are contained in Tab. 1 if one ignores the blank spaces; compare rows $N = 1, 2, 3, 4$ from Tab. 2 with rows $n = 3, 5, 7, 9$ from Tab. 1.

The number $D(N, s)$ is precisely the dimension of the spin-blocks $H_{m=0,1/2}^{s}$. Thus, the problem of diagonalizing the ZBW Hamiltonian – originally a $4^{N+1} \times 4^{N+1}$ matrix – reduces to a set of smaller matrices of dimension $D(N+1, s)$, $s = 0, 1/2, ..., (N+1)/2$ given by Tab. 2. Numerically, this decomposition is more efficient due to the (time / space) complexity of eigenvalue and eigenvector determination. The added cost is just the determination of U, which only needs to be done once for each N (it is independent of model parameters), and a matrix product $H \to U^{\dagger} H U$ which needs to be done for each set of parameters.

With the matrix elements and the simplifying observations about 'good' quantum numbers in place, the Hamiltonian is readily diagonalized numerically. As we proceed down this avenue in the next section, we supplement the discussion with perturbation theory to understand the process of screening in the ZBW model. It is instructive to consider the single-lead S-QD system first.

5.3 YSR bound state in the single lead system

Let us study the atomic limit ($t \to 0$) of the single lead ($N = 1$) ZBW model and the leading order perturbative corrections. In the end, we will find a ground state transition at some finite t to a screened YSR singlet in the local moment regime.

We take $H_0 = H_S + H_D$ as the unperturbed Hamiltonian where

$$H_S = -\Delta c_\uparrow^\dagger c_\downarrow^\dagger - \Delta c_\downarrow c_\uparrow, \quad H_D = \epsilon_d n_d + U n_{d\uparrow} n_{d\downarrow}, \tag{5.54}$$

and treat

$$H_{S-D} = t \sum_\sigma \left(c_\sigma^\dagger d_\sigma + d_\sigma^\dagger c_\sigma \right) \tag{5.55}$$

as a perturbation. Note, that both Δ and t are real, positive numbers without loss of generality. In the unperturbed system there is no tunneling between the lead and the QD. Therefore, the ground state of the combined system is simply the combination of the isolated QD ground state and the isolated lead ground state. The atomic limit of the (normal metal) Anderson model was dicussed in Section 1.4. The only difference with superconducting leads is the condensation of electrons into Cooper pairs in the leads. Diagonalizing H_S, the eigenstates are $|\sigma_S\rangle = c_\sigma^\dagger |0_S\rangle$ with energy $E_S^\sigma = 0$ (at the Fermi level) and BCS states (cf. Eq. (3.6))

$$|+_S\rangle = \frac{1}{\sqrt{2}} \left(-|0_S\rangle + |\uparrow\downarrow_S\rangle \right), \quad |-_S\rangle = \frac{1}{\sqrt{2}} \left(|0_S\rangle + |\uparrow\downarrow_S\rangle \right), \tag{5.56}$$

with energies $E_S^\pm = \pm\Delta$. The subscript S is for superconductor (lead). The state $|-_S\rangle$ has lowest energy. The ground state of the isolated QD is determined by ϵ_d and U (see Fig. 1.2). The unperturbed eigenstates of the combined system and their energies are summarized in Tab. 3. From the previous section we know that we may decompose the 16-dimensional Hamiltonian into three blocks of dimension $5, 4, 1$ corresponding to $s = 0, 1/2, 1$, respectively (cf. Tab. 2).

	$s = m = 0$				
State	$(|\uparrow,\downarrow\rangle - |\downarrow,\uparrow\rangle)/\sqrt{2}$	$|0,-\rangle$	$|0,+\rangle$	$|\uparrow\downarrow,-\rangle$	$|\uparrow\downarrow,+\rangle$
E_0	ϵ_d	$-\Delta$	Δ	$2\epsilon_d + U - \Delta$	$2\epsilon_d + U + \Delta$

	$s = m = 1/2$				$s = m = 1$
State	$|\uparrow,-\rangle$	$|\uparrow,+\rangle$	$|\uparrow\downarrow,\uparrow\rangle$	$|0,\uparrow\rangle$	$|\uparrow,\uparrow\rangle$
E_0	$\epsilon_d - \Delta$	$\epsilon_d + \Delta$	$2\epsilon_d + U$	0	ϵ_d

Table 3: Unperturbed eigenstates and energies of $H_0 = H_S + H_D$ (Eq. (5.54)) for $N = 1$ lead in the ZBW approximation. Due to spin-rotational symmetry, energies are degenerate in m. Hence, only states with $s = m$ are shown. The states are written as $|\text{QD}, \text{Lead}\rangle$ with $|\pm\rangle$ defined in Eq. (5.56).

In the local moment regime $-U < \epsilon_d < 0$, the isolated QD ground state is $|\sigma_D\rangle$ with energy $E_D^\sigma = \epsilon_d$. Therefore, the (doublet) ground state of H_0 is

$$|D_0\rangle = |\sigma, -\rangle = |\sigma_D\rangle \otimes |-_S\rangle = \frac{1}{\sqrt{2}}\left(|\sigma, 0\rangle + |\sigma, \uparrow\downarrow\rangle\right). \tag{5.57}$$

The doublet has combined spin $s = 1/2$ and unperturbed energy $E_0^D = \langle D_0|H_0|D_0\rangle = \epsilon_d - \Delta$. Note that there are three other doublets than $|D\rangle$ in the system (with higher energy).

For some critical $t = t_c$, it will be energetically favorable to screen the local moment on the QD such that the ground state of H has spin $s = 0$. To find this critical tunneling rate, we will apply degenerate perturbation theory. Thus, we need to find the 'good' linear combinations in the degenerate subspace that split up when the perturbation is applied. Then we can apply the results of non-degenerate perturbation theory. We will limit our discussion to the local moment regime where the level spacings between $|0, -\rangle$, $|\uparrow\downarrow, -\rangle$ and the two degenerate states $|\uparrow,\downarrow\rangle$, $|\downarrow,\uparrow\rangle$ are large: $\Delta - U \ll \epsilon_d \ll -\Delta$. For small Δ, we can find such ϵ_d, but at $\Delta \simeq U/2$, this obviously breaks down for all ϵ_d. In this regime, we can neglect the mixing between these states and focus on how the degeneracy between $|\uparrow,\downarrow\rangle$ and $|\downarrow,\uparrow\rangle$ is lifted.

If we apply the perturbation to these states and project onto the unperturbed eigen-

states, we find

$$H_{S-D}\left|\uparrow,\downarrow\right\rangle = t\left(\left|0,\uparrow\downarrow\right\rangle + \left|\uparrow\downarrow,0\right\rangle\right) = \frac{t}{\sqrt{2}}\left(\left|0,+\right\rangle + \left|0,-\right\rangle + \left|\uparrow\downarrow,-\right\rangle - \left|\uparrow\downarrow,+\right\rangle\right), \quad (5.58a)$$

$$H_{S-D}\left|\downarrow,\uparrow\right\rangle = -H_{S-D}\left|\uparrow,\downarrow\right\rangle. \quad (5.58b)$$

It is clear that the symmetric combination

$$\left|s=1, m=0\right\rangle = \frac{1}{\sqrt{2}}\left(\left|\uparrow,\downarrow\right\rangle + \left|\downarrow,\uparrow\right\rangle\right) \quad (5.59)$$

is an eigenstate of the full Hamiltonian $H = H_0 + H_{S-D}$ (with energy $E^{s=1} = \epsilon_d$). It is not affected by the perturbation at all. This is just a statement about spin-rotational symmetry; with only one lead, there is just one triplet ($s = 1$) and, therefore, no further mixing. The odd combination

$$\left|S_0\right\rangle = \left|\chi=1, s=0, m=0\right\rangle = \frac{1}{\sqrt{2}}\left(\left|\uparrow,\downarrow\right\rangle - \left|\downarrow,\uparrow\right\rangle\right) \quad (5.60)$$

is not an eigenstate of $H_0 + H_{S-D}$, however, since it mixes with $\left|0,\uparrow\downarrow\right\rangle$ and $\left|\uparrow\downarrow,0\right\rangle$. The χ-label is there to remind us, that $\left|S_0\right\rangle$ is just one of the five singlets that will mix when we turn on H_{S-D}. We will refer to $\left|S\right\rangle$ as the screened YSR singlet. In the limit $t \to 0$, $\left|s=1, m=0\right\rangle$ and $\left|s=0, m=0\right\rangle$ are degenerate but they are the 'good' states to use for non-degenerate perturbation theory since they obey the spin-rotational symmetry.

Now we compare the perturbative energies of the doublet $\left|D\right\rangle$ and singlet $\left|S\right\rangle$. Using Eq. (5.58), we find

$$H_{S-D}\left|D_0\right\rangle = \frac{t}{\sqrt{2}}\left(\left|0,\sigma\right\rangle - \left|\uparrow\downarrow,\sigma\right\rangle\right), \quad (5.61a)$$

$$H_{S-D}\left|S_0\right\rangle = t\left(\left|0,+\right\rangle + \left|0,-\right\rangle + \left|\uparrow\downarrow,-\right\rangle - \left|\uparrow\downarrow,+\right\rangle\right). \quad (5.61b)$$

From here, it is easy to see that the first order energy corrections are zero: $\langle D_0|H_{S-D}|D_0\rangle = \langle S_0|H_{S-D}|S_0\rangle = 0$. Summing over all other eigenstates $|n\rangle$ of H_0, the second order terms are

$$\delta E_2^D = \sum_n \frac{|\langle n|H_{S-D}|D_0\rangle|^2}{E_0^D - E_0^n} = -\frac{t^2}{2}\left(\frac{1}{\Delta - \epsilon_d} + \frac{1}{\epsilon_d + U + \Delta}\right), \quad (5.62a)$$

$$\delta E_2^S = \sum_n \frac{|\langle n|H_{S-D}|S_0\rangle|^2}{E_0^S - E_0^n} = -t^2\left(\frac{1}{\Delta - \epsilon_d} - \frac{1}{\Delta + \epsilon_d} + \frac{1}{\epsilon_d + U - \Delta} + \frac{1}{\epsilon_d + U + \Delta}\right). \quad (5.62b)$$

Close to the particle-hole symmetric point $\epsilon_d \simeq -U/2$ and with large Coulomb repulsion $U \gg \Delta$, we may neglect Δ in all terms. It is then clear that both corrections are negative and that the correction to the singlet state is larger: $\delta E_2^S/\delta E_2^D \simeq 4$. The singlet has more tunneling options and becomes more delocalized. Thus, at some finite $t = t_c$, we expect an energy level crossing: $E^D - E^S = 0$.

$$E^D - E^S = -\Delta + t^2 \left(\frac{1/2}{\Delta - \epsilon_d} - \frac{1}{\Delta + \epsilon_d} + \frac{1}{\epsilon_d + U - \Delta} + \frac{1/2}{\epsilon_d + U + \Delta} \right). \tag{5.63}$$

We find that the critical tunneling rate is given by

$$t_{c,\,\text{p.t.}}^2 = \frac{2\Delta}{\frac{1}{\Delta - \epsilon_d} - \frac{2}{\Delta + \epsilon_d} + \frac{2}{\epsilon_d + U - \Delta} + \frac{1}{\epsilon_d + U + \Delta}}. \tag{5.64}$$

The subscript "p.t." stands for "perturbation theory" and is meant to discern it from the true critical tunneling rate t_c we find from numerical diagonalization of H. As expected, in the case of a normal metallic lead ($\Delta = 0$) in the local moment regime, the screened singlet becomes the ground state for finite tunneling ($t > t_c = 0$). This is the ZBW version of the Kondo effect when $T_K \gg \Delta$; the YSR singlet becomes the Kondo singlet in this limit. For a superconducting lead, it takes extra persuasion ($t_c > 0$) to convince the lead to split up the Cooper pair and screen the local moment on the QD; it only happens if $\delta E_2^D - \delta E_2^S > \Delta$.

   The eigenenergies of H are shown in Fig. 5.1 as a function of t at the particle-hole symmetric point $\epsilon_d = -U/2$ for a small $\Delta = 0.1U$. The doublet-singlet phase transition occurs at $t = t_c \approx 0.14U$, but second order perturbation theory (dashed curves) estimates $t_{c,\,\text{p.t.}} \approx 0.12U$ (Eq. (5.64)). Since the doublet and singlet have different quantum numbers $s = 1/2, 0$, they don't mix and are allowed to cross each other in energy. The corresponding eigenstates $|D\rangle$ and $|S\rangle$ are shown in Fig. 5.2 at the energy-crossing ($t = t_c \approx 0.14U$). They have very large overlap with the unperturbed states $|D_0\rangle$ and $|S_0\rangle$, respectively. The singlet, in particular, shows some (small) charge fluctuations which would increase with larger Δ. In the proximitized limit, the lowest energy singlet resembles the BCS state $|-,-\rangle = (|0,-\rangle + |\uparrow\downarrow,-\rangle)/\sqrt{2}$.

   Fig. 5.3(a) shows how $t_{c,\,\text{p.t.}}$ (Eq. (5.64)) varies around the particle-hole symmetric point. As mentioned, our perturbative results are only valid in region $\Delta - U \ll \epsilon_d \ll -\Delta$. In this region, we compare with the exact result (numerical diagonalization of $H = H_0 + H_{S-D}$) in Fig. 5.3(b). For $\Delta \ll U$, t_c is small and the agreement is excellent. As we move away from particle-hole symmetry or increase Δ, the discrepancy grows and perturbation
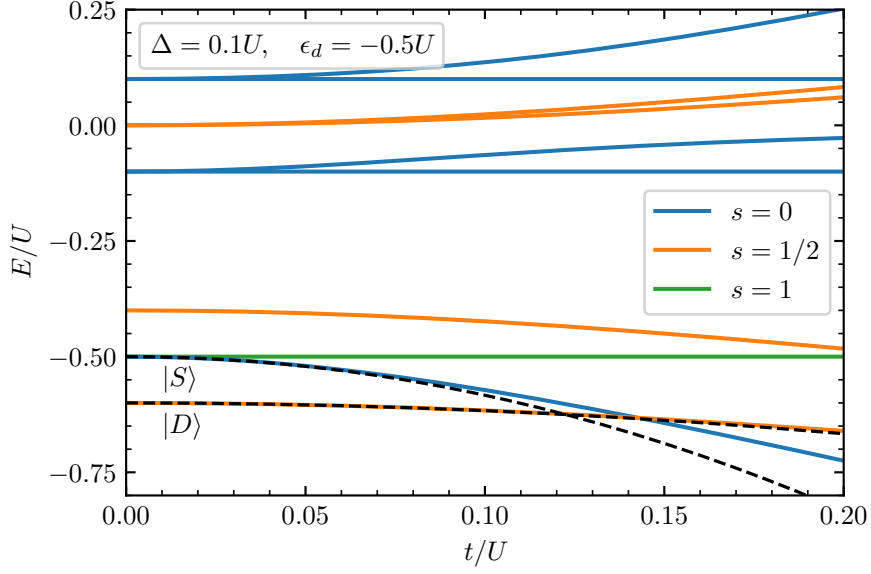
Figure 5.1: ZBW eigenenergies of $H = H_0 + H_{S-D}$ as function of the tunneling rate t. Black dashed curves are the second order energy corrections (Eq. (5.62)). The doublet-singlet phase transition occurs at $t = t_c \approx 0.14U$ while $t_{c, \text{ p.t.}} \approx 0.12U$ (Eq. (5.64)). Parameters used: $\Delta = 0.1U$, $\epsilon_d = -U/2$.
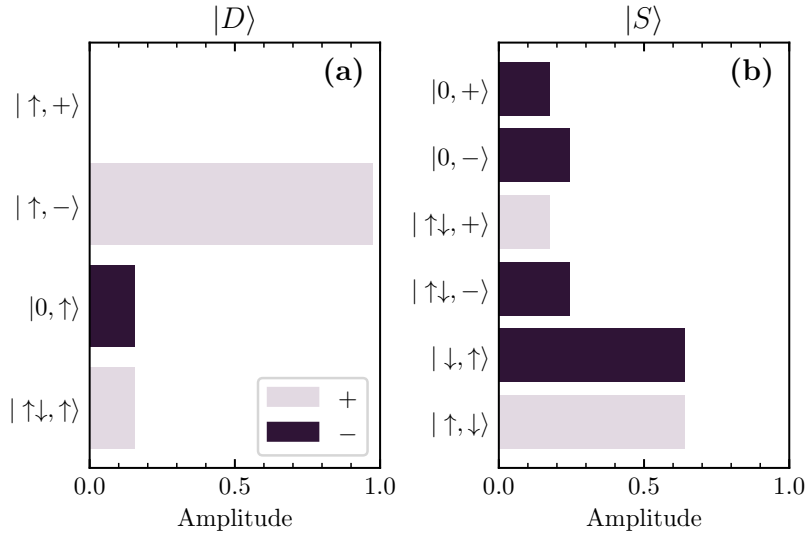

Figure 5.2: Lowest energy ZBW eigenstates $|D\rangle$ (a) and $|S\rangle$ (b) at the critical tunneling rate $t_c \approx 0.14U$. The phase is encoded in the bar color (grey: 0, black: π); with parameters as real numbers, the eigenvectors are chosen to be real. Other parameters used (same as Fig. 5.1): $\Delta = 0.1U$, $\epsilon_d = -U/2$.
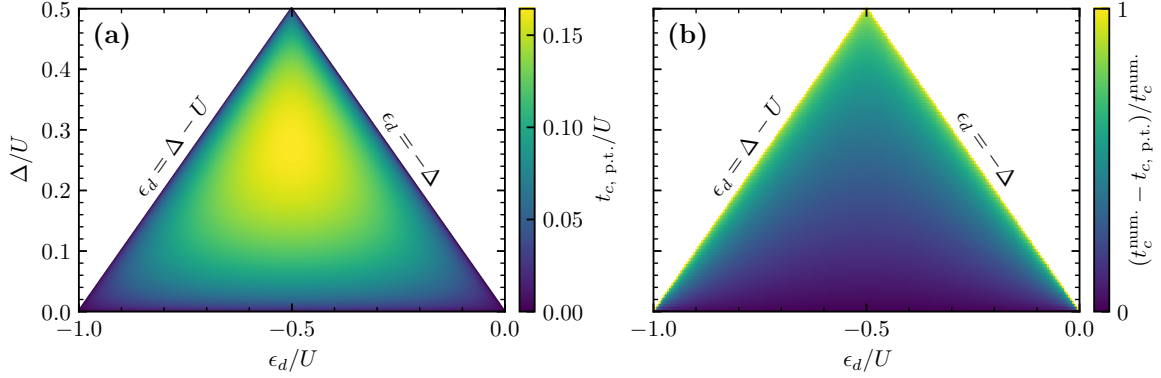
Figure 5.3: ZBW critical tunneling rate for the singlet-doublet phase transition in second order perturbation theory in t around particle-hole symmetry in the region of validity: $\Delta - U < \epsilon_d < -\Delta$. (a) shows $t_{c, \text{p.t.}}$ calculated with Eq. (5.64). (b) shows the relative error between Eq. (5.64) and numerical diagonalization of $H = H_0 + H_{S-D}$.

theory underestimates t_c; it is worst close to the lines $\epsilon_d = \Delta - U$ and $\epsilon_d = -\Delta$ where our perturbation theory breaks down and $t_{c, \text{p.t.}}$ goes to zero.

5.4 YSR bound states in the two-lead system

When we add another lead, we can study the effect of asymmetries and interference effects. Now, the unperturbed Hamiltonian $H_0 = H_S + H_D$ is given by the terms

$$H_S = - \sum_{\alpha=L,R} \left(\Delta_\alpha c_{\alpha\uparrow}^\dagger c_{\alpha\downarrow}^\dagger + \Delta_\alpha^* c_{\alpha\downarrow} c_{\alpha\uparrow} \right), \quad H_D = \epsilon_d n_d + U n_{d\uparrow} n_{d\downarrow}, \tag{5.65}$$

where the summation runs over the left (L) and right (R) lead. The tunneling perturbation is

$$H_{S-D} = \sum_{\alpha\sigma} \left(t_\alpha c_{\alpha\sigma}^\dagger d_\sigma + t_\alpha d_\sigma^\dagger c_{\alpha\sigma} \right). \tag{5.66}$$

Again, we limit our discussion to the local moment regime: $|\Delta_\alpha| - U \ll \epsilon_d \ll -|\Delta_\alpha|$. We will only study the Δ-asymmetric case ($|\Delta_L| \ll |\Delta_R|$) with perturbation theory since symmetric gaps requires us to resolve a degeneracy which only lifts to second order in t; the point is not to test or use perturbation theory directly, but merely as a tool to aid our understanding of the model. Without loss of generality, we have taken the left lead to be the one with the smaller gap in the following.

All unperturbed energies are found in Tab. 4 along with the corresponding eigenstates for $s = m$. Being in the local moment regime means that the ground state will be a state

with only a single electron occupying the QD. Thus, most states from Tab. 4 will not be ground state candidates due to their high energy. The unperturbed ground state is the doublet $|D_0\rangle = |\sigma, -, -\rangle$ from the block with $s = 1/2$. This expands to

$$|D_0\rangle = |\sigma, -, -\rangle = \frac{1}{2}\left(|\sigma, 0, 0\rangle + e^{i\varphi_L}|\sigma, \uparrow\downarrow, 0\rangle + e^{i\varphi_R}|\sigma, 0, \uparrow\downarrow\rangle + e^{i(\varphi_L + \varphi_R)}|\sigma, \uparrow\downarrow, \uparrow\downarrow\rangle\right).$$
(5.67)

As in the single lead case, a screened YSR singlet will become the ground state for sufficiently large tunneling. In the Δ-asymmetric case, the two unperturbed screening states

$$\begin{aligned}
\left|S_0^L\right\rangle &= \frac{1}{\sqrt{2}}\left(|\uparrow, \downarrow, -\rangle - |\downarrow, \uparrow, -\rangle\right), \\
\left|S_0^R\right\rangle &= \frac{1}{\sqrt{2}}\left(|\uparrow, -, \downarrow\rangle - |\downarrow, -, \uparrow\rangle\right),
\end{aligned}$$
(5.68)

which describes screening by the left and right lead, respectively, are non-degenerate with energies $E_0^L = \epsilon_d - |\Delta_R|$ and $E_0^R = \epsilon_d - |\Delta_L|$. If the left lead – which we assumed to have the smallest gap: $|\Delta_L| \ll |\Delta_R|$ – couples at least as much to the QD as the right lead: $t_L \geq t_R$, we expect the screening to be done primarily by the left lead. We will call this $(t_L > t_R$ or $t_L < t_R)$ a t-asymmetry. In this case, $\left|S^L\right\rangle$ will cross $|D\rangle$ in energy at some critical $t = t_c$. If the tunneling is skewed in the right lead's favor $(t_R > t_L)$, it is unclear which of the two leads will be the 'primary screener'. Then, $\left|S^L\right\rangle$ might mix a lot with $\left|S^R\right\rangle$ before it crosses $|D\rangle$ in energy. In terms of energy scales, if $|\Delta_R| + t_L^2/U \gg |\Delta_L| + t_R^2/U$, it will be energetically favorable to break apart the Cooper pair in the left (not right) lead and screen the local moment. Hence, the left lead will be the 'primary screener'. In the opposite case, the roles are reversed and the right lead will be the 'primary screener'. In the intermediate case, both leads will participate and screen the local moment on the QD coherently. We will see examples of this shortly.

In both t-asymmetric cases, we consider the second order energy correction to both $\left|S_0^L\right\rangle$ and $\left|S_0^R\right\rangle$. Applying the perturbation to the singlets, we find

$$\begin{aligned}
H_{S-D}\left|S_0^L\right\rangle &= t_L\left(|0, +, -\rangle + e^{-i\varphi_L}|0, -, -\rangle + |\uparrow\downarrow, -, -\rangle - e^{i\varphi_L}|\uparrow\downarrow, +, -\rangle\right) \\
&\quad - \frac{t_R}{2}\left(|0, \downarrow, \uparrow\rangle - e^{i\varphi_R}|\uparrow\downarrow, \downarrow, \uparrow\rangle - |0, \uparrow, \downarrow\rangle + e^{i\varphi_R}|\uparrow\downarrow, \uparrow, \downarrow\rangle\right),
\end{aligned}$$
(5.69a)

$$\begin{aligned}
H_{S-D}\left|S_0^R\right\rangle &= t_R\left(|0, -, +\rangle + e^{-i\varphi_R}|0, -, -\rangle + |\uparrow\downarrow, -, -\rangle - e^{i\varphi_R}|\uparrow\downarrow, -, +\rangle\right) \\
&\quad + \frac{t_L}{2}\left(|0, \uparrow, \downarrow\rangle - e^{i\varphi_L}|\uparrow\downarrow, \uparrow, \downarrow\rangle - |0, \downarrow, \uparrow\rangle + e^{i\varphi_L}|\uparrow\downarrow, \downarrow, \uparrow\rangle\right).
\end{aligned}$$
(5.69b)

	$s = m = 0$		
State	$\left|\uparrow,\downarrow,\pm\right\rangle - \left|\downarrow,\uparrow,\pm\right\rangle$	$\left|\uparrow,\pm,\downarrow\right\rangle - \left|\downarrow,\pm,\uparrow\right\rangle$	$\left|^0_{\uparrow\downarrow},\uparrow,\downarrow\right\rangle - \left|^0_{\uparrow\downarrow},\downarrow,\uparrow\right\rangle$
E_0	$\epsilon_d \pm |\Delta_R|$	$\epsilon_d \pm |\Delta_L|$	$\left\{ \begin{array}{c} 0 \\ 2\epsilon_d + U \end{array} \right\}$

	$\left|^0_{\uparrow\downarrow},\pm,\pm\right\rangle$		$\left|^0_{\uparrow\downarrow},\pm,\mp\right\rangle$
State			
E_0	$\left\{ \begin{array}{c} \pm|\Delta_L| \pm |\Delta_R| \\ 2\epsilon_d + U \pm |\Delta_L| \pm |\Delta_R| \end{array} \right\}$		$\left\{ \begin{array}{c} \pm|\Delta_L| \mp |\Delta_R| \\ 2\epsilon_d + U \pm |\Delta_L| \mp |\Delta_R| \end{array} \right\}$

	$s = m = 1/2$	
State	$\left|\downarrow,\uparrow,\uparrow\right\rangle + c\left|\uparrow,\downarrow,\uparrow\right\rangle + c^2\left|\uparrow,\uparrow,\downarrow\right\rangle$	$\left|\downarrow,\uparrow,\uparrow\right\rangle + c^2\left|\uparrow,\downarrow,\uparrow\right\rangle + c\left|\uparrow,\uparrow,\downarrow\right\rangle$
E_0	ϵ_d	ϵ_d

	$\left|\uparrow,\pm,\pm\right\rangle$	$\left|\uparrow,\pm,\mp\right\rangle$
State		
E_0	$\epsilon_d \pm |\Delta_L| \pm |\Delta_R|$	$\epsilon_d \pm |\Delta_L| \mp |\Delta_R|$

	$\left|^0_{\uparrow\downarrow},\pm,\uparrow\right\rangle$	$\left|^0_{\uparrow\downarrow},\uparrow,\pm\right\rangle$
State		
E_0	$\left\{ \begin{array}{c} \pm|\Delta_L| \\ 2\epsilon_d + U \pm |\Delta_L| \end{array} \right\}$	$\left\{ \begin{array}{c} \pm|\Delta_R| \\ 2\epsilon_d + U \pm |\Delta_R| \end{array} \right\}$

	$s = m = 1$			$s = m = 3/2$
State	$\left|\uparrow,\uparrow,\pm\right\rangle$	$\left|\uparrow,\pm,\uparrow\right\rangle$	$\left|^0_{\uparrow\downarrow},\uparrow,\uparrow\right\rangle$	$\left|\uparrow,\uparrow,\uparrow\right\rangle$
E_0	$\epsilon_d \pm |\Delta_R|$	$\epsilon_d \pm |\Delta_L|$	$\left\{ \begin{array}{c} 0 \\ 2\epsilon_d + U \end{array} \right\}$	ϵ_d

Table 4: Unperturbed eigenstates and energies of $H_0 = H_S + H_D$ (Eq. (5.54)). Due to spin-rotational symmetry, energies are degenerate in m. Hence, only states with $s = m$ are shown. For easy of readability, the composite states are not normalized and $c = e^{2\pi i/3}$ with the property $1 + c + c^2 = 0$ that ensures orthogonality.

In terms of energy corrections, the screening lead gives a contribution similar to Eq. (5.62b) and the other lead gives a contribution similar to Eq. (5.62a).

$$\delta E_2^{L(R)} = -t_{L(R)}^2 \left(\frac{1}{\left|\Delta_{L(R)}\right| - \epsilon_d} - \frac{1}{\left|\Delta_{L(R)}\right| + \epsilon_d} + \frac{1}{\epsilon_d + U - \left|\Delta_{L(R)}\right|} + \frac{1}{\epsilon_d + U + \left|\Delta_{L(R)}\right|} \right)$$
$$- \frac{t_{R(L)}^2}{2} \left(\frac{1}{\left|\Delta_{R(L)}\right| - \epsilon_d} + \frac{1}{\epsilon_d + U + \left|\Delta_{R(L)}\right|} \right),$$
(5.70)

The difference between δE_2^L and δE_2^R is just the interchange of L and R. Applying the perturbation to the unperturbed doublet ground state $|D_0\rangle = |\sigma, -, -\rangle$, we find

$$H_{S-D} |D_0\rangle = \frac{-t_L}{\sqrt{2}} \left(|0, \sigma, -\rangle - e^{i\varphi_L} |\uparrow\downarrow, \sigma, -\rangle \right) + \frac{t_R}{\sqrt{2}} \left(|0, -, \sigma\rangle - e^{i\varphi_R} |\uparrow\downarrow, -, \sigma\rangle \right). \quad (5.71)$$

This leads to an energy shift of

$$\delta E_2^D = -\frac{t_L^2}{2} \left(\frac{1}{|\Delta_L| - \epsilon_d} + \frac{1}{\epsilon_d + U + |\Delta_L|} \right) - \frac{t_R^2}{2} \left(\frac{1}{|\Delta_R| - \epsilon_d} + \frac{1}{\epsilon_d + U + |\Delta_R|} \right). \quad (5.72)$$

The second term of Eq. (5.70) is contained in Eq. (5.72) and, thus, eliminated from the energy difference.

$$E^D - E^{L(R)} = -\left|\Delta_{L(R)}\right| + t_{L(R)}^2 \left(\frac{1/2}{\left|\Delta_{L(R)}\right| - \epsilon_d} - \frac{1}{\left|\Delta_{L(R)}\right| + \epsilon_d} \right.$$
$$\left. + \frac{1}{\epsilon_d + U - \left|\Delta_{L(R)}\right|} + \frac{1/2}{\epsilon_d + U + \left|\Delta_{L(R)}\right|} \right). \quad (5.73)$$

This is completely equivalent to the single lead case (cf. Eq. (5.63)) and gives two critical tunneling rates – one for each lead (Eq. (5.64)). One can easily generalize this to an arbitrary number of leads as long as the system is Δ-asymmetric.

The characteristics of the YSR state is dependent on the level of t-asymmetry. In Fig. 5.4 the bound state energy spectrum is shown when varying the average tunneling rate $t = (t_L + t_R)/2$ for fixed ratios t_R/t_L. This is done for a Δ-asymmetric setup ($|\Delta_L| = 0.05U$, $|\Delta_R| = 0.2U$) at particle-hole symmetry. For $t_R = t_L$ (Fig. 5.4(a)), the situation is analogous to a single-lead setup since the right lead is not participating in the screening. We see the same crossover as in Fig. 5.1. As the ratio t_R/t_L is increased, the right lead takes over the screening and we observe an avoided crossing between $\left|S^L\right\rangle$ and $\left|S^R\right\rangle$ in the energy spectrum. This is most noticeable in Fig. 5.4(c).

This explanation is inferred from the eigenstates which are shown in Fig. 5.5 for the lowest energy state in the $s = 0$ spin block (the YSR state) at $t = t_c$. For $t_R = t_L$ (Fig.
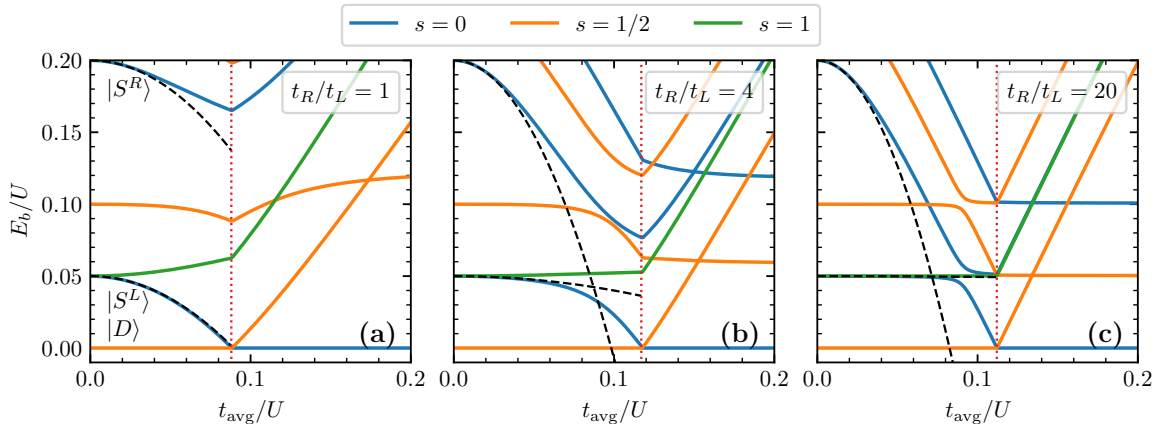
Figure 5.4: Bound state energy ($E_b = E - E_{\text{ground state}}$) as a function of the average tunneling rate $t_{\text{avg}} = (t_L + t_R)/2$ in the Δ-asymmetric two-lead ZBW system for different coupling ratios. The black dashed curves are the second order energy corrections around $t = 0$ (Eq. (5.73)) which are plotted up to the doublet-singlet phase transition (red dotted line). Note that many levels are outside the plotted energy window, including the quartet ($s = 3/2$). Parameters used: $|\Delta_L| = 0.05U$, $|\Delta_R| = 0.2U$, $\varphi_L - \varphi_R = 0$, $\epsilon_d = -U/2$.

5.5(a)), the YSR state is predominantly screening by the left lead ($\left|S_0^L\right\rangle$ – Eq. (5.68)) when we only consider the two components with largest amplitude. For $t_R/t_L = 4$, the YSR state can be very well described as $\left|S_0^L\right\rangle + \left|S_0^R\right\rangle$, i.e. coherent screening between the left and right lead. And for $t_R/t_L = 20$, the YSR state is mostly screening by the right lead ($\left|S_0^R\right\rangle$). The other states with smaller amplitudes are the ones from Eq. (5.69).

5.5 Energy dispersion and current-phase relations

So far we have not addressed the phase bias of a two-lead ZBW system. We have only studied systems with $\varphi_L = \varphi_R$. As previously mentioned, we have some gauge freedom when we choose the phases. Here, we define $\varphi \equiv \varphi_L - \varphi_R$ which is 2π-periodic and lives in the (first) Brillouin zone: $\varphi \in [0, 2\pi)$. In this context, we may refer to the phase-dependence of the energy, $E(\varphi)$, as the energy dispersion. In Fig. 5.6, we show the dispersion for different coupling strengths/asymmetries as well as away from particle-hole symmetry. The degree of particle-hole symmetry is parametrized by the dimensionless quantity $x = 1 + 2\epsilon_d/U$ which is zero at particle-hole symmetry and $x = \pm 1$ at the charge-degeneracy points. For symmetric coupling and at particle-hole symmetry (Figs. 5.6(a)–
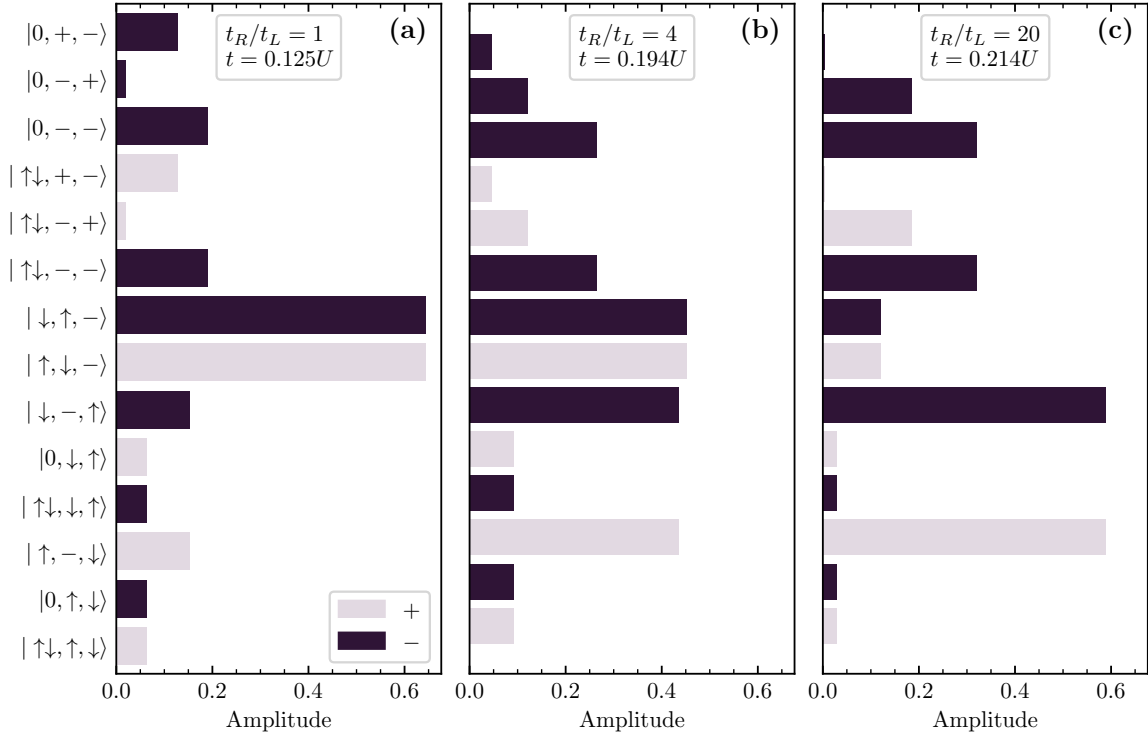
Figure 5.5: YSR eigenstates (lowest energy singlet) from Fig. 5.4 at the critical tunneling rate / doublet-singlet phase transition. Only the components with non-zero amplitude are shown. The phase is encoded in the bar color (grey: 0, black: π). Parameters used (same as Fig. 5.4): $|\Delta_L| = 0.05U$, $|\Delta_R| = 0.2U$, $\varphi_L - \varphi_R = 0$, $\epsilon_d = -U/2$.

(c)), the ground state is a doublet for all $\varphi \in [0, 2\pi)$ when the coupling is weak (Fig. 5.6(a)), but a singlet ground state is found for stronger coupling (Figs. 5.6(b)–(c)) except close to $\varphi = \pi$ where the ground state remains a doublet. This is still true for even stronger coupling ($t > 0.2U$) as long as $x = 0$ and $t_L = t_R$, but the doublet region shrinks. A Weyl point is located at $\varphi = \pi$ where the two singlet (and triplet) levels touch. As was the case with the infinite gap limit (Section 3), this degeneracy is lifted when moving away from particle-hole symmetry (Figs. 5.6(d)–(f)) or with an asymmetric coupling (Figs. 5.6(g)–(i)). In both cases, there is no protected doublet region around $\varphi = \pi$; the ground state is a singlet for all $\varphi \in [0, 2\pi)$ at strong coupling (Figs. 5.6(f) and 5.6(i)). In this way, particle-hole asymmetry and coupling asymmetry has the same effect on the energy levels. Note, however, that the (small) coupling asymmetry mostly affects the energy levels that meet at the Weyl point $\varphi = \pi$ (forces an avoided crossing) and only close to $\varphi = \pi$, while particle-hole asymmetry affects all energy levels in the whole φ-range. In other words, the coupling asymmetry only opens a gap between degenerate levels at the Weyl point.

Even in systems with Δ-asymmetry, it is possible to tune t_L and t_R such that the gap between the two singlets with lowest energy closes at $\varphi = \pi$. This still seems to require particle-hole symmetry, however. Furthermore, the doublet remains the ground state at $\varphi = \pi$; the singlet is not pushed below the doublet – not even at strong coupling. In Fig. 5.7(a), we show how the singlet gap in Fig. 5.6(h) closes with a fine-tuned Δ-asymmetry. Only the singlets are degenerate at $\varphi = \pi$ (not the triplets) and this Weyl point is not protected against a change in coupling strength t_{avg} (cf. Figs. 5.6(a)–(c)). In Fig. 5.7(b) we plot the set of parameter configurations that keep the singlet gap closed. These surfaces are parametrized by $|\Delta_L|/U$. For large couplings ($t_L, t_R \gg |\Delta_L|, |\Delta_R|$), $|\Delta_R|/|\Delta_L|$ seems to be proportional to $(t_R/t_L)^2$ (a straight line in the plot). The surfaces touch on the line of Δ- and t-symmetry, meaning the Weyl point is proteced against coupling strength variations t_{avg} in this case (as shown in Figs. 5.6(a)–(c)).

The energy dispersion is important for the physical system. It determines the super-current that runs across the junction (here in arbitrary units).

$$I = \frac{\partial E_{GS}}{\partial \varphi}. \tag{5.74}$$

Junctions are often categorized according to their current-phase relation (CPR). If the phase is a free variable, the system chooses the phase which minimizes the (free) energy. If the energy minimum is at $\varphi = 0$ or $\varphi = \pi$, the junction is referred to as a 0- or π-junction, respectively. It may also be noted that the singlet-doublet phase transition, we have been
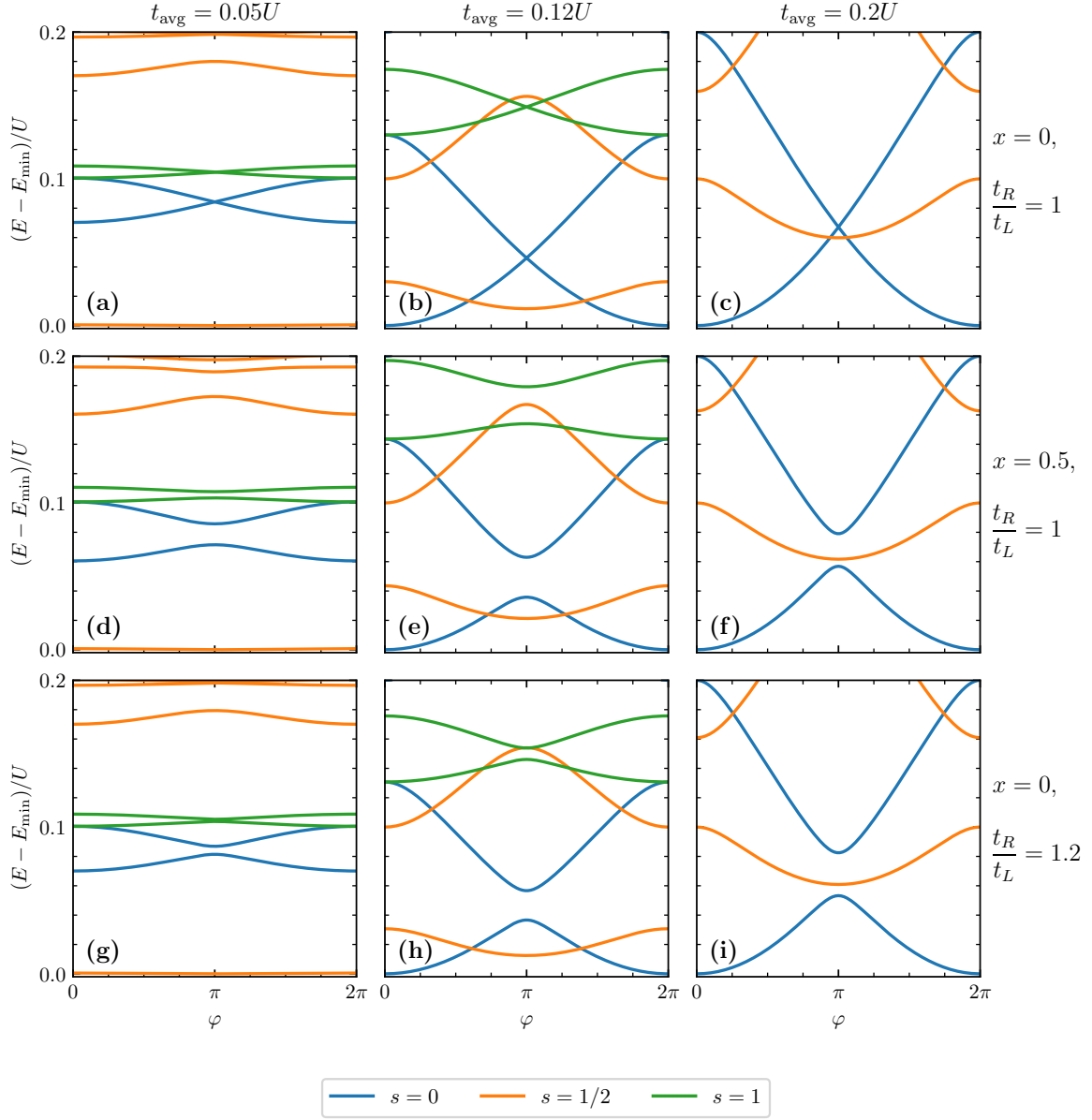
Figure 5.6: ZBW energy dispersions in the Δ-symmetric two-lead system. The average tunneling rate $t_{\mathrm{avg}} = (t_L + t_R)/2$ as well as particle-hole asymmetry $x = 1 + 2\epsilon_d/U$ and coupling ratio t_R/t_L are varied between panels as indicated by the column and row labels. Note that many levels are outside the plotted energy window of 2Δ, including the quartet ($s = 3/2$). Common parameters: $|\Delta_L| = |\Delta_R| = 0.1U$.
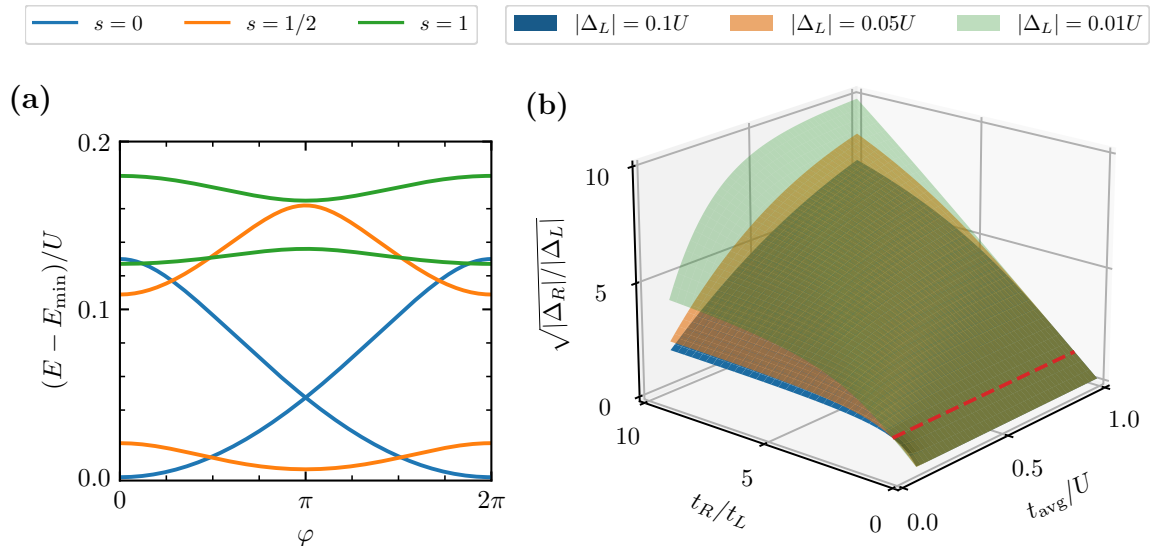
Figure 5.7: Weyl points with asymmetric couplings and SC gaps. (a) shows a Weyl point at $\varphi = \pi$ where the two singlets with lowest energy become degenerate – compare with Fig. 5.6(h). The set of configurations of t_α and Δ_α which closes the singlet gap are shown in (b) for fixed values of $|\Delta_L|/U$. In the symmetric case, all surfaces touch (dashed red line). Parameters used in (a) are the same as in Fig. 5.6(h) except for $|\Delta_R| = 0.122U$. Parameters used in (b): $x = 0$, $\varphi = \pi$.

	π	π'	$0'$	0
t_{avg}/U	0.05	0.105	0.2	0.2
t_R/t_L	1.0	1.0	1.0	1.2
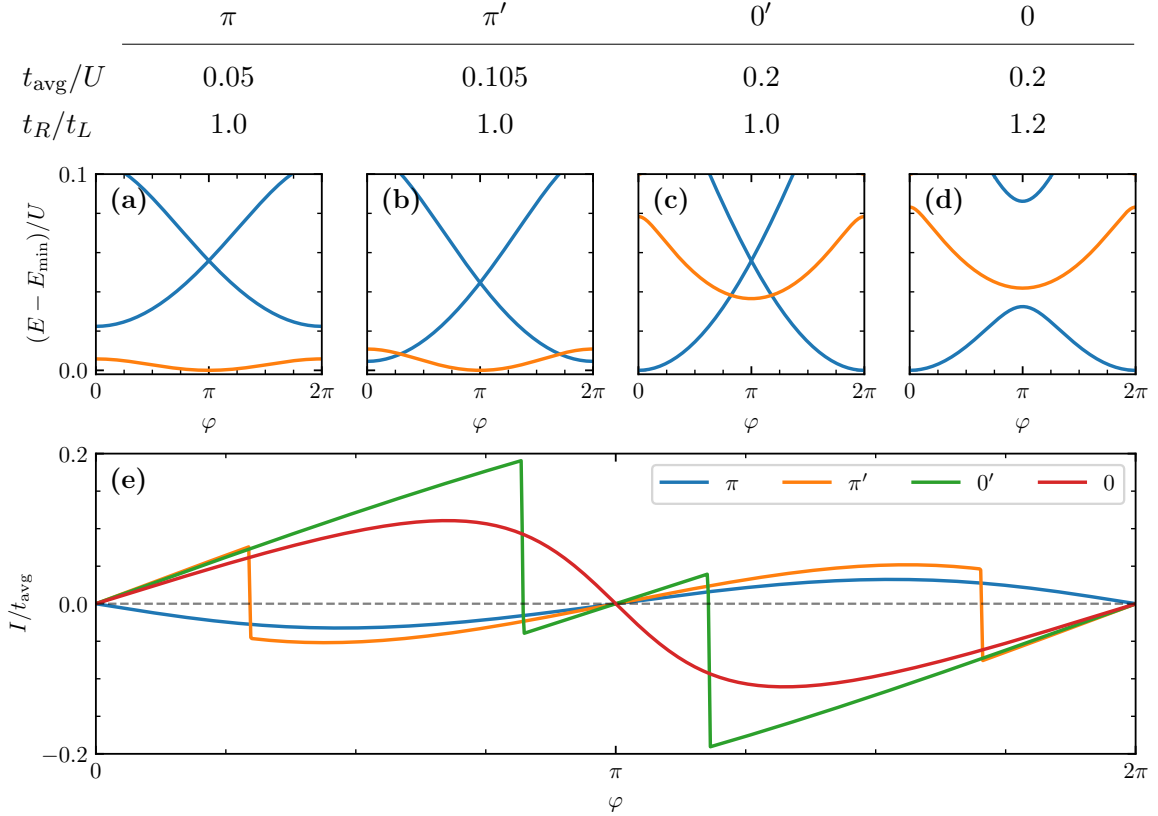
Figure 5.8: Exemplary energy dispersions (a)-(d) and corresponding current-phase relations (e) for the four different junction types: π, π', $0'$, and 0. In (a)-(d), the blue (orange) lines are $s = 0$ ($s = 1/2$). Discontinuities in the current are due to quantum phase transitions. Common parameters: $|\Delta_L| = |\Delta_R| = 0.1U$, $x = 0$.

concerned with, is also commonly referred to as a 0-π-transition due to the shift in energy minimum. As is evident from e.g. Fig. 5.7(a), the ground state may change when φ is varied (GS: singlet $\rightarrow$ doublet $\rightarrow$ singlet). This leads to a discontinuous current flow and provides a further distinction within 0- and π-junctions. Such junctions are referred to as $0'$- or π'-junctions, depending on where the global energy minimum is. Examples of the four different junction types are shown in Fig. 5.8.

The ZBW approximation produce, qualitatively, the same phase diagrams that we have previously studied – e.g. Fig. 4.4. In Fig. 5.9, we show phase diagrams for different two-terminal junctions with both symmetric and asymmetric couplings and SC gaps. For a junction with symmetric coupling ($t_L = t_R$) and equal gaps ($|\Delta_L| = |\Delta_R|$) as in Fig. 5.9(a),
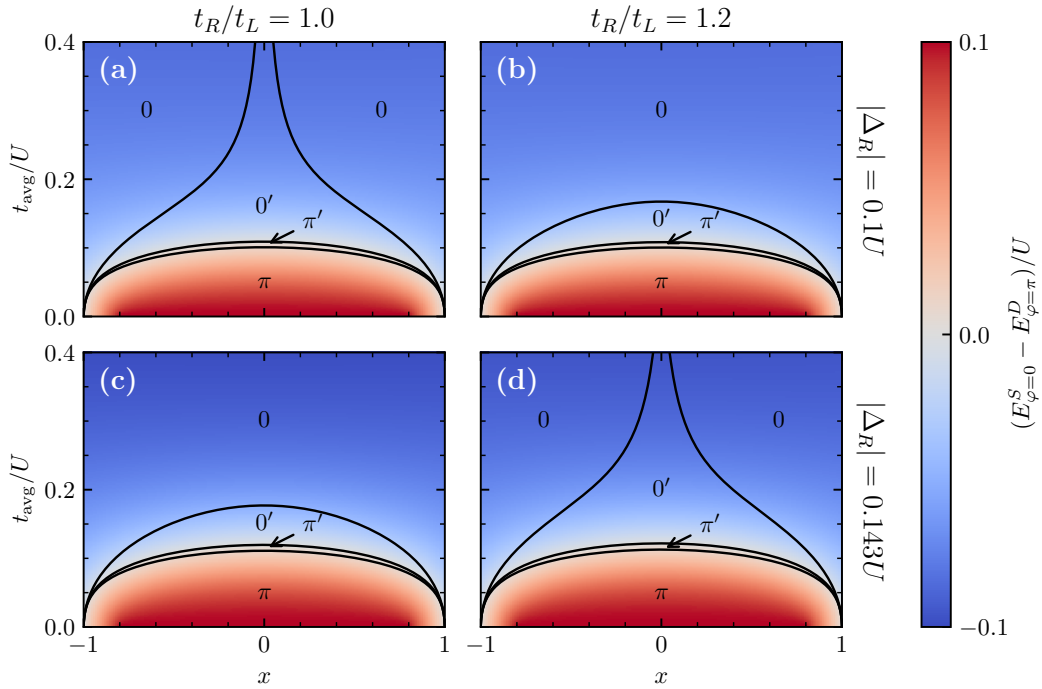
Figure 5.9: Phase diagrams for different coupling and gap asymmetries in two-lead ZBW systems. The color scale is the difference between the energy minimum of the singlet ($\varphi = 0$) and the doublet ($\varphi = \pi$). Common parameters: $|\Delta_L| = 0.1U$.

the 0-phase is inaccessible at particle-hole symmetry ($x = 0$); the doublet remains the ground state at $\varphi = \pi$ even for strong coupling (cf. Fig. 5.6(c)). The same is true for asymmetric junctions (Fig. 5.9(d)) if they are fine-tuned as in Fig. 5.7(b). One may run through the junction types by tuning t_{avg} for fixed $x \neq 0$ or vice versa for weak coupling. For other asymmetric configurations, the chimney-like $0'$-phase around $x = 0$ becomes a closed dome (Figs. 5.9(b)–(c)). These phase diagrams are similar to what we find in e.g. Refs. [17, 24].

5.6   Relation to the superconducting Anderson model

So far we have seen that the ZBW model may be used as a *qualitative* tool describing a lot of the physics of the superconducting Anderson model. In this section we will try to connect the ZBW to the Anderson model on a *quantitative* level. We will do so by a suitable renormalization of the tunneling parameter t^{ZBW} which describes the effective tunneling to a single SC level. We introduced the superscript "ZBW" to discern t^{ZBW} from the original tunneling amplitude t of the Anderson model, introduced in Eq. (2.3). The

rest of the parameters we leave unchanged compared to the full superconducting Anderson model. We split the problem into two parts: the proximitized limit and the Kondo regime. These are treated separately, initially, but connected in the end via a suitable interpolation function. Along we way, we compare with NRG results and find good agreement with the renormalized ZBW model in terms of the phase diagram – except in the intermediate regime where the system is neither in the proximitized limit nor the Kondo regime. The subgap energy spectrum and the supercurrent is shown to match poorly with NRG in the Kondo regime which we attribute to the lack of a continuum.

5.6.1   Renormalization for the proximitized QD

In the proximitized / infinite gap limit we find the correct renormalization of t^{ZBW} by a comparison of the QD self-energy in the superconducting Anderson model and in the ZBW model. To calculate the self-energy in the ZBW model, we may retrace our steps from Sections 2.1 and 3 and reuse the results derived there. We find that the Matsubara Nambu Green function for electrons in lead α is given by

$$\mathcal{G}_{0,\alpha}(i\omega_n) = \frac{-1}{|\Delta_\alpha|^2 + \omega_n^2} \begin{pmatrix} i\omega_n & -\Delta_\alpha \\ -\Delta_\alpha^* & i\omega_n \end{pmatrix}. \tag{5.75}$$

Comparing with the Anderson model (Eq. (2.9)), there is only a single momentum value, $k = k_F$, and, hence, no k-index in the ZBW approximation. Integrating out the ZBW leads, we find

$$\Sigma_d(i\omega_n) = \sum_\alpha \left(t_\alpha^{\mathrm{ZBW}} \right)^2 \tau_z \mathcal{G}_{0,\alpha}(i\omega_n)\tau_z = -\sum_\alpha \frac{\left(t_\alpha^{\mathrm{ZBW}} \right)^2}{|\Delta_\alpha|^2 + \omega_n^2} \begin{pmatrix} i\omega_n & \Delta_\alpha \\ \Delta_\alpha^* & i\omega_n \end{pmatrix} \tag{5.76}$$

as the self-energy for electrons on the QD. Comparing this result with the self-energy of the full superconducting Anderson model (Eq. (2.14)), we see that we can't simply replace t_α^{ZBW} by $\Gamma_\alpha = \pi\nu_{F,\alpha}t_\alpha^2$ in the ZBW model. In general, the conversion also depends on the gap and the energy.

$$\left(t_\alpha^{\mathrm{ZBW}} \right)^2 = \frac{2}{\pi} \arctan\left(\frac{D_\alpha}{\sqrt{|\Delta_\alpha|^2 + \omega_n^2}} \right) \Gamma_\alpha \sqrt{|\Delta_\alpha|^2 + \omega_n^2}. \tag{5.77}$$

For the proximitized dot, $|\Delta_\alpha| \gg \omega$, the conversion becomes energy-independent.

$$\left(t_\alpha^{\mathrm{ZBW}} \right)^2 \approx \frac{2}{\pi} \arctan\left(\frac{D_\alpha}{|\Delta_\alpha|} \right) \Gamma_\alpha |\Delta_\alpha|, \quad |\Delta_\alpha| \gg \omega. \tag{5.78}$$

In this infinite gap regime, Eq. (5.78) gives the correct renormalization of t_α^{ZBW} and a way to compare it to other, more exact, methods such as NRG or quantum Monte Carlo (QMC). Previously, we found that the leading order corrections to the infinite gap limit were of order $\Gamma_\alpha/|\Delta_\alpha|$ (see e.g. Eq. (4.20)). Therefore, we should expect Eq. (5.78) to hold for $|\Delta_\alpha| \gg \Gamma_\alpha$. Curiously, if one is working in units of $\Delta = 1$, this renormalization is equivalent to (neglecting the bandwidth term) just replacing $(t^{\mathrm{ZBW}})^2$ with Γ as one might do.

Figure 5.10 compares this t-conversion method to NRG data by Bauer *et al.* [16] for a single-lead ($N = 1$) S-QD system. Here, we have kept all other physical quantities unchanged compared to the Anderson model, i.e. $U^{\mathrm{ZBW}} = U, \Delta^{\mathrm{ZBW}} = \Delta$, and so on. We see that the agreement between the simple ZBW model and NRG is excellent in the proximitized limit ($\Delta \gtrsim \Gamma$) both at and away from particle-hole symmetry – on a par with MFS considered in Section 4. Moving towards the Kondo regime ($U \gg \Gamma, \Delta$), however, Eq. (5.78) fails to capture the YSR singlet ground state for $T_K \gtrsim 0.3\Delta$ as NRG predicts. ZBW predicts that the doublet phase wins out for $U \gtrsim 6\Gamma$ (Fig. 5.10(a)). The pertubative expansion around the infinite gap limit (MFS) from Section 4 describes this singlet-doublet crossover more accurately in the Kondo regime even though it underestimates the Kondo temperature somewhat at particle-hole symmetry; Meng *et al.* [15] finds that $T_K \propto \exp(-\pi U/4\Gamma)$ instead of $T_K \propto \exp(-\pi U/8\Gamma)$ as expected from scaling theory (Eq. (1.10)).

Note also that the YSR bound state crosses the gap, $E^S - E^D < \Delta$, in the lower left (dark blue) corner of Fig. 5.10(a) for $\Delta \ll \Gamma$. This is unphysical as the bound state is always within the gap in the real system (see e.g. Fig. 5.15). The gap crossing is an inherent problem of the ZBW model in the strong coupling limit, $\Gamma \gg \Delta$, as there are no bulk states to repel the bound state from the gap edges. On the other hand, Eq. (5.78) is not expected to describe the system in the strong coupling limit, anyway.

Previously, we also compared the MFS model to NRG data from Tanaka *et al.* [20] in the two-lead system S-QD-S with and without coupling asymmetry and SC phase bias (see Fig. 4.4). There we found that the perturbative approach was able to describe only the proximitized QD, i.e. $\varphi = 0$. For both symmetric and asymmetric coupling, the predicted phase transition was quite far off in the proximity-cancelled case, i.e. $\varphi = \pi$. The ZBW model handles this much better as illustrated in Fig. 5.11. For $\varphi = 0$, the ZBW model and MFS are almost indistinguishable, except for large U/Δ in Fig. 5.11(b) when compared
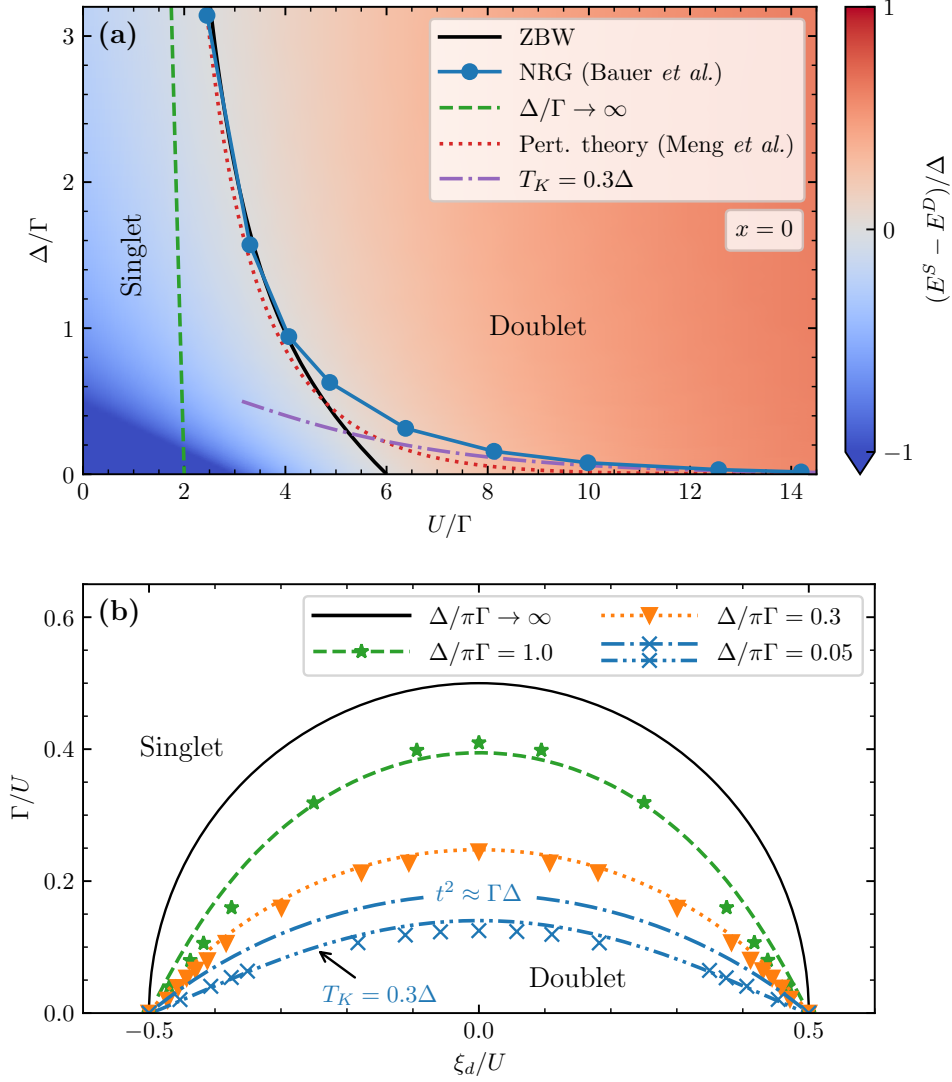
Figure 5.10: Phase diagram comparisons between ZBW and NRG data from Bauer *et al.* [16] for a single-lead ($N = 1$) S-QD system. Pane (a) reproduces their Fig. 9 at particle-hole symmetry with the ZBW phase transition line (using Eq. (5.78)) along with the infinite gap asymptote and the first order corrections to the infinite gap limit (Eq. (4.22)). The 'Kondo asymptote' $T_K = 0.3\Delta$ in the strongly interacting limit is also shown. The color indicates the energy difference between the lowest energy singlet and doublet (red: doublet; blue: singlet). Pane (b) compares the ZBW phase transition (lines) to the NRG data (symbols) given in Fig. 12 in Ref. [16]. The bottom two lines ($\Delta/\pi\Gamma = 0.05$) compare the ZBW model (using Eq. (5.78)) with the 'Kondo asymptote' $T_K = 0.3\Delta$; at particle-hole symmetry, $U \approx 8.1\Gamma$ at the phase transition (see (a)). Compare (b) with Fig. 4.2.

with Fig. 4.4(b). In this case, both approaches are close to the NRG phase transition with small deviations for large $U \gtrsim 5\Delta$. The proximity-cancelled limit, $\varphi = \pi$, is where the ZBW model really discerns itself from the perturbative approach. Here, the ZBW model agrees well with NRG for small U/Δ; large deviations occur for $U \gtrsim 5\Delta$. Opposed to MFS, the ZBW model correctly predicts the characteristic 'chimney' around the particle-hole symmetric point in Fig. 5.11(c) for symmetric coupling and $\varphi = \pi$. The 'chimney' is also present in Fig. 5.11(b), but the right-hand side is outside the plot limits – quite far from the NRG data (here we approach the Kondo regime).

5.6.2   Renormalization in the local moment regime

Through Eq. (5.78), we are able to reproduce the NRG phase diagrams on a quantitative level in the weakly interacting limit, $U \ll \Delta$, with the simple ZBW model. Equation (5.78) seems to break down around $U \simeq 5\Delta$, $\Delta \simeq \Gamma$. Thus, in the strongly interacting limit, $U \gg \Delta$, we need to do something else to use the ZBW model. For a single-lead S-QD system, we propose to use the universal phase transition relation [16, 18, 19]

$$T_K \approx 0.3\Delta_c, \qquad U \gg \Delta, \quad \epsilon_d \approx -U/2, \tag{5.79}$$

and map the ZBW phase transition onto this curve for $U \gg \Delta$. This is an empirical observation based on NRG results and also shown in Fig. 5.10. To emphasize that Eq. (5.79) only holds at the phase transition, we added the subscript c (for "critical") to Δ_c on the RHS. At the phase transition, Eq. (5.79) relates the physical quantities U, Γ, and Δ. As stated in Eq. (5.79), the definition of the Kondo temperature is the one given in Eq. (1.10). Note that Eq. (1.10) is valid away from particle-hole symmetry, and Yoshioka *et al.* [19] showed that the ratio T_K/Δ_c is only weakly dependent on ϵ_d around the particle-hole symmetric point, so we can neglect this effect (see also Fig. 5.10(b)).

Ideally, we want to interpolate between the proximitized limit and the local moment regime in a way that matches more accurate methods such as NRG. The intermediate regime is hard to match with a hands-off approach. In this case, a simple ZBW model may not be able to give quantitative predictions. The ZBW model loses its edge on e.g. NRG if it can't be used as a stand-alone tool.

In the single-lead S-QD system, the ZBW tunneling amplitude t^{ZBW} may be related to the hybridization Γ of the Anderson model through Eq. (5.79). At the ZBW phase transition, we write $t^{\mathrm{ZBW}}/U = f(\Delta/U, x)$ for some smooth, bijective function f. See
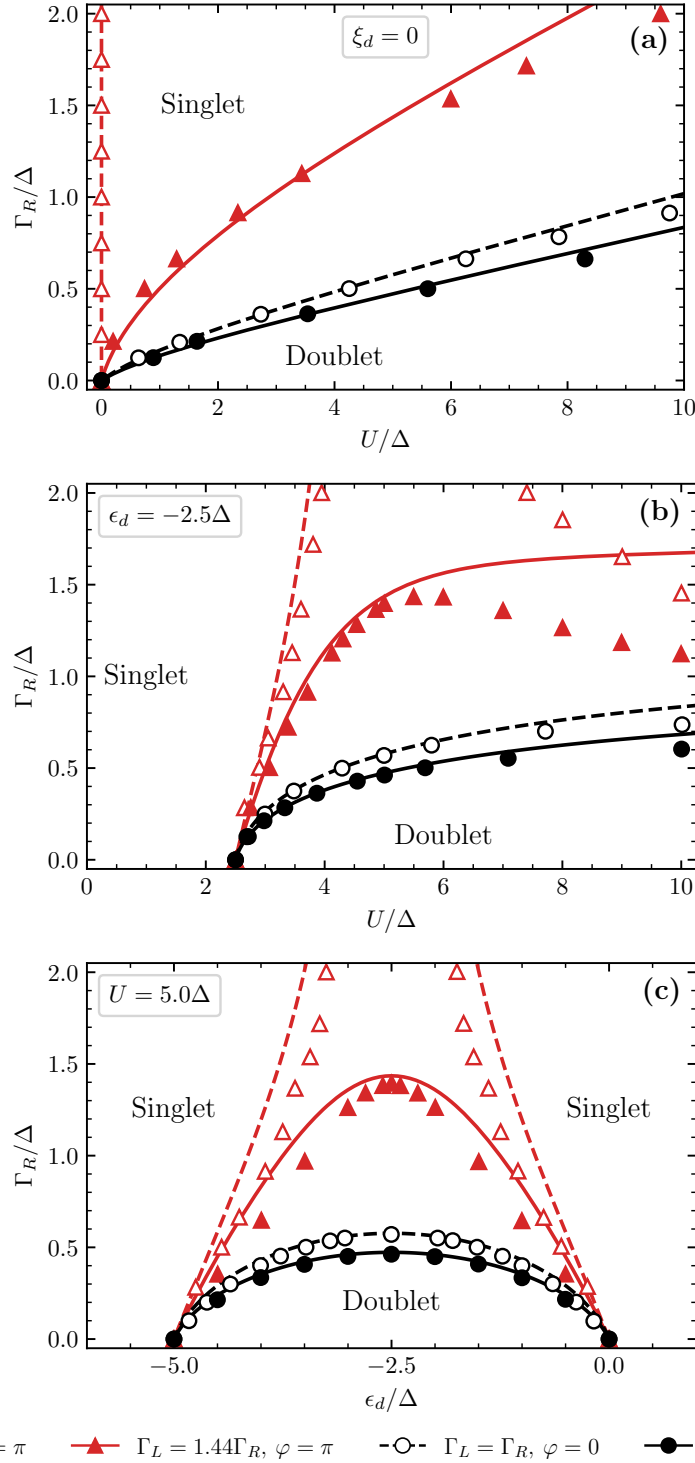
Figure 5.11: ZBW phase diagrams for $N = 2$ identical leads (L = Left lead, R = Right lead) with superconducting gap $|\Delta_L| = |\Delta_R| = \Delta$ and electronic bandwidth $D_L = D_R = 1.0 \times 10^5 \Delta$. The phase difference and couplings for the different lines is given by the legend below pane (c). Symbols are NRG data from Tanaka *et al.* [20] (the data has been graphically read off from their Figs. 5, 6, and 7) while the lines are ZBW results using Eq. (5.78). Compare this figure with Fig. 4.4.

appendix D for some details. Using Eq. (5.79), we find

$$\frac{t^{\text{ZBW}}}{U} = f\left(\frac{T_K}{0.3U}, x\right), \quad U \gg \Delta, \tag{5.80}$$

where the RHS depends on the ratio U/Γ and x. To map the ZBW phase transition onto the line $T_K = 0.3\Delta_c$, we find that the ratio t^{ZBW}/Γ must be varied as in Fig. 5.12. Again, we have kept all other parameters unchanged: $U^{\text{ZBW}} = U, \Delta^{\text{ZBW}} = \Delta, \epsilon_d^{\text{ZBW}} = \epsilon_d$. Close to the particle-hole symmetric point, $x = 0$, the surface does not vary much, but develops a 'shoulder' for $x \gtrsim 0.5$. We really only care about the asymptotic behavior in the limit $U \gg \Gamma$ since this is where Eq. (5.79) is valid. In the limit $U \gg \Delta$ – which is satisfied at the phase transition (of the full Anderson model) when $U \gg \Gamma$ – the ZBW phase transition occurs at (Eq. (5.63))

$$(t^{\text{ZBW}})^2 = \frac{2}{3}\frac{\Delta}{\frac{1}{\epsilon_d+U} - \frac{1}{\epsilon_d}}, \quad U \gg t^{\text{ZBW}}, \Delta. \tag{5.81}$$

We want this to align with $T_K = 0.3\Delta$, meaning that we should choose t^{ZBW} such that

$$(t^{\text{ZBW}})^2 = \frac{20}{9}\frac{T_K}{\frac{1}{\epsilon_d+U} - \frac{1}{\epsilon_d}}, \quad U \gg \Gamma, \tag{5.82}$$

which reduces to $(t^{\text{ZBW}})^2 = 5T_K U/9$ at particle-hole symmetry, $\epsilon_d = -U/2$. Inserting T_K from Eq. (1.10), we find

$$(t^{\text{ZBW}})^2 \approx 0.161 U\sqrt{\Gamma U}e^{-\pi U/8\Gamma}, \qquad U \gg \Gamma, \quad x = 0, \tag{5.83}$$

at particle-hole symmetry.

5.6.3 Interpolating between the proximitized limit and the local moment regime

To connect the limit of the proximitized QD and the Kondo regime, some kind of interpolation function is needed. In this case we combine Eq. (5.78) and Eq. (5.80) and write the ZBW tunneling as

$$t^{\text{ZBW}} = \mathcal{I}(U, \Delta, \Gamma)\sqrt{\frac{2}{\pi}\arctan\left(\frac{D}{\Delta}\right)\Gamma\Delta} + [1 - \mathcal{I}(U, \Delta, \Gamma)]\,Uf\left(\frac{T_K}{0.3U}, x\right), \tag{5.84}$$

with interpolation function $\mathcal{I}(U, \Delta, \Gamma)$. We know that this expression must reduce to Eq. (5.78) in the proximitized limit ($\mathcal{I} = 1$) and to Eq. (5.80) in the Kondo regime ($\mathcal{I} = 0$)
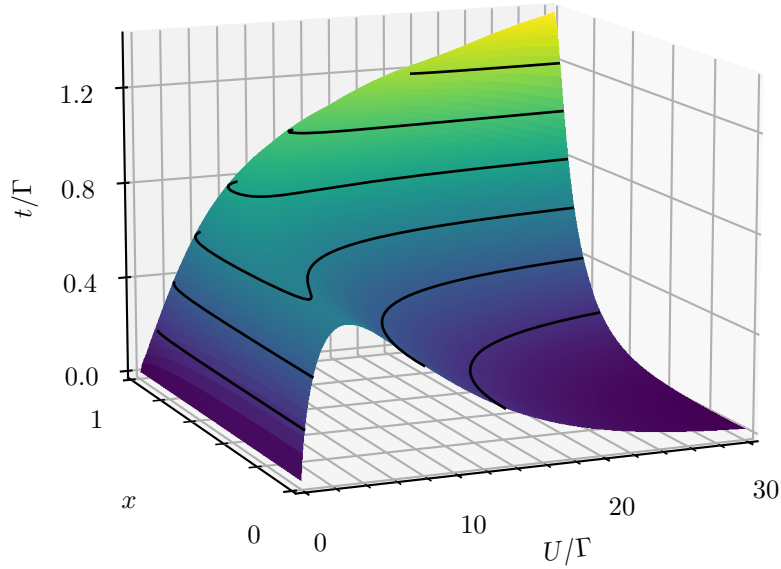
Figure 5.12: Rescaling of t^{ZBW} in the ZBW model to map the phase transition onto the 'Kondo asymptote' $T_K = 0.3\Delta$. The surface is mirror-symmetric in the plane $x = 0$ and, hence, only shown for $0 < x < 1$.

to match the NRG phase transition. The best interpolation function is hard to find and would require extensive comparison with e.g. NRG and more data. Here, we take the interpolation function to be a simple Fermi function

$$\mathcal{I}(U, \Delta, \Gamma) = n_F\left(\frac{U - U^*}{w}\right), \quad n_F(x) = (1 + e^x)^{-1}, \tag{5.85}$$

with some center U^* and width w. We set $U^* = 18.6\Delta$ to match the intersection of the ZBW transition (with Eq. (5.78)) and the 'Kondo asymptote' $T_K = 0.3\Delta$ in Fig. 5.10(a). We set $w = 2\Gamma$ to smooth out the transition between the regimes. The resulting phase diagrams and comparison with Bauer *et al.* is shown in Fig. 5.13. In Fig. 5.13(a), the ZBW phase transition moves from the line in the proximitized limit (Fig. 5.10(a)) for $U \lesssim 4\Gamma$ to the 'Kondo asymptote' for $U \gtrsim 5\Gamma$. In between the two regimes, the ZBW phase transition suffers a kink and is not as smooth as the NRG data suggest. In this intermediate regime, the ZBW model struggles and does not quite match the NRG. As Fig. 5.13(b) shows, the ZBW model does well also away from particle-hole symmetry in both the proximitized limit ($\Delta/\pi\Gamma > 0.3$) and the Kondo regime ($\Delta/\pi\Gamma = 0.05$).

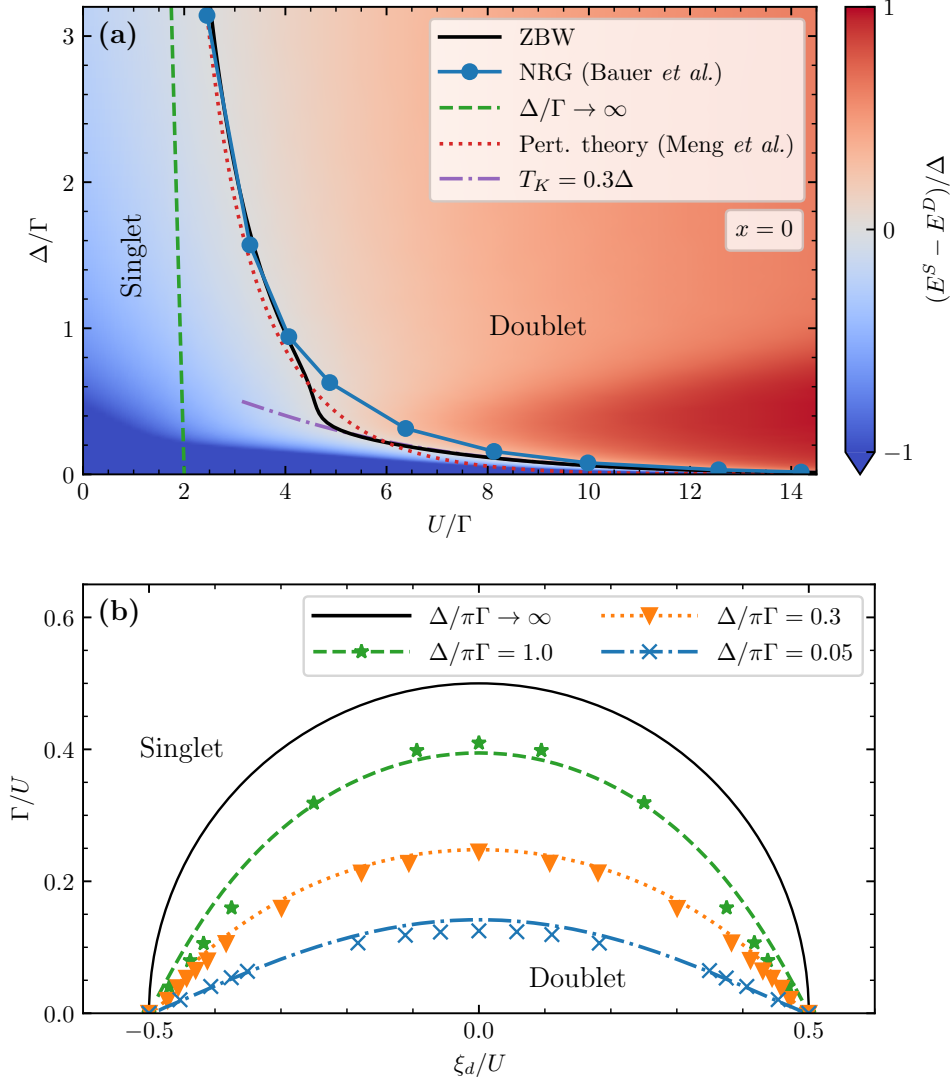We also show the ZBW phase diagrams along with the interpolation function in Fig. 5.14.

Figure 5.13: Phase diagram comparisons between ZBW and NRG data from Bauer *et al.* [16] for a single-lead ($N = 1$) S-QD system using Eqs. (5.84) and (5.85) with $U^* = 18.6\Delta$, $w = 2\Gamma$. The transition between the proximized limit and the local moment regime is smoothed out but still visible. Compare with Fig. 5.10.

The kink in the intermediate region is also visible in Fig. 5.14(a) as a bend in the phase transition surface. In Fig. 5.14(b), the axes are chosen differently and it looks smooth.

The phase diagram is, of course, only part of the story. If an experiment probes the subgap states in some way, the ZBW model should, ideally, be able to explain this, too – not just predict the phase transition. Bauer *et al.* [16] calculated the bound state energy for a single lead S-QD system in their NRG analysis of the superconducting Anderson model. In Fig. 5.15, we compare their NRG results with the interpolated ZBW model and the MFS model, we considered in Section 4. For $\Delta = 0.3\pi\Gamma$ (black curves), both ZBW and MFS models match the NRG data quite well up until the phase transition. The MFS model sees a small dip for $U < \Gamma$ which is due to a divergence in Eq. (4.21a) in the singlet region when $E_-^0 - E_\sigma^0 = -\Delta$ (see Section 4). For $U \gtrsim 5\Gamma$, the MFS model starts to deviate from the NRG data while the interpolated ZBW model follows NRG until $U \approx 13\Gamma$. The ZBW model interpolates smoothly between the infinite gap curve (black dashed curve) and the 'Kondo asymptote' (black dash-dotted curve), extending the validity of the ZBW model.

The t-conversion from the 'Kondo asymptote' (Eq. (5.80)) is, however, not able to capture the bound state energies in the Kondo regime, only the position of the phase transition. This is especially apparent from the small gap curves in Fig. 5.15(a): $\Delta/\pi\Gamma = 0.05, 0.005$ in red and blue, respectively. Here, $\mathcal{I} \approx 0$ along both curves, meaning the Kondo rescaling is used. One of the issues is the aforementioned inherent gap crossing of the doublet in the ZBW model which stems from a lack of continuum states in the superconductor at the gap edge. As is evident from Fig. 5.15(b), the doublet in the MFS model also crosses the gap edge for small Δ/Γ. Both models work well in the proximitized limit, with a small edge in favor of the ZBW model, and both models fail in the Kondo regime.

In a recent article by Žonda *et al.* [25] an extension of simple the infinite gap limit (see Section 3) was explored. In addition to the off-diagonal, anomalous terms in the self-energy (Eq. (2.14)), they included the leading order (in Δ/ω) diagonal terms of the self-energy. Since these are proportional to ω, they were able to include the effect in the Berry phase term through a simple renormalization of the parameters and reach the same
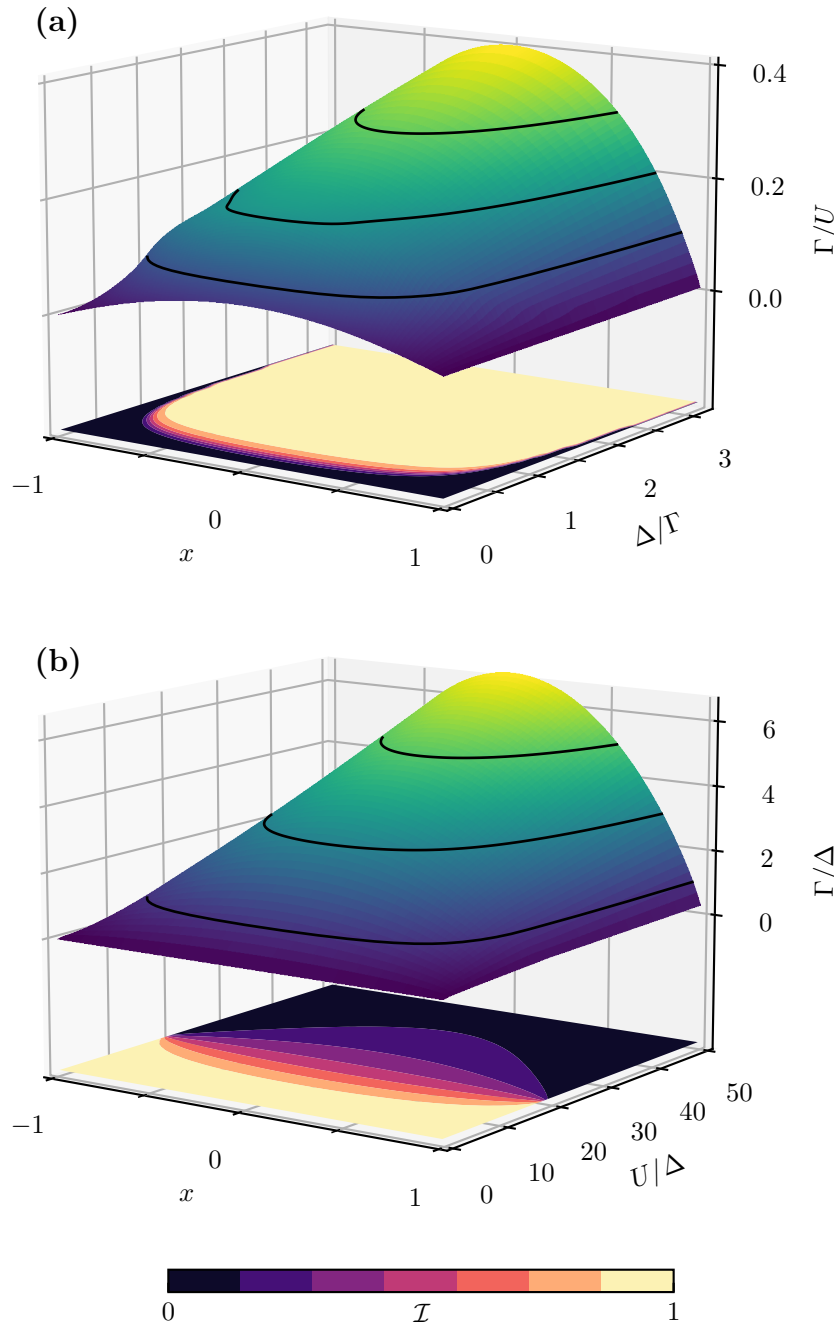
Figure 5.14: ZBW phase transition surfaces for a single-lead ($N = 1$) S-QD system using Eqs. (5.84) and (5.85) with $U^* = 18.6\Delta$, $w = 2\Gamma$. The phase transition occurs across the surfaces with the doublet phase residing inside the 'domes' (cf. Fig. 5.13). The color map on the 'floor' is the value of the interpolation function $\mathcal{I}$ at the phase transition (color bar below (b)). The difference between (a) and (b) is simply the choice of y- and z-axis.
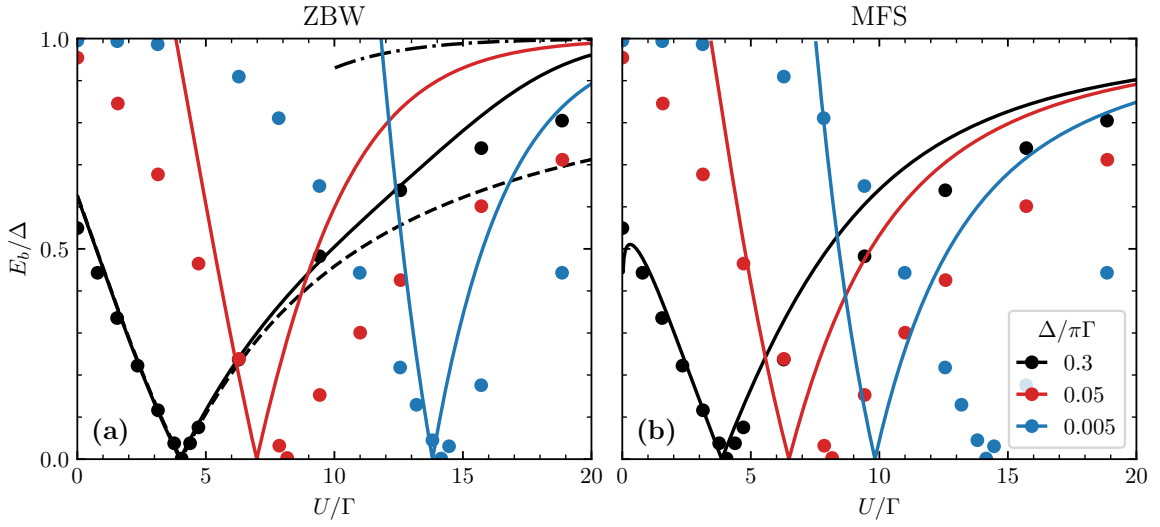
Figure 5.15: Comparison between bound state energies at particle-hole symmetry in the single lead S-QD system calculated with NRG (filled circles) by Bauer *et al.* [16], the interpolated ZBW model (a) (Eqs. (5.84) and (5.85) with $U^* = 18.6\Delta$, $w = 3\Gamma$), and first order corrections to the infinite gap limit (b) (Eq. (4.21a)). To show the effect of the interpolating function, for the largest $\Delta = 0.3\pi\Gamma$ (black) in (a), both the infinite gap curve (dashed) using Eq. (5.78) and the 'Kondo asymptote' (dash-dotted) using Eq. (5.80) are shown along with the interpolated curve (solid) using Eq. (5.84). Note that for strong coupling (small U/Γ), both ZBW and MFS have doublets that cross the gap edge.
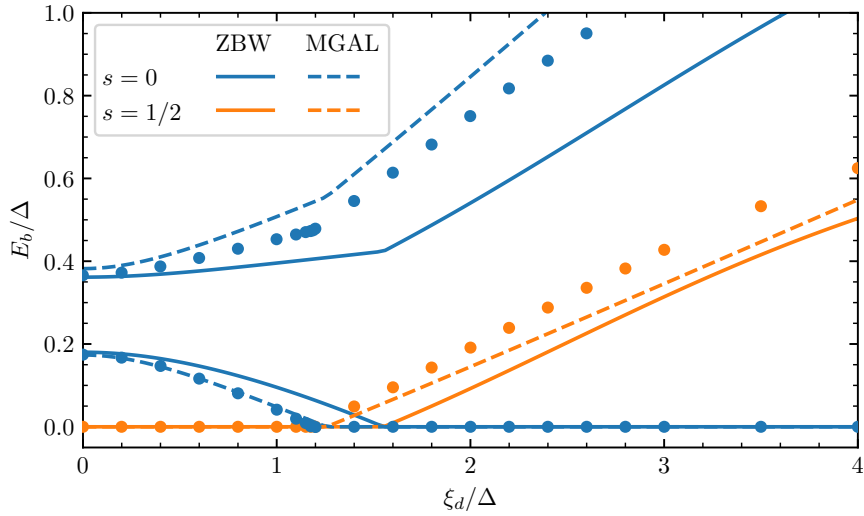
Figure 5.16: Subgap bound state energies as a function of the QD energy level ξ_d in a phase-biased, symmetric two-lead S-QD-S system. Symbols are NRG data graphically read off from Ref. [25] while the curves are interpolated ZBW (solid) and MGAL (dashed). Parameters used: $|\Delta_L| = |\Delta_R| \equiv \Delta$, $\Gamma_L = \Gamma_R = \Delta$, $U = 5\Delta$, $\varphi = 0.9\pi$.

effective Hamiltonian (Eq. (3.5)).

$$
\begin{aligned}
\xi_d &\to \tilde{\xi}_d = \nu \xi_d, \\
\gamma &\to \tilde{\gamma} = \nu \gamma, \\
U &\to \tilde{U} = \nu^2 U,
\end{aligned}
\tag{5.86}
$$

where $\nu = 1/(1 + \Gamma/\Delta)$. Via comparisons with NRG, they found better agreement when rescaling the QD energy level as $\xi_d \to \xi_d^{\mathrm{MGAL}} = \nu^2 \xi_d \sqrt{1 + 2\Gamma/\nu U}$. They called the infinite gap limit with this parameter rescaling the "modified generalized atomic limit" (MGAL). Among other things, they compare the energy of the subgap states in a two-lead S-QD-S system with NRG close to the proximitized limit. We show a comparison with the ZBW model in Fig. 5.16. Here, MGAL seems to have the upper hand but ZBW is not far off – both models certainly seem to qualitatively agree.

Žonda *et al.* also looked at the energy dispersion of the subgap states and the corresponding supercurrent in the proximitized limit. In Fig. 5.17 we reproduce the relevant figures and overlay the ZBW and MFS results. The energy dispersion in Figs. 5.17(a) and 5.17(b) show very good agreement between ZBW, MGAL, and the NRG data for both bound state energies close to the phase transition – they deviate slighty from NRG for

smaller φ. On the other hand, MFS has a hard time predicting the phase transition as we saw in Fig. 4.4 for non-zero φ (when the proximity effect is reduced). MFS describes the bound state energy well in Figs. 5.17(a) and 5.17(b) for small φ, however.

In Fig. 5.17(c), we note a few things about the supercurrent. First of all, the ZBW model matches more closely the NRG data than both MGAL and MFS. Second of all, they all fall short for large U/Δ as we have previously seen. Third of all, MGAL fails on two qualitative aspects as noted in Ref. [25]: the current is independent of U in the singlet phase and zero in the doublet phase since MGAL is only a rescaled infinite gap Hamiltonian (Eq. (3.5)). These shortcomings are not oberserved in ZBW and MFS. In a following paper, however, Pokorný & Žonda showed that these problems of MGAL are largely solved by a band correction which includes higher-order terms in the self-energy [26].

The ZBW model with appropriate rescaling of the effective tunneling parameter t does seem to match with NRG results in the proximitized limit and with the interpolation between the proximitized limit and the Kondo regime, the model's range of validity does seem to improve. The strongly interacting, $U \gg \Delta$, Kondo limit is, however, not described to a satisfying degree. Here, other methods – such as an effective Kondo model [17] – need to be used.
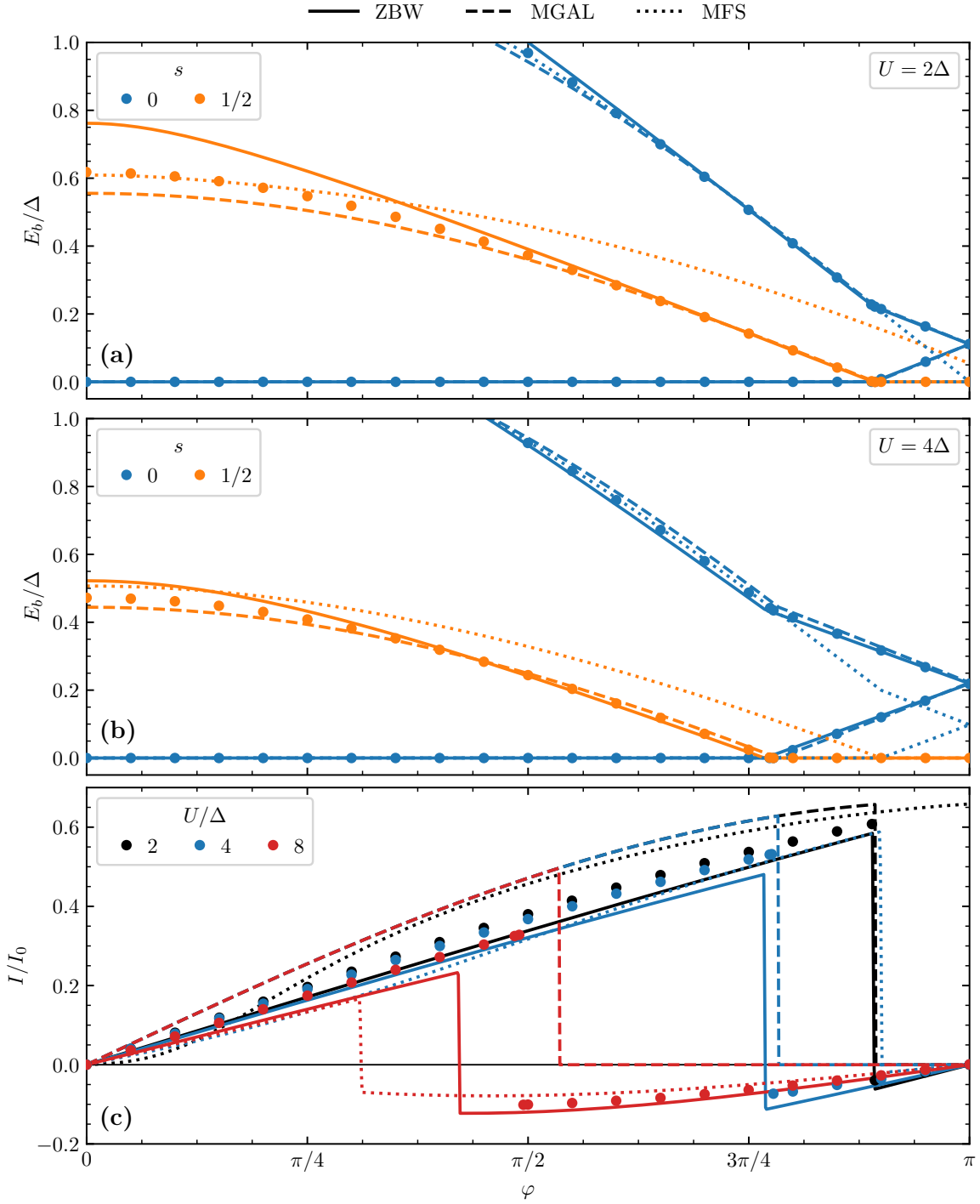
Figure 5.17: Bound state energies (a)-(b) and supercurrent (c) as a function of the SC phase difference φ in a symmetric two-lead S-QD-S system. Symbols are NRG data graphically read off from Ref. [25] while the curves are interpolated ZBW (solid), MGAL (dashed), and MFS (dotted). In (a) and (b), there are two singlets ($s = 0$) within the gap that become degenerate at $\varphi = \pi$. In (c), the supercurrent $I = 2e/\hbar(\partial E_{\mathrm{GS}}/\partial\varphi)$ has been normalized with $I_0 = e\Delta/\hbar$. Common parameters: $|\Delta_L| = |\Delta_R| \equiv \Delta$, $\Gamma_L = \Gamma_R = \Delta$, $\xi_d = 0$.

6   Conclusion

In this thesis we have studied interacting multiterminal Josephson junctions consisting of a single-level quantum dot coupled to superconducting leads through the superconducting impurity Anderson model. We used the path integral formalism to integrate out the superconducting leads and arrive at an effective action for electrons on the QD. In the limit of large superconducting gap, we found an effective low energy Hamiltonian which described proximity-induced superconductivity of the QD. We diagonalized the Hamiltonian, found the eigenstates and eigenenergies, and obtained the phase diagram, describing the transition from a BCS-like singlet to a magnetic doublet state.

To extend the model to finite superconducting gaps, we developed the multiterminal MFS model. Here, we expanded the partition function around the infinite gap limit and considered the lowest order corrections to the QD energy levels. In an effort to re-sum leading divergences, we introduced a self-consistency condition to attain the phase diagram from the renormalized energy levels. Good agreement was found with NRG data close to proximitized limit for single-lead (S-QD) and two-lead (S-QD-S) systems. In the proximity-cancelled limit ($\varphi = \pi$) of the two-lead (S-QD-S) system, however, the phase diagram was qualitatively wrong.

In the second half of this thesis, we studied the zero-bandwidth model which trades the continuum of bulk states in each lead for a single quasiparticle at the gap edge with an effective tunneling rate to the QD. First we explored the qualitative features of the model. We saw that the model was able to describe both the proximity effect and YSR screening of a local moment. Through perturbation theory we were able to understand the energy reduction of the many-body system by screening and the breaking apart of Cooper pairs in the leads. In a two-lead system, we saw that, depending on the (a)symmetry of the system, the screening could be carried out by a single lead or shared among the leads. We also calculated the energy dispersion and supercurrent in the ZBW model and used it to characterize S-QD-S systems as 0- or π-junctions.

In the end, we established a direct, quantitative connection between the ZBW model and the superconducting impurity Anderson model. Through comparisons with various NRG data, it became evident that the simple ZBW model – with effective tunneling rate found from the self-energy – provides an accurate description of the phase diagrams, bound state energies, and the supercurrent in QD-based JJs in the proximitized limit, $\Delta \gg \Gamma, U$. It was also able to describe the phase diagram of proximity-cancelled ($\varphi = \pi$) two-lead

S-QD-S systems – an advantage over MFS. In the proximitized limit of two-lead systems, the ZBW model is also favorable to the "modified generalized atomic limit" (MGAL) considered by Žonda *et al.* in terms of determination of the supercurrent and both models give an accurate description of the bound state energies.

In the local moment regime, we mapped the ZBW phase transition onto the 'Kondo asymptote' $T_K \approx 0.3\Delta_c$ in an attempt to extend the use of the ZBW model. By interpolating between the two regimes, we were able to better capture the onset of Kondo physics. Deep in the local moment regime, however, we were not able to describe the energy of the subgap states away from the phase transition – partly due to the gap crossing of the doublet in the strong-coupling limit of the ZBW model. To mend this, one likely needs to add more SC bulk states to the Hilbert space or use some clever parameter renormalization. Adding more states, of course, defeats the purpose of a simple, exactly solvable model.

7 Outlook

Recently, experiments [27–29] with full-shell InAs/Al nanowires coupled to a quantum dot have been performed, measuring the effect of an axially applied magnetic field on e.g. the subgap energies. A superconducting shell gives rise to the destructive Little-Parks effect [30, 31] and phase winding of the SC pairing potential when a flux penetrates the core. With a phase winding, opposing points on the shell geometry cancel each other in the proximity effect as in a two-lead (S-QD-S) junction with $\varphi = \pi$. This has been studied using mean-field theory [32] but it would be interesting to develop and explore a ZBW model. The multiterminal ZBW model investigated in this thesis could be considered a 'tight-binding' model by discretization of the superconducting shell into smaller segments and introducing a nearest neighbor inter-lead coupling. At this point, the approach is speculative but definitely an interesting idea to pursue.

As already showed by Ref. [14], such an inter-lead tunnel-coupling can lead to a non-trivial topology in non-interacting MJJs with three or more leads in the infinite gap limit. Physically, this is exciting because the transconductance is proportional to the Chern number and, therefore, quantized – as in the quantum Hall effect – in units of $4e^2/h$ [33].[1] Therefore, it would be interesting to study the topological properties of MJJs further – especially, if all this is contained within the ZBW model, now that we know it agrees

---

[1]An array of SQUIDs aranged in a chain has also been proposed to realize fractional transconductance – as in the more exotic *fractional* quantum Hall effect [34].

with NRG on the phase diagram, bound state energies, and the supercurrent close to the proximitized limit.

Another extension of this work – perhaps more straightforward compared to the above-mentioned future projects – is to use our quantitative ZBW model to calculate the current response to an ac bias voltage as done in Ref. [23]. This relies on the current matrix element between the ground state of the system and excited states within the same parity sector. In Ref. [23], they argue that a ZBW model qualitatively matches other analytical approaches but quantitative comparisons with e.g. NRG were missing to substantiate the application of ZBW models.

Appendices

A   Berry curvature and Chern number in the infinite gap limit

This section is partly based on the lecture notes by Kolodrubetz et al. [35] and Klees et al. [14].

We derived the many-particle eigenstates in the infinite gap limit in Section 3, describing the low energy effective Hamiltonian of the QD. Here, we will show that the topology of the eigenstates is trivial in the sense that the Chern-number is always zero in the φ_j, φ_k-phase space.

We may characterize the topology of the eigenstates using the geometric tensor. This tensor contains the information about the geometry and thus the topological features. First, let us define the *Berry connection* of state $|n\rangle = |\sigma\rangle, |\pm\rangle$

$$A_j^{(n)} = i \langle n | \partial_j n \rangle, \tag{A.1}$$

where $\partial_j = \frac{\partial}{\partial \varphi_j}$. The odd parity eigenstates $|\sigma\rangle$ do not depend on the phases of the leads and thus $A_j^{(\sigma)} = 0$. The even parity states depend on φ_j through u, v, and ζ. Using Eq. (3.6), we find

$$A_j^{(+)} = v^2 \partial_j \zeta + i(u \partial_j u + v \partial_j v) = - \left(A_j^{(-)} \right)^*. \tag{A.2}$$

Using $\partial_j E_A = |\gamma|/E_A \partial_j |\gamma| = -|\gamma| \tilde{\Gamma}_j \sin(\phi_j - \zeta)/E_A$, we differentiate Eq. (3.7) with respect to φ_j

$$\partial_j u = \frac{\xi_d |\gamma| \tilde{\Gamma}_j}{4 E_A^3 u} \sin(\phi_j - \zeta), \tag{A.3}$$

$$\partial_j v = \frac{-\xi_d |\gamma| \tilde{\Gamma}_j}{4 E_A^3 v} \sin(\phi_j - \zeta), \tag{A.4}$$

$$\partial_j \zeta = \frac{\tilde{\Gamma}_j}{|\gamma|} \cos(\phi_j - \zeta), \tag{A.5}$$

where $\tilde{\Gamma}_j = \frac{2}{\pi} \arctan\left(\frac{D}{|\Delta_\alpha|}\right) \Gamma_\alpha$. We note that $u \partial_j u + v \partial_j v = 0$ which reduces the Berry connection of the states $|\pm\rangle$ to

$$A_j^{(+)} = v^2 \partial_j \zeta = -A_j^{(-)}. \tag{A.6}$$

The curl of the Berry connection is the *Berry curvature* which contains the topological information of the state. From Eq. (A.6) we get

$$F_{jk}^{(+)} = \partial_j A_k^{(+)} - \partial_k A_j^{(+)} = \partial_j (v^2) \partial_k(\zeta) - \partial_k(v^2) \partial_j(\zeta) = -F_{jk}^{(-)}, \tag{A.7}$$

since $\partial_j(\partial_k\zeta) = \partial_k(\partial_j\zeta)$; the second derivatives of ζ are continuous. Using $\partial_j v^2 = 2v\partial_j v$ and Eqs. (A.4) and (A.5), we find

$$F_{jk}^{(+)} = \frac{\xi_d \Gamma_j \Gamma_k}{2E_A^3} \sin(\phi_k - \phi_j) = -F_{jk}^{(-)}. \tag{A.8}$$

The integral of the Berry curvature is quantized in most cases and known as the *Chern number*

$$C^{(\pm)} = \frac{1}{2\pi} \int_0^{2\pi} \mathrm{d}\varphi_j \int_0^{2\pi} \mathrm{d}\varphi_k \, F_{jk}^{(\pm)}. \tag{A.9}$$

This number tells trivial ($C = 0$) topological states from non-trivial ($C \neq 0$). In this case, it evaluates to $C^{(\pm)} = 0$. Let us show this explicitly.

Consider the inner integral

$$f(\varphi_j) = \int_0^{2\pi} \mathrm{d}\varphi_k \, \frac{\sin(\varphi_k - \varphi_j)}{\left(\xi_d^2 + |\gamma|^2\right)^{3/2}}. \tag{A.10}$$

This function is odd around the point $\varphi_j = \zeta_0 = \arg(\gamma_{\neq j,k}) = \arg(\sum_{\alpha \neq j,k} \tilde{\Gamma}_\alpha e^{i\varphi_\alpha})$; the angle of γ in the complex plane before summing over lead j and k. If $\varphi_j = \zeta_0$, then the angle of γ is unchanged when adding lead j, i.e. $\gamma_{\neq k} = |\gamma_{\neq k}| e^{i\zeta_0}$. For the integrand in Eq. (A.10), we have $|\gamma|^2 = |\gamma_{\neq k}|^2 + \Gamma_k^2 + 2|\gamma_{\neq k}|\Gamma_k \cos(\phi_k - \zeta_0)$, using the law of cosines. The integrand is thus also odd around $\varphi_k = \zeta_0$ and 2π-periodic, so it integrates to zero over a full period; $f(\zeta_0) = 0$.

A reflection about the axis $\zeta = \zeta_0$ does not change $|\gamma|$. Parametrizing φ_j, φ_k by $\Delta\varphi_j, \eta$, $|\gamma(\varphi_j = \zeta_0 + \Delta\varphi_j, \phi_k = \zeta_0 + \Delta\varphi_j + \eta)| = |\gamma(\varphi_j = \zeta_0 - \Delta\varphi_j, \phi_k = \zeta_0 - \Delta\varphi_j - \eta)|$. Using this and the 2π-periodicity of the integrand in Eq. (A.10), one may show that $f(\zeta_0 + \Delta\varphi_j) = -f(\zeta_0 - \Delta\varphi_j)$, such that $\int_0^{2\pi} \mathrm{d}\varphi_j \, f(\varphi_j) = 0$ and thus $C^{(\pm)} = 0$. This holds for all finite Γ_j, Γ_k such that the topology of the eigenstates $|\sigma\rangle, |\pm\rangle$ is always trivial in the infinite gap limit.

B   Imaginary time Nambu Green function for lead electrons

In Eq. (2.9), we found the Matsubara Nambu Green function for the electrons in lead α. Here we Fourier transform this expression to arrive at the imaginary time representation of this function.

By definition

$$\mathcal{G}_{0,\alpha k}(\tau) = \frac{1}{\beta} \sum_n \mathcal{G}_{0,\alpha k}(i\omega_n) e^{-i\omega_n \tau}, \quad 0 < \tau < \beta, \tag{B.1}$$

where $\mathcal{G}_{0,\alpha k}(i\omega_n)$ is given by Eq. (2.9), restated here with $E_{\alpha k} = \sqrt{\xi_{\alpha k}^2 + |\Delta_\alpha|^2}$:

$$\mathcal{G}_{0,\alpha k}(i\omega_n) = \frac{i\omega_n + \xi_{\alpha k}\tau_z - \Delta_\alpha'\tau_x + \Delta_\alpha''\tau_y}{(i\omega_n)^2 - E_{\alpha k}^2}. \tag{B.2}$$

We may evaluate the Matsubara sum with complex contour integration. Consider the integral

$$I = \int_C \frac{dz}{2\pi i} \left(1 - f(E_{\alpha k})\right) \frac{[1, z]}{z^2 - E_{\alpha k}^2} e^{-\tau z}, \quad 0 < \tau < \beta \tag{B.3}$$

using a circle of infinite radius centered at the origin as the contour C and integrating in the counter-clockwise direction. Here, $f(z) = [\exp(\beta z) + 1]^{-1}$ is the Fermi function. The notation $[1, z]$ is simply to evaluate two similar integrals at the same time. By Jordan's lemma, $I = 0$ since the integrand is exponentially suppressed along the contour. The integrand has poles at $z = i\omega_n$ due to the Fermi function and at $z = \pm E_{\alpha k}$. The poles at $z = i\omega_n$ are simple poles with residue $1/\beta$. Thus, by the residue theorem

$$\begin{aligned}
I &= \frac{1}{\beta} \sum_n \frac{[1, i\omega_n]}{(i\omega_n)^2 - E_{\alpha k}^2} e^{-i\omega_n \tau} + 2\pi i \text{Res}(z = E_{\alpha k}) + 2\pi i \text{Res}(z = -E_{\alpha k}) \\
&= \frac{1}{\beta} \sum_n \frac{[1, i\omega_n]}{(i\omega_n)^2 - E_{\alpha k}^2} e^{-i\omega_n \tau} + \frac{f(E_{\alpha k})}{2E_{\alpha k}} \left[e^{E_{\alpha k}(\beta - \tau)} - e^{E_{\alpha k}\tau}, e^{E_{\alpha k}(\beta - \tau)} + e^{E_{\alpha k}\tau}\right].
\end{aligned} \tag{B.4}$$

Combined with Jordan's lemma, we find

$$\frac{1}{\beta} \sum_n \frac{[1, i\omega_n]}{(i\omega_n)^2 - E_{\alpha k}^2} e^{-i\omega_n \tau} = -\frac{f(E_{\alpha k})}{2E_{\alpha k}} \left[e^{E_{\alpha k}(\beta - \tau)} - e^{E_{\alpha k}\tau}, e^{E_{\alpha k}(\beta - \tau)} + e^{E_{\alpha k}\tau}\right]. \tag{B.5}$$

The components of the imaginary time Nambu Green function are then for $0 < \tau < \beta$

$$\sum_k \mathcal{G}_{0,\alpha k}^{11}(\tau) = -\sum_k \frac{1}{2} f(E_{\alpha k}) \left(e^{E_{\alpha k}(\beta - \tau)} + e^{E_{\alpha k}\tau}\right), \tag{B.6a}$$

$$\mathcal{G}_{0,\alpha k}^{12}(\tau) = \frac{\Delta_\alpha}{2E_{\alpha k}} f(E_{\alpha k}) \left(e^{E_{\alpha k}(\beta - \tau)} - e^{E_{\alpha k}\tau}\right). \tag{B.6b}$$

The momentum-sum is simply there to kill the anti-symmetric term $\xi_{\alpha k}$ that sits on the diagonal. Note that $\sum_k \mathcal{G}_{0,\alpha k}^{22}(\tau) = \sum_k \mathcal{G}_{0,\alpha k}^{11}(\tau)$, $\mathcal{G}_{0,\alpha k}^{21}(\tau) = \mathcal{G}_{0,\alpha k}^{12}(\tau)^*$ determines the two other components.

C   QD Nambu Green function in the infinite gap limit

In this section, we derive the components of the Nambu Green function for electrons on the QD in the infinite gap limit. In imaginary time, the components of the Green function are given by Eq. (4.9), and copied here

$$
\mathcal{G}_{0,d}(-\tau) = \begin{pmatrix} \left\langle d_\uparrow^\dagger(\tau) d_\uparrow(0) \right\rangle_0 & \left\langle d_\downarrow(\tau) d_\uparrow(0) \right\rangle_0 \\ \left\langle d_\uparrow^\dagger(\tau) d_\downarrow^\dagger(0) \right\rangle_0 & \left\langle d_\downarrow(\tau) d_\downarrow^\dagger(0) \right\rangle_0 \end{pmatrix}.
\tag{C.1}
$$

The Green functions are evaluated in the Lehmann representation, meaning $Z_0 \left\langle \cdots \right\rangle_0 = \sum_{n_0} e^{-\beta E_n^0} \left\langle n_0 | \cdots | n_0 \right\rangle$ using the eigenstates $|n_0\rangle \in \{|\uparrow\rangle, |\downarrow\rangle, |+\rangle, |-\rangle\}$, where (Eq. (3.6))

$$
|+\rangle = u |\uparrow\downarrow\rangle - v e^{-i\zeta} |0\rangle, \qquad |-\rangle = u |0\rangle + v e^{i\zeta} |\uparrow\downarrow\rangle,
\tag{C.2}
$$

and $|\uparrow\downarrow\rangle = d_\uparrow^\dagger d_\downarrow^\dagger |0\rangle$. The time evolution is given by the infinite gap Hamiltonian (3.5) such that Heisenberg operators evolve as $A_H(\tau) = e^{H_\infty \tau} A_S e^{-H_\infty \tau}$, where A_H, A_S refer to the operator A in the Heisenberg, Schrödinger picture, respectively. It is useful to consider the identity

$$
\begin{aligned}
\langle A_H(\tau) B_H(0) \rangle_0 &= \frac{1}{Z_0} \sum_{n_0} e^{-\beta E_n^0} \langle n_0 | e^{H_\infty \tau} A_S e^{-H_\infty \tau} B_S | n_0 \rangle \\
&= \frac{1}{Z_0} \sum_{n_0} e^{-(\beta - \tau) E_n^0} \langle n_0 | A_S e^{-H_\infty \tau} B_S | n_0 \rangle.
\end{aligned}
\tag{C.3}
$$

Let us also apply $e^{-H_\infty \tau}$ to the states $|0\rangle, |\uparrow\downarrow\rangle$ that are not eigenstates.

$$
\begin{aligned}
e^{-H_\infty \tau} |0\rangle &= e^{-H_\infty \tau} \left(-v e^{i\zeta} |+\rangle + u |-\rangle \right) = -v e^{i\zeta} e^{-E_+^0 \tau} |+\rangle + u e^{-E_-^0 \tau} |-\rangle \\
&= \left(u^2 e^{-E_-^0 \tau} + v^2 e^{-E_+^0 \tau} \right) |0\rangle + u v e^{i\zeta} \left(e^{-E_-^0 \tau} - e^{-E_+^0 \tau} \right) |\uparrow\downarrow\rangle,
\end{aligned}
\tag{C.4}
$$

$$
\begin{aligned}
e^{-H_\infty \tau} |\uparrow\downarrow\rangle &= e^{-H_\infty \tau} \left(u |+\rangle + v e^{-i\zeta} |-\rangle \right) = u e^{-E_+^0 \tau} |+\rangle + v e^{-i\zeta} e^{-E_-^0 \tau} |-\rangle \\
&= u v e^{-i\zeta} \left(e^{-E_-^0 \tau} - e^{-E_+^0 \tau} \right) |0\rangle + \left(u^2 e^{-E_+^0 \tau} + v^2 e^{-E_-^0 \tau} \right) |\uparrow\downarrow\rangle.
\end{aligned}
\tag{C.5}
$$

Now, we are ready to calculate the Green functions.

$$
\begin{aligned}
Z_0 \left\langle d_\uparrow^\dagger(\tau) d_\uparrow(0) \right\rangle_0 &= \sum_{n_0} e^{-(\beta-\tau)E_n^0} \langle n_0|d_\uparrow^\dagger e^{-H_\infty \tau} d_\uparrow|n_0\rangle \\
&= \left(e^{-(\beta-\tau)E_\uparrow^0} \langle\uparrow|d_\uparrow^\dagger e^{-H_\infty \tau} d_\uparrow|\uparrow\rangle + e^{-(\beta-\tau)E_+^0} \langle+|d_\uparrow^\dagger e^{-H_\infty \tau} d_\uparrow|+\rangle \right. \\
&\qquad \left. + e^{-(\beta-\tau)E_-^0} \langle-|d_\uparrow^\dagger e^{-H_\infty \tau} d_\uparrow|-\rangle \right) \\
&= \left(e^{-(\beta-\tau)E_\uparrow^0} \langle 0|e^{-H_\infty \tau}|0\rangle + u^2 e^{-(\beta-\tau)E_+^0} \langle\downarrow|e^{-H_\infty \tau}|\downarrow\rangle \right. \\
&\qquad \left. + v^2 e^{-(\beta-\tau)E_-^0} \langle\downarrow|e^{-H_\infty \tau}|\downarrow\rangle \right) \\
&= u^2 \left(e^{-E_-^0 \tau} e^{-E_\uparrow^0(\beta-\tau)} + e^{-E_\downarrow^0 \tau} e^{-E_+^0(\beta-\tau)} \right) \\
&\quad + v^2 \left(e^{-E_+^0 \tau} e^{-E_\uparrow^0(\beta-\tau)} + e^{-E_\downarrow^0 \tau} e^{-E_-^0(\beta-\tau)} \right),
\end{aligned}
\tag{C.6}
$$

$$
\begin{aligned}
Z_0 \left\langle d_\downarrow(\tau) d_\downarrow^\dagger(0) \right\rangle_0 &= \sum_{n_0} e^{-(\beta-\tau)E_n^0} \langle n_0|d_\downarrow e^{-H_\infty \tau} d_\downarrow^\dagger|n_0\rangle \\
&= \left(e^{-(\beta-\tau)E_\uparrow^0} \langle\uparrow|d_\downarrow e^{-H_\infty \tau} d_\downarrow^\dagger|\uparrow\rangle + e^{-(\beta-\tau)E_+^0} \langle+|d_\downarrow e^{-H_\infty \tau} d_\downarrow^\dagger|+\rangle \right. \\
&\qquad \left. + e^{-(\beta-\tau)E_-^0} \langle-|d_\downarrow e^{-H_\infty \tau} d_\downarrow^\dagger|-\rangle \right) \\
&= \left(e^{-(\beta-\tau)E_\uparrow^0} \langle\uparrow\downarrow|e^{-H_\infty \tau}|\uparrow\downarrow\rangle + v^2 e^{-(\beta-\tau)E_+^0} \langle\downarrow|e^{-H_\infty \tau}|\downarrow\rangle \right. \\
&\qquad \left. + u^2 e^{-(\beta-\tau)E_-^0} \langle\downarrow|e^{-H_\infty \tau}|\downarrow\rangle \right) \\
&= u^2 \left(e^{-E_+^0 \tau} e^{-E_\uparrow^0(\beta-\tau)} + e^{-E_\downarrow^0 \tau} e^{-E_-^0(\beta-\tau)} \right) \\
&\quad + v^2 \left(e^{-E_-^0 \tau} e^{-E_\uparrow^0(\beta-\tau)} + e^{-E_\downarrow^0 \tau} e^{-E_+^0(\beta-\tau)} \right),
\end{aligned}
\tag{C.7}
$$

$$
\begin{aligned}
Z_0 \left\langle d_\uparrow^\dagger(\tau) d_\downarrow^\dagger(0) \right\rangle_0 &= \sum_{n_0} e^{-(\beta-\tau)E_n^0} \langle n_0|d_\uparrow^\dagger e^{-H_\infty \tau} d_\downarrow^\dagger|n_0\rangle \\
&= \left(e^{-(\beta-\tau)E_\uparrow^0} \langle\uparrow|d_\uparrow^\dagger e^{-H_\infty \tau} d_\downarrow^\dagger|\uparrow\rangle + e^{-(\beta-\tau)E_+^0} \langle+|d_\uparrow^\dagger e^{-H_\infty \tau} d_\downarrow^\dagger|+\rangle \right. \\
&\qquad \left. + e^{-(\beta-\tau)E_-^0} \langle-|d_\uparrow^\dagger e^{-H_\infty \tau} d_\downarrow^\dagger|-\rangle \right) \\
&= \left(-e^{-(\beta-\tau)E_\uparrow^0} \langle 0|e^{-H_\infty \tau}|\uparrow\downarrow\rangle - uv e^{-i\zeta} e^{-(\beta-\tau)E_+^0} \langle\downarrow|e^{-H_\infty \tau}|\downarrow\rangle \right. \\
&\qquad \left. + uv e^{-i\zeta} e^{-(\beta-\tau)E_-^0} \langle\downarrow|e^{-H_\infty \tau}|\downarrow\rangle \right) \\
&= uv e^{-i\zeta} \left(e^{-E_+^0 \tau} e^{-E_\uparrow^0(\beta-\tau)} + e^{-E_\downarrow^0 \tau} e^{-E_-^0(\beta-\tau)} \right. \\
&\qquad\qquad \left. -e^{-E_-^0 \tau} e^{-E_\uparrow^0(\beta-\tau)} - e^{-E_\downarrow^0 \tau} e^{-E_+^0(\beta-\tau)} \right) \\
&= Z_0 \left\langle d_\downarrow(\tau) d_\uparrow(0) \right\rangle_0^*.
\end{aligned}
\tag{C.8}
$$

The last equality follows from $\langle n_0|d_\uparrow^\dagger e^{-H_\infty \tau} d_\downarrow^\dagger|n_0\rangle^* = \langle n_0|d_\downarrow e^{-H_\infty \tau} d_\uparrow|n_0\rangle$.

D ZBW single-lead phase transition

In section Section 5.6 we needed the function f which relates Δ/U to t^{ZBW}/U at the singlet-doublet phase transition in the ZBW model for some $x = 1 + 2\epsilon_d/U$.

$$\frac{t^{\mathrm{ZBW}}}{U} = f\left(\frac{\Delta}{U}, x\right). \tag{D.1}$$

We approximate f numerically through diagonalization of the ZBW Hamiltonian for fixed x on a 2D grid (Δ/U, t^{ZBW}/U) and, afterwards, using the marching squares algorithm ('mpl2014' in `ContourPy`) to estimate the singlet-doublet phase transition $E^S - E^D = 0$ through linear interpolation between grid points. The grid is of size 200×200 with logarithmic spacing ($\Delta/U \in [10^{-4}, 10^3]$, $t^{\mathrm{ZBW}}/U \in [5 \times 10^{-4}, 30]$) and we repeat this for 101 different $x \in [-0.99, 0.99]$ (evenly spaced in linear space). See Fig. D.1 for examples of this. The sampled values of f are shown in Fig. D.2. Outside this grid, the asymptotic values are used (dashed lines in Fig. D.1).

$$f\left(\frac{\Delta}{U}, x\right) \rightarrow \begin{cases} \sqrt{\dfrac{2\Delta/3U}{\frac{U}{\epsilon_d+U} - \frac{U}{\epsilon_d}}}, & U \gg \Delta \\[2ex] \left[\dfrac{\Delta^2}{U^2}\left(\dfrac{1}{4} - \dfrac{\xi_d^2}{U^2}\right)\right]^{1/4}, & \Delta \gg U. \end{cases} \tag{D.2}$$

The asymptote for $U \gg \Delta$ is found from Eq. (5.63) while the other ($\Delta \gg U$) is given by the infinite gap limit of the ZBW model. From the QD self-energy in the ZBW model (Eq. (5.76)), we find that the infinite gap Hamiltonian has the same form as Eq. (3.5) but with a different tunneling parameter, γ. For a single-lead S-QD system, $\gamma = (t^{\mathrm{ZBW}})^2/\Delta$. From Section 3 we know the phase transition occurs at $\xi_d^2 + |\gamma|^2 = U^2/4$ and inserting $\gamma = (t^{\mathrm{ZBW}})^2/\Delta$, one finds the asymptotic behaviour of t^{ZBW}/U given by Eq. (D.2) in the limit $\Delta \gg U$.
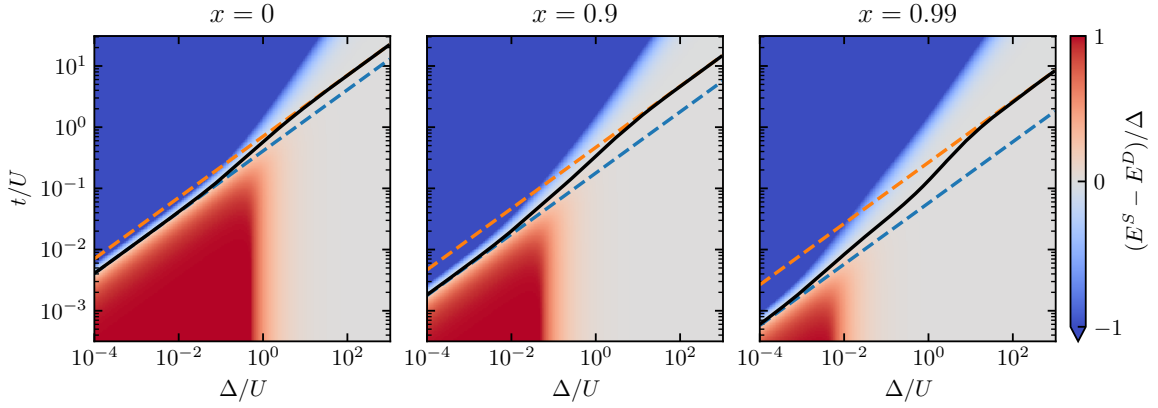
Figure D.1: ZBW single-lead (S-QD) phase diagrams for different $x = 1+2\epsilon_d/U$ on a log-log scale. Phase diagrams are identical for $x \to -x$. The dashed lines denote the asymptotic phase transition lines given by Eq. (D.2). It depends on x, when the asymptotic behavior is reached.
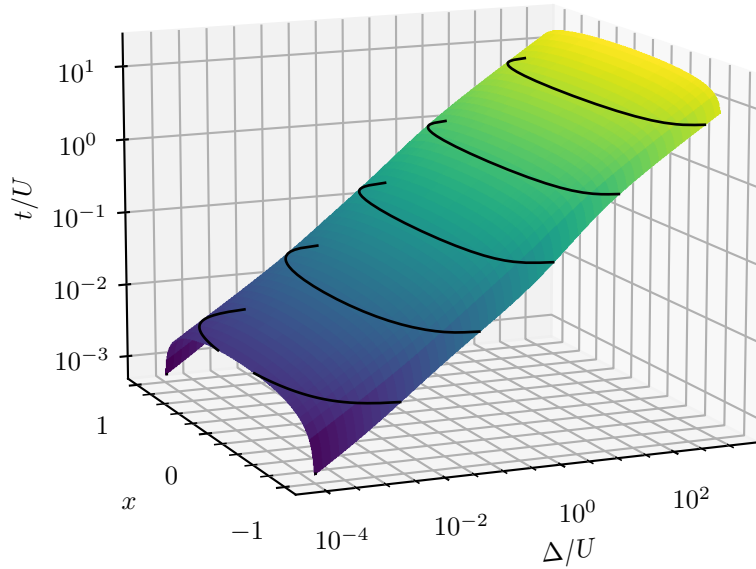

Figure D.2: ZBW single-lead S-QD system: relation between Δ/U, x, and t^{ZBW}/U at the singlet-doublet phase transition.

Bibliography

[1] J. Bardeen, L. N. Cooper, and J. R. Schrieffer, "Theory of superconductivity", Phys. Rev. **108**, 1175–1204 (1957).

[2] J. Bardeen and D. Pines, "Electron-phonon interaction in metals", Phys. Rev. **99**, 1140–1150 (1955).

[3] P. Coleman, *Introduction to many-body physics* (Cambridge University Press, Nov. 2015).

[4] B. D. Josephson, "Possible new effects in superconductive tunnelling", Physics Letters **1**, 251–253 (1962).

[5] J. Sólyom, "Superconductivity", in *Fundamentals of the physics of solids – volume II: Electronic properties* (Springer, Berlin, Germany, 2009), pp. 449–515.

[6] V. Ambegaokar and A. Baratoff, "Tunneling between superconductors", Phys. Rev. Lett. **10**, 486–489 (1963).

[7] A. Bargerbos et al., "Singlet-Doublet Transitions of a Quantum Dot Josephson Junction Detected in a Transmon Circuit", PRX Quantum **3**, 030311 (2022).

[8] A. C. Hewson, *The Kondo Problem to Heavy Fermions* (Cambridge University Press, Cambridge, England, UK, Jan. 1993).

[9] J. R. Schrieffer and P. A. Wolff, "Relation between the Anderson and Kondo Hamiltonians", Phys. Rev. **149**, 491–492 (1966).

[10] F. D. M. Haldane, "Theory of the atomic limit of the Anderson model. I. Perturbation expansions re-examined", J. Phys. C: Solid State Phys. **11**, 5015 (1978).

[11] L. Yu, "Bound state in superconductors with paramagnetic impurities", Acta. Phys. Sin. **21**, 75–91 (1965).

[12] H. Shiba, "Classical spins in superconductors", Prog. Theor. Phys. **40**, 435–451 (1968).

[13] A. I. Rusinov, "Superconductivity near a paramagnetic impurity", JETP Lett. **9**, 85 (1969), [Zh. Eksp. Teor. Fiz. **9**, 146 (1968)].

[14] R. L. Klees et al., "Microwave spectroscopy reveals the quantum geometric tensor of topological Josephson matter", Phys. Rev. Lett. **124**, 197002 (2020).

[15] T. Meng, S. Florens, and P. Simon, "Self-consistent description of Andreev bound states in Josephson quantum dot devices", Phys. Rev. B **79**, 224521 (2009).

[16] J. Bauer, A. Oguri, and A. C. Hewson, "Spectral properties of locally correlated electrons in a Bardeen–Cooper–Schrieffer superconductor", J. Phys.: Condens. Matter **19**, 486211 (2007).

[17] G. Kiršanskas et al., "Yu-Shiba-Rusinov states in phase-biased superconductor–quantum dot–superconductor junctions", Phys. Rev. B **92**, 235422 (2015).

[18] K. Satori et al., "Numerical renormalization group study of magnetic impurities in superconductors", J. Phys. Soc. Jpn. **61**, 3239–3254 (1992).

[19] T. Yoshioka and Y. Ohashi, "Numerical renormalization group studies on single impurity Anderson model in superconductivity: a unified treatment of magnetic, nonmagnetic impurities, and resonance scattering", J. Phys. Soc. Jpn. **69**, 1812–1823 (2000).

[20] Y. Tanaka, A. Oguri, and A. C. Hewson, "Kondo effect in asymmetric Josephson couplings through a quantum dot", New J. Phys. **9**, 115 (2007).

[21] K. Grove-Rasmussen et al., "Yu–Shiba–Rusinov screening of spins in double quantum dots", Nat. Commun. **9**, 1–6 (2018).

[22] J. C. E. Saldaña et al., "Supercurrent in a Double Quantum Dot", Phys. Rev. Lett. **121**, 257701 (2018).

[23] C. Hermansen, A. L. Yeyati, and J. Paaske, "Inductive microwave response of Yu-Shiba-Rusinov states", Phys. Rev. B **105**, 054503 (2022).

[24] A. V. Rozhkov and D. P. Arovas, "Josephson coupling through a magnetic impurity", Phys. Rev. Lett. **82**, 2788–2791 (1999).

[25] M. Žonda et al., "Generalized atomic limit of a double quantum dot coupled to superconducting leads", Phys. Rev. B **107**, 115407 (2023).

[26] V. Pokorný and M. Žonda, "Effective low-energy models for superconducting impurity systems", Phys. Rev. B **107**, 155111 (2023).

[27] S. Vaitiekėnas et al., "Flux-induced topological superconductivity in full-shell nanowires", Science **367**, eaav3392 (2020).

[28] D. Razmadze et al., "Quantum Dot Parity Effects in Trivial and Topological Josephson Junctions", Phys. Rev. Lett. **125**, 116803 (2020).

[29] M. Valentini et al., "Nontopological zero-bias peaks in full-shell nanowires induced by flux-tunable Andreev states", Science **373**, 82–88 (2021).

[30] W. A. Little and R. D. Parks, "Observation of Quantum Periodicity in the Transition Temperature of a Superconducting Cylinder", Phys. Rev. Lett. **9**, 9–12 (1962).

[31] M. Tinkham, *Introduction to Superconductivity*, Dover Books on Physics Series (Dover Publications, 2004).

[32] S. D. Escribano et al., "Fluxoid-induced pairing suppression and near-zero modes in quantum dots coupled to full-shell nanowires", Phys. Rev. B **105**, 045418 (2022).

[33] R.-P. Riwar et al., "Multi-terminal Josephson junctions as topological matter", Nat. Commun. **7**, 1–5 (2016).

[34] H. Weisbrich et al., "Fractional transconductance via non-adiabatic topological Cooper pair pumping", arXiv, `10.48550/arXiv.2212.11757` (2022).

[35] M. Kolodrubetz et al., "Geometry and non-adiabatic response in quantum and classical systems", Phys. Rep. **697**, 1–87 (2017).